Title
Multi-physics Modeling for Molten Salt Reactors (MSRs)

Author
SHI, JUN

Publication Date
2021

Peer reviewed|Thesis/dissertation

Multi-physics Modeling for Molten Salt Reactors (MSRs)

by

Jun Shi

A dissertation submitted in partial satisfaction of the

requirements for the degree of

Doctor of Philosophy

in

Engineering- Nuclear Engineering

in the

Graduate Division

of the

University of California, Berkeley

Committee in charge:

Professor Massimiliano Fratoni, Chair
Professor Jasmina Vujic
Professor Christine Parlour

Summer 2021

Multi-physics Modeling for Molten Salt Reactors (MSRs)

Abstract

Multi-physics Modeling for Molten Salt Reactors (MSRs)

by

Jun Shi

Doctor of Philosophy in Engineering- Nuclear Engineering

University of California, Berkeley

Professor Massimiliano Fratoni, Chair

The concept of a molten salt reactor (MSR) originated at Oak Ridge National Laboratory (ORNL), under the direction of Alvin Weinberg. In the 1960s, the Molten Salt Reactor Experiment (MSRE) operated successfully for five years and demonstrated the viability and safety of such concept. Recently, MSRs have attracted world's attention again as part of the six reactor technologies selected for further research and development by the Generation IV International Forum (GIF).

Modeling of liquid-fueled molten salt reactors involves the simulation of peculiar phenomena whose treatment is not readily available in common reactor physics tools as these are typically developed with stationary solid fuel in mind. In particular, the effect related to delayed neutron precursor circulation, the impact of compressibility on pressure wave propagation in liquid salt, and the consequence of radiative heat transfer (RHT) within liquid salt need specific modeling and simulation capabilities.

The purpose of this work is to develop multi-physics high-fidelity MSR models which are able to analyze phenomena peculiar to the liquid-fueled MSR. Since no MSR has been built yet, with the exception of the MSRE, high-fidelity models can help to better understand the significance and impact of these phenomena on the performance and safety of MSRs. Furthermore, high-fidelity tools and models can provide reference data for low-fidelity (less computational demanding) models/tools verification if experimental data are not available.

Two MSR models, based on the Molten Salt Reactor Experiment and the Molten Salt Fast Reactor (MSFR), respectively, were developed using the Monte Carlo particle transport code Serpent 2 and the multi-physics code GeN-Foam. The MSRE GeN-Foam model was used to study the effect of delayed neutron precursor drift. When fuel moves rapidly through the core, delayed neutron precursors decay in a different location as compared to the one they are generated. This leads to delayed neutrons being emitted in lower importance regions of the core or even outside of the core, leading to a lower neutron multiplication factor and a

lower effective delayed neutron fraction. A multi-physics model of the MSRE that couples fuel flow and neutronics, as well as an adjoint solver to calculate the effective delayed neutron fraction, was developed and the results showed close agreement with the experimental values from the MSRE. The MSFR GeN-Foam model was used to study the effects of fuel salt compressibility and radiative heat transfer in MSRs. During a reactivity-initiated accident, negative reactivity is obtained from the Doppler effect but also from the salt expanding and exiting the core region. The latter effect is unique to liquid fuel, but failing to recognize the impact of the salt compressibility alters its nature. The assumption of incompressible salt, although usually acceptable in core simulations, makes the reactivity feedback prompt. In reality, this feedback is delayed and depends on the speed that the pressure waves propagate through salt. The effect of the salt compressibility was studied in the MSFR using either fluoride salt or chloride salt. It was found that a larger power excursion occurs when salt compressibility is properly accounted for and this is more severe in chloride salt due to its harder neutron spectrum and shorter neutron prompt lifetime. Finally, preliminary results show that the impact of radiative heat transfer is not significant during a loss of flow accident in the MSFR.

To my parents, Xiaoyun Tong and Kedeng Shi,
who introduced me to the field of Nuclear Engineering

When I was a kid,
I never thought I would go abroad,
study in the United States, and graduate with a Ph.D. degree.
Your continued support - spiritually and financially - made all of this possible.

I LOVE YOU!

Contents

List of Figures

List of Tables

List of Symbols

α	Thermal expansion coefficient	$[\mathrm{K}^{-1}]$
α_a	Albedo coefficient	[-]
α_T	Turbulent thermal diffusivity	$[\mathrm{kg\,m^{-1}\,s^{-1}}]$
$\alpha_{f/c}$	Linear expansion coefficient of fuel or cladding	$[\mathrm{K}^{-1}]$
β	Total delayed neutron fraction	[-]
β_k	Delayed neutron fraction for the k^{th} delayed neutron precursor group	[-]
β_S	Isentropic compressibility	$[\mathrm{m\,s^2\,kg^{-1}}]$
β_T	Isothermal compressibility	$[\mathrm{m\,s^2\,kg^{-1}}]$
$\beta_{eff,k}$	Effective delayed neutron fraction for the k^{th} delayed neutron precursor group	[-]
β_{eff}	Total effective delayed neutron fraction	[-]
$\boldsymbol{\kappa(u_D)}$	Tensor defined in Equation (2.8)	$[\mathrm{N\,m^{-4}\,s}]$
$\boldsymbol{F_g}$	Volumetric force due to gravity	$[\mathrm{N\,m^{-3}}]$
$\boldsymbol{F_{ss}}$	Volumetric force due to the interaction with the sub-scale structure	$[\mathrm{N\,m^{-3}}]$
$\boldsymbol{u_D}$	Darcy fluid velocity	$[\mathrm{m\,s^{-1}}]$
$\boldsymbol{u}$	Velocity	$[\mathrm{m\,s^{-1}}]$
$\boldsymbol{v_f}$	Axial orientation of fuel	[-]
$\chi_{d,i}$	Delayed neutron yield for the i^{th} energy group	[-]
$\chi_{p,i}$	Prompt neutron yield for the i^{th} energy group	[-]
$\dot{Q}_f$	Heat source in fuel	$[\mathrm{W\,m^{-3}}]$
$\dot{Q}_{ss}$	Heat transferred from the sub-scale structure to the fluid	$[\mathrm{W\,m^{-3}}]$

ϵ	Emissivity coefficient	[-]
γ	Porosity or void fraction	[-]
$\kappa(u_D)_{ii}$	Component of $\boldsymbol{\kappa(u_D)}$ in the i^{th} principal direction of the sub-scale structure	$[\mathrm{N\,m^{-4}\,s}]$
λ	Thermal conductivity	$[\mathrm{W\,m^{-1}\,K^{-1}}]$
λ_k	Decay constant for the k^{th} delayed neutron precursor group	$[\mathrm{s^{-1}}]$
μ	Dynamic viscosity	$[\mathrm{Pa\,s}]$
μ_T	Turbulent dynamic viscosity	$[\mathrm{Pa\,s}]$
ν	Average number of neutrons produced per fission	[-]
ν_i	Average number of neutrons produced per fission for the i^{th} energy group	[-]
ν_T	Turbulent kinematic viscosity	$[\mathrm{m^2\,s^{-1}}]$
ϕ	Neutron flux	$[\mathrm{m^{-2}\,s^{-1}}]$
ϕ^*	Adjoint neutron flux	$[\mathrm{m^{-2}\,s^{-1}}]$
ϕ_i^*	Adjoint neutron flux for the i^{th} energy group	$[\mathrm{m^{-2}\,s^{-1}}]$
ϕ_i	Neutron flux for the i^{th} energy group	$[\mathrm{m^{-2}\,s^{-1}}]$
ρ	Density	$[\mathrm{kg\,m^{-3}}]$
ρ_0	Reference density	$[\mathrm{kg\,m^{-3}}]$
ρ_c	Density of cladding	$[\mathrm{kg\,m^{-3}}]$
ρ_f	Density of fuel	$[\mathrm{kg\,m^{-3}}]$
ρ_{gas}	Density of the gas bubble	$[\mathrm{kg\,m^{-3}}]$
ρ_{salt}	Density of salt	$[\mathrm{kg\,m^{-3}}]$
ρ_{ss}	Density of the sub-scale structure	$[\mathrm{kg\,m^{-3}}]$
σ	Scattering coefficient	$[\mathrm{m^{-1}}]$
σ_{eff}	Effective scattering coefficient	$[\mathrm{m^{-1}}]$
$\Sigma_{f,i}$	Macroscopic fission cross section for the i^{th} energy group	$[\mathrm{m^{-1}}]$
$\Sigma_{r,i}$	Macroscopic removal cross section for the i^{th} energy group	$[\mathrm{m^{-1}}]$

$\Sigma_{s,i'\rightarrow i}$	Macroscopic group-transfer cross section from the i'^{th} to the i^{th} energy group	$[\mathrm{m}^{-1}]$
σ_{SB}	Stefan-Boltzmann Constant	$[\mathrm{W\,m^{-2}\,K^{-4}}]$
ε	Dissipation rate of turbulent kinetic energy	$[\mathrm{m^2\,s^{-3}}]$
a	Absorption coefficient	$[\mathrm{m}^{-1}]$
A_V	Volumetric area	$[\mathrm{m}^{-1}]$
$A_{f_{D,i}}$	Constant defined in Equation (2.10)	[-]
$A_{Nu,i}$	Constant defined in Equation (2.14)	[-]
$B_{f_{D,i}}$	Constant defined in Equation (2.10)	[-]
$B_{Nu,i}$	Constant defined in Equation (2.14)	[-]
C	Concentration of delayed neutron precursors	$[\mathrm{m}^{-3}]$
c	Speed of sound	$[\mathrm{m\,s^{-1}}]$
C^*	Importance of delayed neutron precursors	$[\mathrm{m^{-2}\,s^{-1}}]$
C_k^*	Importance of the k^{th} delayed neutron precursor group	$[\mathrm{m^{-2}\,s^{-1}}]$
C_k	Concentration of the k^{th} delayed neutron precursor group	$[\mathrm{m}^{-3}]$
c_p	Specific heat capacity	$[\mathrm{J\,kg^{-1}\,K^{-1}}]$
c_{mix}	Speed of sound in the liquid-gas mixture	$[\mathrm{m\,s^{-1}}]$
$C_{Nu,i}$	Constant defined in Equation (2.14)	[-]
$c_{p,c}$	Specific heat capacity of cladding	$[\mathrm{J\,kg^{-1}\,K^{-1}}]$
$c_{p,f}$	Specific heat capacity of fuel	$[\mathrm{J\,kg^{-1}\,K^{-1}}]$
$c_{p,ss}$	Specific heat capacity of the sub-scale structure	$[\mathrm{J\,kg^{-1}\,K^{-1}}]$
C_{P1}	Linear-anisotropic phase function coefficient	[-]
D_f	Fuel displacement field	[m]
D_h	Hydraulic diameter of the sub-scale structure	[m]
D_i	Neutron diffusion coefficient for the i^{th} energy group	[m]
$D_{Nu,i}$	Constant defined in Equation (2.14)	[-]

D_{P1}	Diffusion coefficient in the "P1" radiation model	[m]
E	Emission contribution	$[\mathrm{W\,m^{-3}}]$
e	Emission coefficient defined in Equation (2.29)	$[\mathrm{m^{-1}}]$
e	Fluid total energy defined in Equation (2.7)	$[\mathrm{J\,kg^{-1}}]$
$f_{D,i}$	Darcy friction factor in the i^{th} principal direction of the sub-scale structure	[-]
G	Incident radiation	$[\mathrm{W\,m^{-2}}]$
g	Gravitational acceleration constant	$[\mathrm{m\,s^{-2}}]$
H	Height	[m]
h	Heat transfer coefficient between the fluid and the sub-scale structure	$[\mathrm{W\,m^{-2}\,K^{-1}}]$
h_i	Heat transfer coefficient in the i^{th} principal direction of the sub-scale structure	$[\mathrm{W\,m^{-2}\,K^{-1}}]$
h_{eff}	Heat transfer coefficient between the fluid and an external heat sink	$[\mathrm{W\,m^{-2}\,K^{-1}}]$
h_{ext}	External heat transfer coefficient	$[\mathrm{W\,m^{-2}\,K^{-1}}]$
K	Bulk modulus	$[\mathrm{kg\,m^{-1}\,s^{-2}}]$
k	Turbulent kinetic energy	$[\mathrm{m^2\,s^{-2}}]$
k_c	Conductivity of cladding	$[\mathrm{W\,m^{-1}\,K^{-1}}]$
k_f	Conductivity of fuel	$[\mathrm{W\,m^{-1}\,K^{-1}}]$
k_T	Turbulent conductivity	$[\mathrm{W\,m^{-1}\,K^{-1}}]$
k_{eff}	Effective multiplication factor	[-]
K_{gas}	Bulk modulus of the gas bubble	$[\mathrm{kg\,m^{-1}\,s^{-2}}]$
K_{salt}	Bulk modulus of salt	$[\mathrm{kg\,m^{-1}\,s^{-2}}]$
k_{ss}	Conductivity of the sub-scale structure	$[\mathrm{W\,m^{-1}\,K^{-1}}]$
L_i	Diffusion length for the i^{th} energy group	[m]
Nu_i	Nusselt number in the i^{th} principal direction of the sub-scale structure	[-]
p	Pressure	[Pa]
p_0	Reference pressure	[Pa]

Pr	Prandtl number	[-]
r	Radial distance	[m]
Re	Reynolds number	[-]
$Rp()$	Source term component (for the power of T^4) in Equation (2.27)	$[\mathrm{W\,m^{-3}\,K^{-4}}]$
$Ru()$	Source term component (constant) in Equation (2.27)	$[\mathrm{W\,m^{-3}}]$
$Sh()$	Radiation source term in Equation (2.27)	$[\mathrm{W\,m^{-3}}]$
T	Temperature	[K]
t	Time	[s]
T_0	Reference temperature	[K]
T_c	Temperature of cladding	[K]
T_f	Temperature of fuel	[K]
T_{ext}	Temperature of an external heat sink	[K]
$T_{f/c,ref}$	Reference temperature in fuel or cladding	[K]
$T_{f/c}$	Temperature in fuel or cladding	[K]
T_{ss}	Temperature of the sub-scale structure	[K]
$u_{D,i}$	Darcy fluid velocity in the i^{th} principal direction of the sub-scale structure	$[\mathrm{m\,s^{-1}}]$
v_i	Average neutron velocity for the i^{th} energy group	$[\mathrm{m\,s^{-1}}]$

Acknowledgments

Firstly, I would like to express my sincere gratitude to my advisor Prof. Massimiliano Fratoni for the continued support of my Ph.D. study and related research, for his patience, motivation, and immense knowledge. His guidance helped me during all the time of research and writing of this thesis. I could not have imagined having a better advisor and mentor for my Ph.D. study.

Besides my advisor, I would like to thank the rest of my thesis committee: Prof. Jasmina Vujic and Prof. Christine Parlour, for their insightful comments and encouragement, but also for the hard question which incented me to widen my research from various perspectives.

My sincere thanks also goes to Dr. Carlo Fiorina, who provided me an opportunity to use GeN-Foam code and helped me better understand the basis of this code. Without his precious support it would not be possible to conduct this research.

Chapter 1

Introduction

1.1 Background on Molten Salt Reactors

In the late 1940s, investigation of molten salt reactors started as a part of the United States' program to develop a nuclear-powered bomber. During the 1950s, the research interest of MSRs was moved from military purpose to civilian power applications. During the 1960s at Oak Ridge National Laboratory (ORNL), a small prototype 8 MWt Molten Salt Reactor Experiment (MSRE) was built and successfully operated for 5 years (from 1965 to 1969). The MSR research reached its peak during this period of time, as well as the beginning of 1970s. Since the mid of 1970s, due to the shortage of funding and the shift of research focus to other nuclear reactor designs, MSRs had lost its momentum [25]. Today, most nuclear power plants in the world have installed light water reactors (LWRs), but according to Dolan's book *Molten Salt Reactors and Thorium Energy* [7], LWRs have the following disadvantages:

- New fuel must be added every 1-3 years, due to low fissile breeding by ^{238}U;
- Proliferation concern of ^{239}Pu in used fuel;
- Temperature usually limits thermal efficiency to $< 35\%$;
- Danger of pressure vessel failure, due to high-pressure coolant;
- High core radioactivity, which is a large source term in accidents;
- High-level waste disposal issues;
- Limits of fuel and cladding life, due to radiation damage;
- High excess core reactivity and careful power control, due to ^{135}Xe poisoning;
- Present once-through fuel cycle utilizes $< 2\%$ of potential uranium energy and produces a large volume of high-level radioactive waste;

- Danger of steam explosion (Chernobyl accident);
- Danger of fuel melting (Three Mile Island and Fukushima accidents);
- Potential hydrogen generation during accidents (Fukushima accident).

The molten salt reactor has the potential to alleviate all of these problems and provide a path towards clean and sustainable nuclear energy. Therefore, in 2002, after decades of discontinuance, this concept was selected by the Generation IV International Forum (GIF), as one of the six reactor concepts, for further detailed study. MSRs use molten salt as fuel and/or coolant, and there are two primary variants of the MSR:

- Liquid-fueled MSR: fuel is dissolved in the molten salt.
- Solid-fueled MSR: salt only serves as the coolant.

The MSR concept covers thermal and fast reactors, operated with $U/^{239}Pu$ or a $Th/^{233}U$ fuel cycle, or as trans-uranium (TRU) burners. Depending on the the fuel cycle, MSRs can re-use fissile and fertile materials from LWRs, or they can use uranium, or burn plutonium or minor actinides. MSRs are operated at low pressure (slightly above atmospheric pressure) and are designed to be fail-safe. Also, they have increased power conversion efficiency because fission reactions directly occur in the carrier salt and transfer their heat to the coolant salt in heat exchangers. MSRs can be deployed as large power reactors or as small modular reactors (SMRs), and the deployment is limited by technological challenges, e.g., high temperature, structural materials, corrosion, etc [15].

1.2 Worldwide Activities on Molten Salt Reactors

Various countries, groups and institutions actively participate in the development of MSR designs and prospects, and some worldwide activities are summarized in this section [7].

China is currently leading the global research. China Academy of Sciences (CAS) initiated a thorium molten salt reactor (TMSR) research project in January 2011 and claimed to have the world's largest national effort on it. The TMSR development consists of two streams - a liquid-fueled thorium molten salt reactor (TMSR-LF) and a solid-fueled thorium molten salt reactor (TMSR-SF), and they have been designed for thorium-based nuclear energy utilization and hybrid nuclear energy applications.

Encouraged by the successful MSRE at Oak Ridge National Laboratory in the 1960s, the United States also has a lot of ongoing research in the MSR field. The U.S. Department of Energy collaborates with China Academy of Sciences to facilitate the development of fluoride salt-cooled high-temperature reactors (FHRs). An integrated research project (IRP), led by Massachusetts Institute of Technology (MIT), the University of California at Berkeley (UCB) and the University of Wisconsin (UW), has completed a 3-year study (analysis and experiments) to develop the FHR concept and a pathway to commercialization.

The Molten Salt Laboratory at Ohio State University (OSU) evaluates the thermodynamics and transport properties of lanthanides in molten salts for molten salt recycling, which can also be used to characterize the molten salt corrosion. The Nuclear Engineering (NE) Department of the University of Tennessee at Knoxville (UTK) models the fuel cycle of denatured molten salt reactor (DMSR) using low-enriched uranium (LEU) without reprocessing, and checks the dynamical stability of the core as a function of burn-up. The University of Utah's Metallurgical Engineering Department studies the pyroprocessing of nuclear fuel with projects in safeguards, actinide separations, and waste management for fuel cycles of the thorium-uranium fluoride salt fuel-based molten salt reactor. The research focus at Pennsylvania State University (PSU) is electrochemical separation of alkali/alkaline-earths (Ba, Sr, and Cs) in liquid metals with an ultimate goal to enable salt recycling by electrochemical separation of fission products and reduce the nuclear waste volume. Missouri University of Science and Technology (Missouri S&T) explores the possibilities of initial fuel for the TMSR. TerraPower and Southern Company Services, in cooperation with ORNL, Electric Power Research Institute, and Vanderbilt University, are developing a liquid-fueled molten chloride fast reactor (MCFR). Martingale Company is designing the ThorCon MSR, which does not require new technology and is a straightforward scale-up of Oak Ridge MSRE. Transatomic Power aims to develop a single-fluid MSR using very low-enriched uranium fuel (1.8%), which can safely burn all used LWR fuel and reduce the need for underground disposal. Flibe Energy is designing a liquid fluoride thorium reactor (LFTR). Elysium Industries is developing the molten chloride salt fast breeder reactor (MCSFR) with fuel in chloride salt.

The work described in this thesis was performed in the context of Nuclear Science, Technology and Education for Molten Salt Reactors (NuSTEM) project, which was funded by the U.S. DOE's Nuclear Energy University Program as an Integrated Research Program (October 2017 - September 2020). Principal participators include researchers from Texas A&M University, the University of California - Berkeley, and the University of Wisconsin - Madison. The NuSTEM project is centered on two intertwined themes [26]:

- The technical thrust has five mission areas: material and corrosion science, chemical technologies, modeling and multi-physics simulation, thermal-hydraulics science, and cross-section measurements. These technical missions will enable and develop the new technologies needed for the advancement of molten salt reactors.

- The educational thrust includes a collaboration with Safety Assessment of the Molten Salt Fast Reactor (SAMOFAR) project, which is one of the major research and innovation projects in the Horizon 2020 Euratom (European Atomic Energy Community) research program. This educational mission will draw upon research, incorporate results into courses and curriculum, inform and attract young students and professionals into science, engineering and mathematics, and develop the next generation of nuclear experts.

1.3 Peculiar Phenomena in Liquid-fueled Molten Salt Reactors

Liquid-fueled MSRs are different from traditional solid-fueled nuclear reactors and are usually defined as a non-classical reactor type because of the specific nature of the fuel, which is typically constituted by a molten salt mixture (e.g., fluoride salt, chloride salt, etc.) circulating in the primary circuit. The fission materials (uranium and/or transuranium elements) are dissolved in the molten salt carrier, which is also used as a coolant. For the modeling and simulation of liquid-fueled MSRs, there are three peculiar phenomena whose treatment is not available in common reactor physics tools: (1) the effect related to delayed neutron precursor drift, (2) the impact of compressibility on pressure wave propagation in the liquid salt, (3) and the consequence of radiative heat transfer within the liquid salt.

Delayed neutron precursor drift

According to Duderstadt's book *Nuclear Reactor Analysis* [8] and Lamarsh's book *Introduction to Nuclear Engineering* [20], a typical nuclear fission reaction (e.g., ${}^{1}_{0}n + {}^{235}_{92}U \rightarrow {}^{236}_{92}U^{*} \rightarrow$ *fission reaction products*) produces a variety of reaction products, including the fission fragments and several neutrons (about 2.5 on average) as well as numerous gammas, betas, and neutrinos. A considerable amount of energy (about 200 MeV) is also released during this process. Those neutrons emitted in the fission event can be used to propagate a fission chain reaction, and most of them appear essentially instantaneously (on the order of 10^{-14} sec) after the fission event, which are referred to as prompt neutrons. However, there is a very small fraction of neutrons (less than 1%) referred to as delayed neutrons because they are emitted with an appreciable time delay (ranging from few milliseconds up to 55 sec for the longest-lived precursor ${}^{87}Br$) from the subsequent decay of radioactive fission products. A fission fragment, whose beta-decay yields a daughter nucleus which subsequently decays via delayed neutron emission, is referred to as a delayed neutron precursor (DNP). There are believed to be about 20 such precursors, which can be divided into different groups based on their characteristic half-lives. The delayed neutron fraction for the k^{th} DNP group, β_k, is defined as the fraction of all of the fission neutrons released in fission that appear as delayed neutrons in the k^{th} group. In other words, β_k is the absolute neutron yield of the k^{th} group divided by the average number of neutrons, both prompt and delayed, released per fission (ν). The total delayed neutron fraction, β, is the sum of all the β_k. Although the fraction of delayed neutrons in a fission reaction is very small, delayed neutrons are significantly important for the safe control of any nuclear reactor. In a fission reactor, the effective delayed neutron fraction, β_{eff}, denotes the effective fraction of delayed neutrons on the neutron multiplication, and the effectiveness can be weighted by the adjoint neutron flux.

In liquid-fueled MSRs, the effective delayed neutron fraction differs from the delayed neutron fraction because of two distinct reasons. The first reason (common to solid-fueled reactors) is that the emission spectrum of delayed neutrons is softer than prompt neutrons:

delayed neutrons have an initial energy between 0.3 MeV and 0.9 MeV with an average value of 0.4 MeV, and prompt neutrons have an initial energy between 1 MeV and 10 MeV with an average value of 2 MeV. Therefore, in thermal reactors delayed neutrons are less likely to be lost by leakage or by parasitic absorption (i.e., absorption of a neutron does not result in a fission) than prompt neutrons, so they are easier to be thermalized. On the other hand, delayed neutrons are less likely to cause fast fissions due to their low average energy. These effects tend to counteract each other and result in a difference in the importance of delayed and prompt neutrons. The second reason is due to the physics of nuclear fuel circulation in MSRs. The delayed neutron precursors are transported by the fluid flow in the fuel circuit and may decay in a low neutron importance region (e.g., boundary of the reactor core) and even out of the core. Spatial effect due to the fuel motion is more relevant and always reduces β_{eff}. Energy effect is, in general, of less relevance and may increase/reduce β_{eff}, according to the neutronics characteristics of the core. Therefore, the delayed neutron precursor drift complicates the calculation of the effective delayed neutron fraction as well as the modeling of reactor transient responses.

Fuel salt compressibility

Although incompressible fluids do not actually exist and all real fluids are compressible, liquid flows are almost always treated as incompressible because of their small compressibilities or insignificant change in density due to the pressure change. An incompressible approximation ignores pressure effects on the fluid density, as if the speed of sound is infinite ($c^2 = \frac{dp}{d\rho} \to \infty$ when $d\rho \to 0$), and this implies that the fluid density is instantaneously related to the fluid temperature. During a reactivity initiated accident (RIA) in fast-spectrum MSRs, the increase of reactor power results in a rapid rise of salt temperature, which introduces two pieces of negative reactivity feedback: (1) the Doppler effect related to the broadening of resonances in fertile isotopes that mainly increases the neutron absorption; (2) the thermal expansion of salt that increases the neutron leakage. Differently from the Doppler effect which occurs instantaneously, the propagation of pressure waves and full expansion of salt outside of the core usually take several milliseconds or more. Therefore, an incompressible assumption may not be suitable to accurately model MSR's transients with rapid salt expansion, and the salt compressibility effect should be taken into account. Some preliminary studies on the compressibility effects in the Molten Salt Fast Reactor (MSFR) with fluoride salt have been summarized in Cervi's paper [4], and the results show that an incompressible assumption significantly overestimates negative feedback during a prompt-supercritical scenario. It is expected that the effect of this phenomenon will be more prominent in the molten chloride reactor due to its harder neutron spectrum and shorter neutron prompt lifetime.

Radiative heat transfer (RHT)

According to Incropera's book *Fundamentals of Heat and Mass Transfer* [18], heat transfer (or heat) is thermal energy in transit due to a spatial temperature difference. Whenever

there exists a temperature difference in a medium or between media, heat transfer must occur. There are three different types of heat transfer processes: conduction, convection, and radiation. The heat transfer by conduction and convection requires the presence of a temperature gradient in some form of matter. In contrast, RHT does not require an intervening medium, and in fact, this process occurs most efficiently in a vacuum. Another distinguishing feature between radiation and the other two heat transfer methods is the difference in their temperature dependency. For most applications, conductive and convective heat transfer rate is linearly proportional to the temperature difference, but radiative heat transfer rate is generally proportional to the difference in temperature to the fourth (or higher) power. Therefore, as temperature level increases, RHT becomes more important and may dominate over conduction and convection at very high temperatures, e.g., in combustion applications and nuclear reactions, etc.

All matter emits radiation, and the nature of radiation is the propagation of a collection of particles termed photons or quanta. Alternatively, radiation may be viewed as the propagation of electromagnetic waves. The complete electromagnetic spectrum is delineated in Figure 1.1. Since electromagnetic waves of vastly different wavelengths carry very different amounts of energy, their behavior is often quite different. The intermediate portion of the spectrum, which extends from approximately 0.1 μm to 100 μm and includes a portion of the spectrum of the ultraviolet (UV) and all of the visible and infrared (IR), is termed thermal radiation because it is both caused by and affects the thermal state or temperature of matter. For this reason, thermal radiation is pertinent to heat transfer.

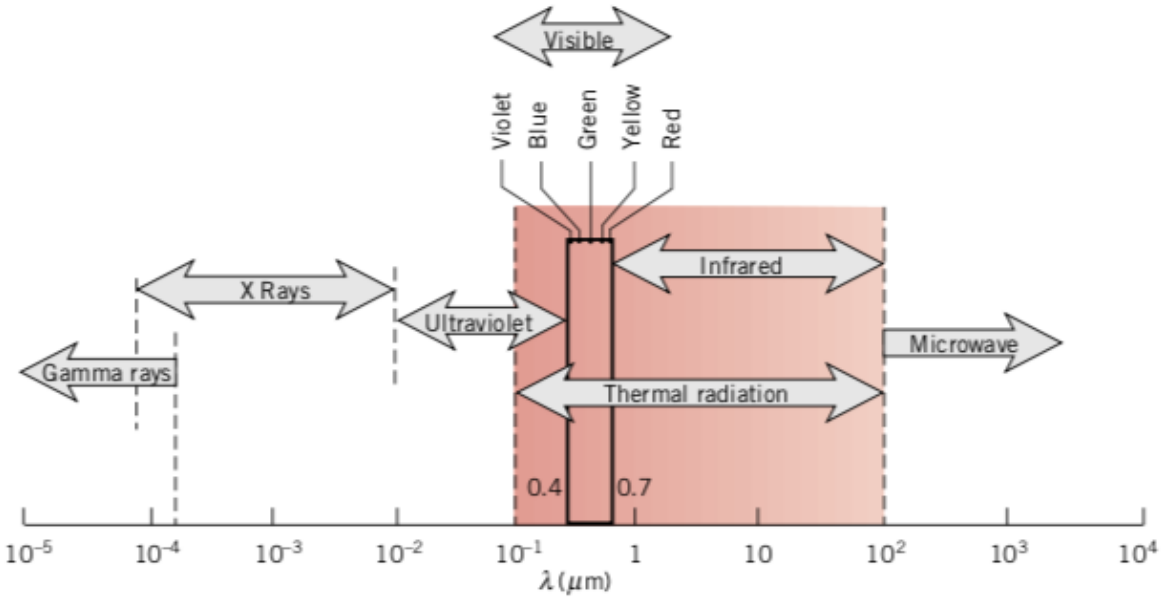

Figure 1.1: Spectrum of electromagnetic radiation [18].

According to Modest's book *Radiative Heat Transfer* [24], when an electromagnetic wave

traveling through a medium (or vacuum) strikes the surface of another medium (solid or liquid surface, particle or bubble), the wave may be reflected (either partially or totally), and any non-reflected part will penetrate into the medium. While passing through the medium the wave may become continuously attenuated. If attenuation is complete so that no penetrating radiation reemerges, the medium is known as opaque. If a wave passes through a medium without any attenuation, the medium is termed transparent, while a body with partial attenuation is called semitransparent. Whether a medium is transparent, semitransparent or opaque depends on the material as well as on its thickness (i.e., the distance the electromagnetic wave must travel through the medium).

Some of the possible carrier salts in MSRs are transparent or semi-transparent to infrared radiation and visible light. This feature may have an impact on heat transfer mechanisms in MSR applications at high temperatures. For example, during a loss of flow accident, the raised salt temperature enhances RHT and improves decay heat removal, which is important in the transient analysis. According to the different salt compositions, the fluid may be opaque in specific bandwidths. Moreover, the production of non-soluble fission products and the dissolution of corrosion products may decrease the light's mean free path, resulting in a change of effective thermal conductivity of salt. For theses reasons, an accurate simulation of heat transfer in MSRs requires a detailed multi-physics model simultaneously including conduction, convection and radiation transport.

1.4 Molten Salt Reactor Experiment

This section provides a brief overview of the Molten Salt Reactor Experiment, and a more detailed description of the MSRE can be found in the original reports written by Oak Ridge National Laboratory, e.g., ORNL-TM-728 [30], ORNL-TM-3229 [19], ORNL-TM-380 [16], ORNL-4233 [29], etc.

In the 1960s, the MSRE was undertaken by ORNL to demonstrate the feasibility of constructing and operating a simple, reliable and safe nuclear reactor using the molten salt concept. This was the first large-scale, long-term, high-temperature test in a reactor environment of the fuel salt, graphite, moderator and high-nickel-base alloy (INOR-8). The operating data from the MSRE provided very valuable information on the study and design of molten salt reactors.

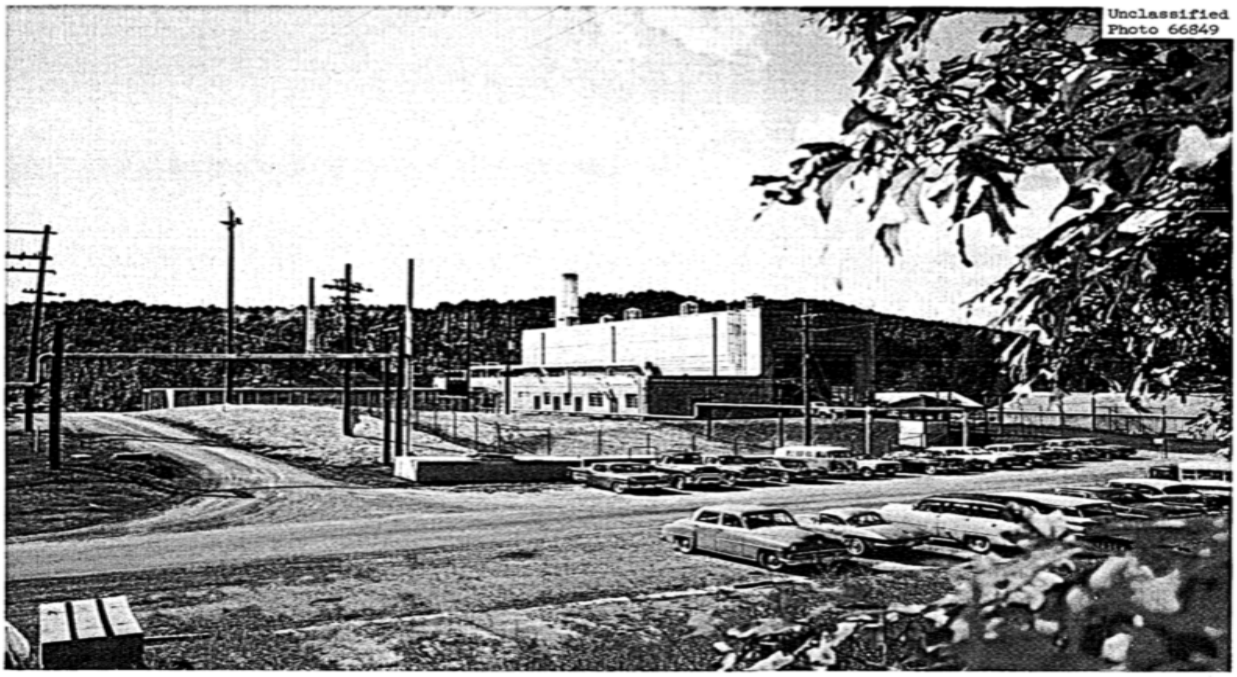

Figure 1.2: Front view of building 7503 [30].

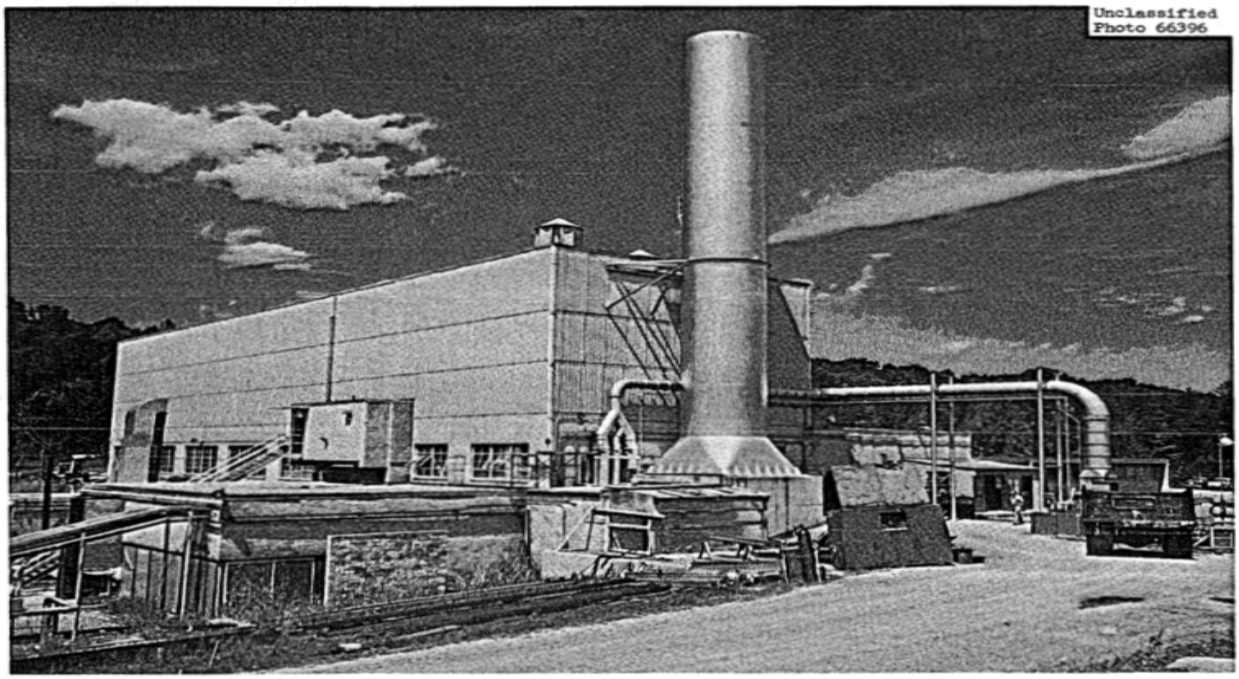

Figure 1.3: Rear view of building 7503 [30].

In July 1961, construction of the MSRE officially started in the 7503 Area of Oak Ridge National Laboratory, Oak Ridge, Tennessee (Figures 1.2 and 1.3), having in mind that most of the advance thinking and preliminary design work were well under way by that time. The MSRE is a single-region, unclad, graphite-moderated, fluid-fuel type of reactor with a design thermal power of 10 MW, and the major components in the MSRE are illustrated in Figure 1.4.

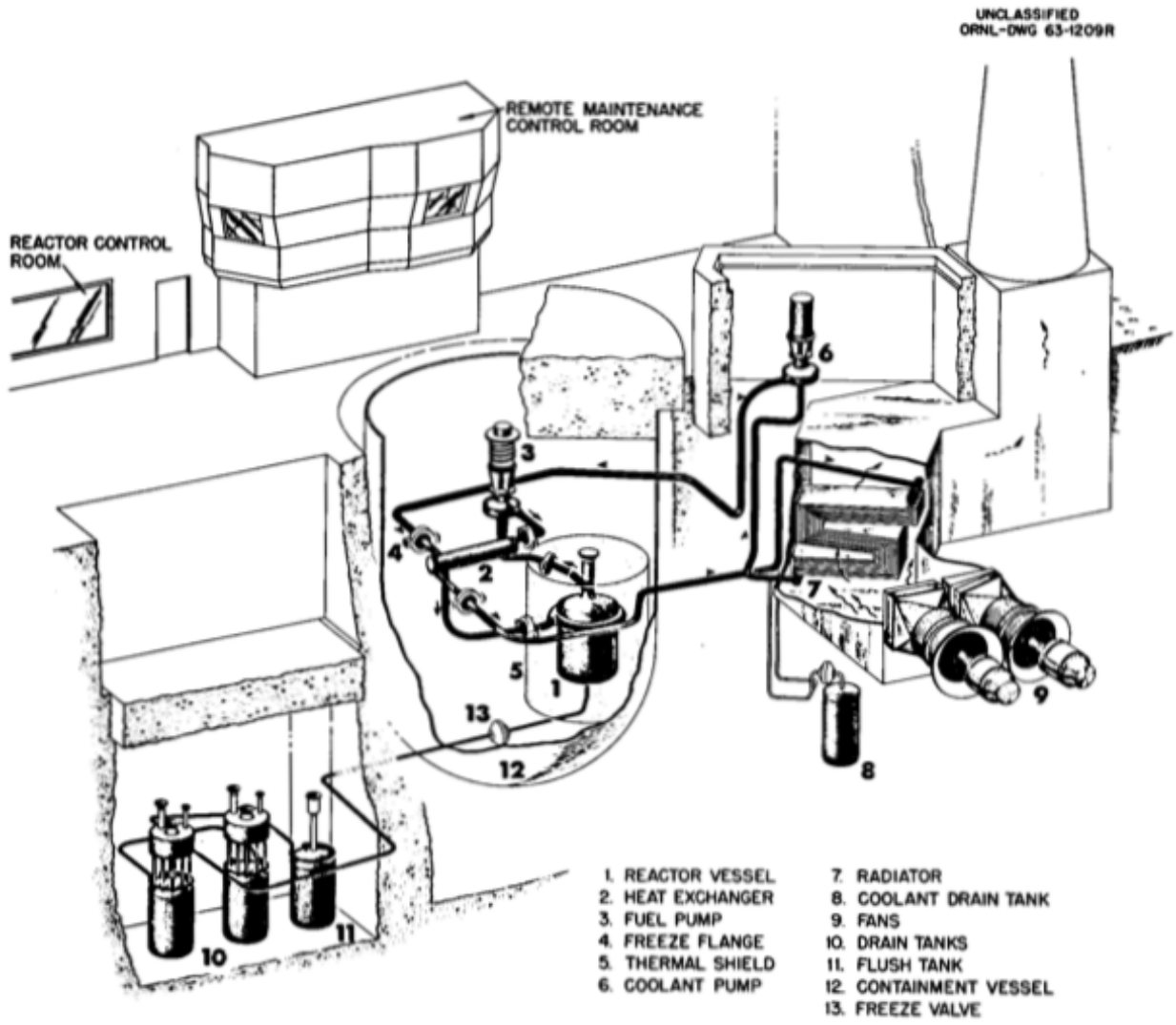

Figure 1.4: MSRE flow diagram [30].

The reactor primary system or fuel-salt-circulating system consists of the reactor vessel, the fuel heat exchanger (Figure 1.5), the fuel circulating pump (Figure 1.6) and the inter-

connecting piping. The reactor secondary system or coolant system consists of the coolant pump, the radiator (Figure 1.7), and the piping between the pump, the radiator, and the fuel heat exchanger. When circulating systems are not in operation, fuel and coolant salts are contained in the drain-tank system (Figure 1.8).

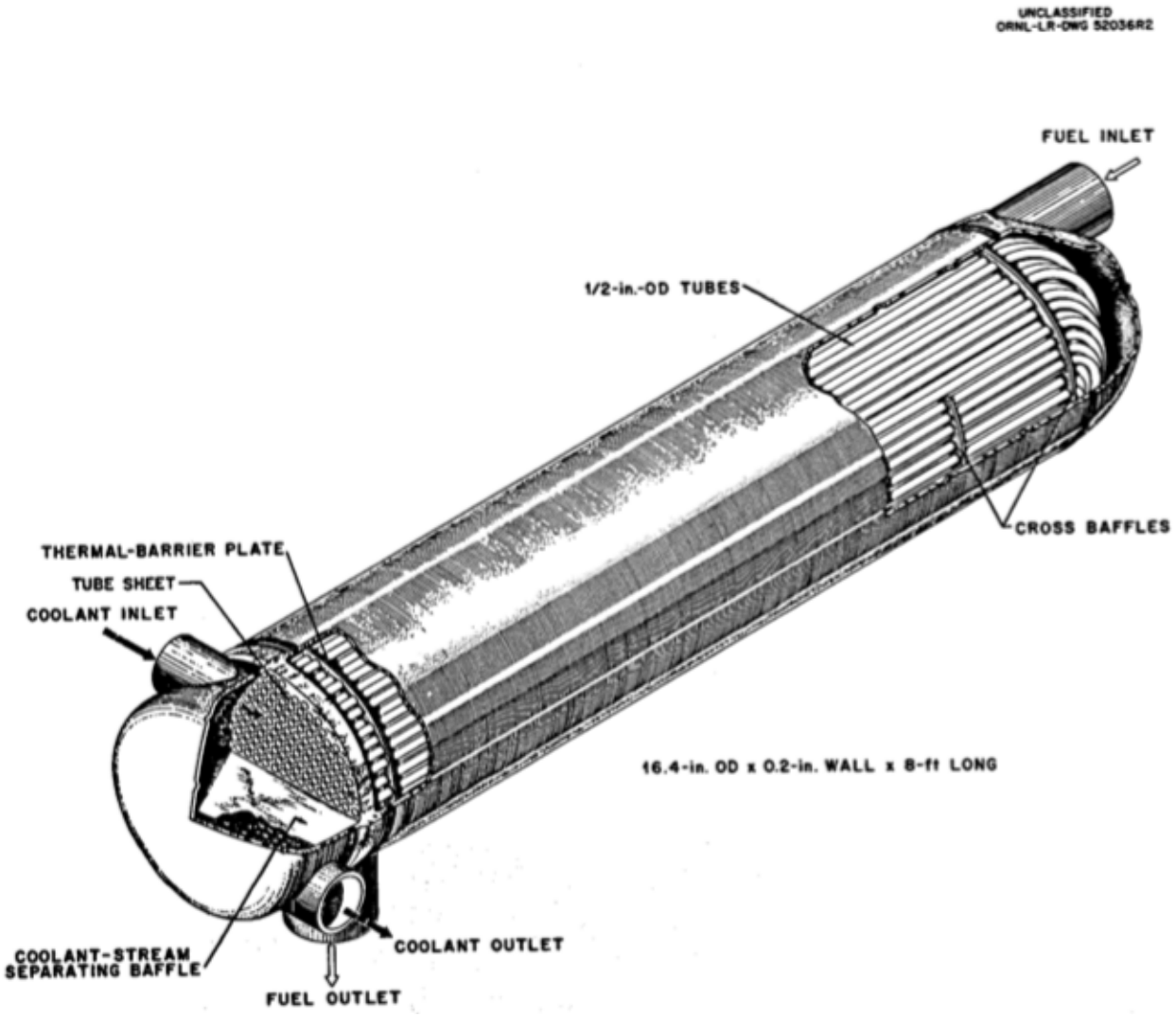

Figure 1.5: MSRE heat exchanger [30].

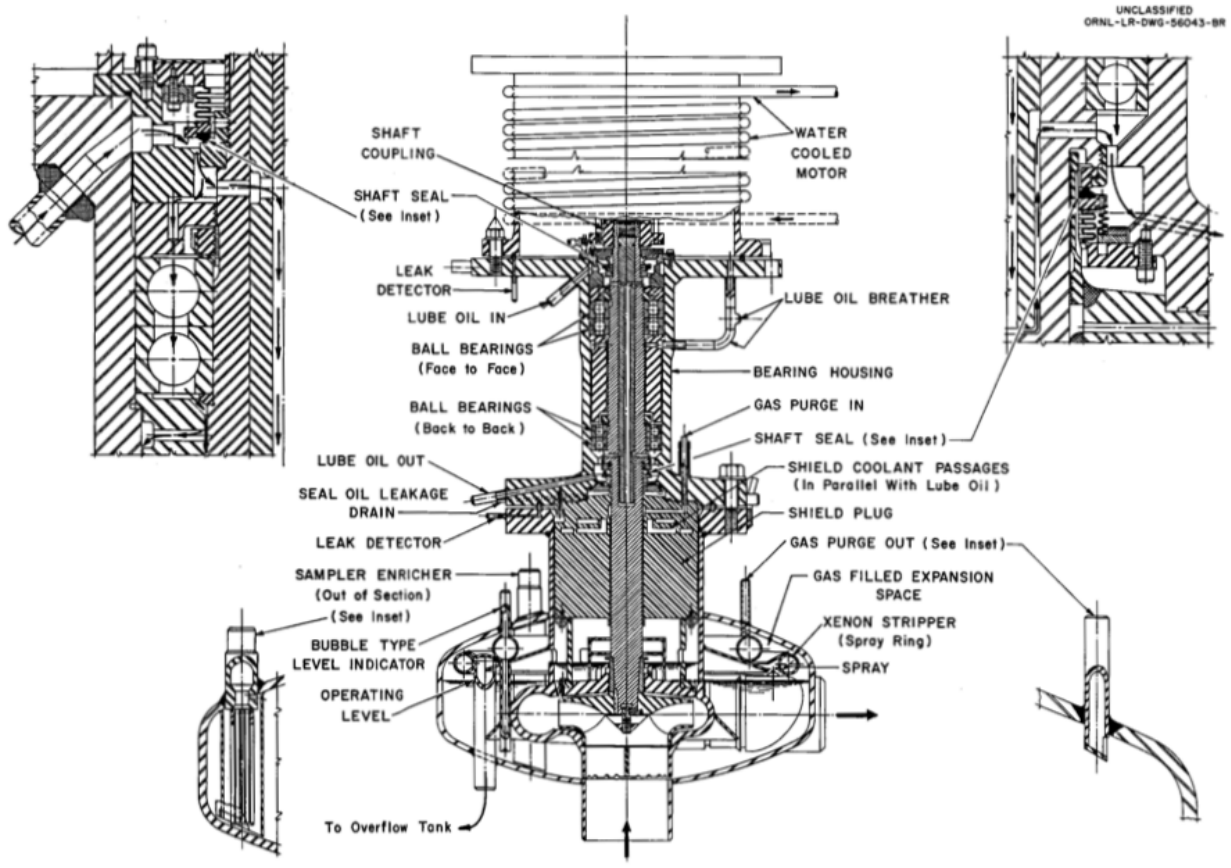

Figure 1.6: MSRE fuel pump [30].

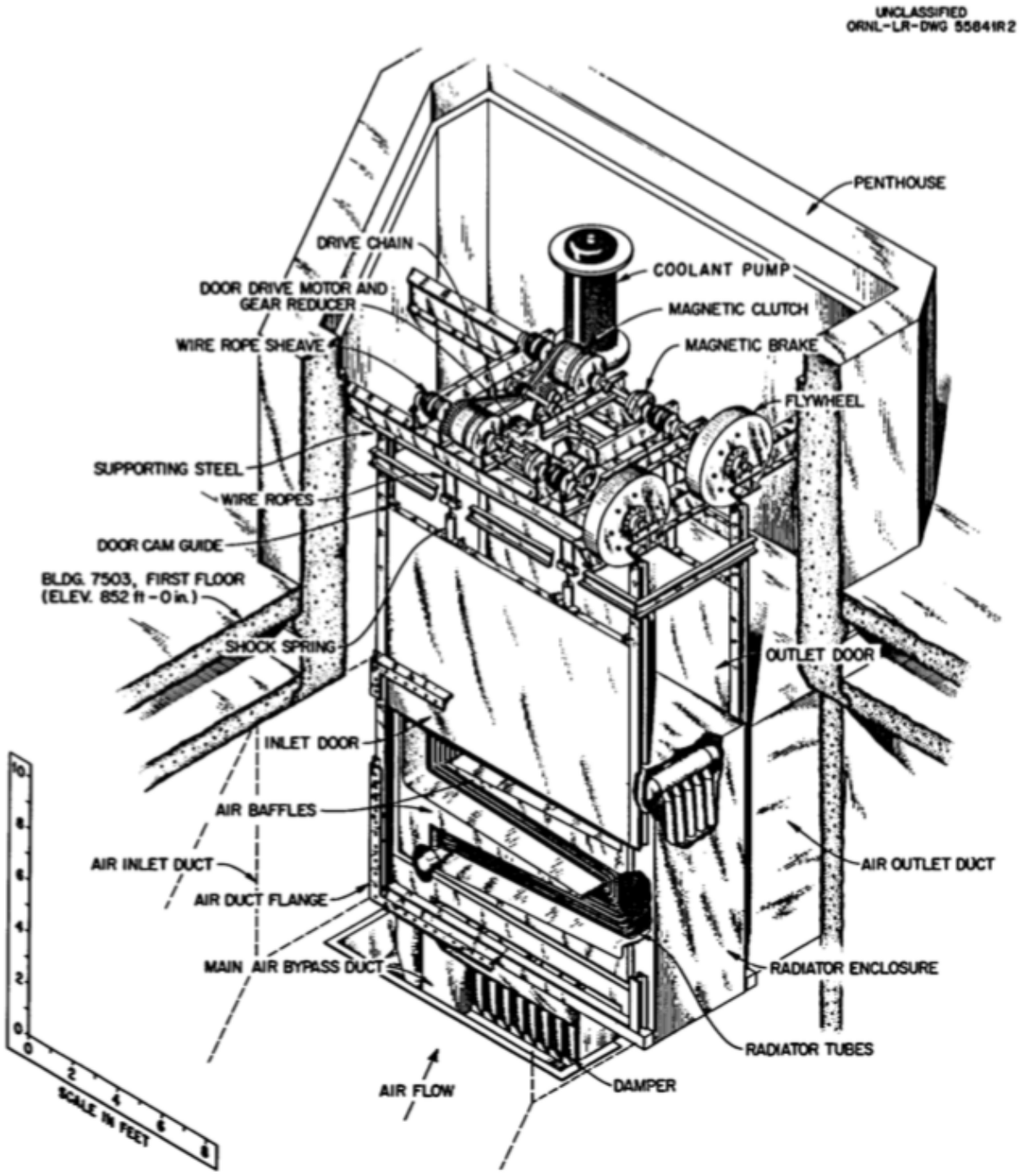

Figure 1.7: MSRE radiator [30].

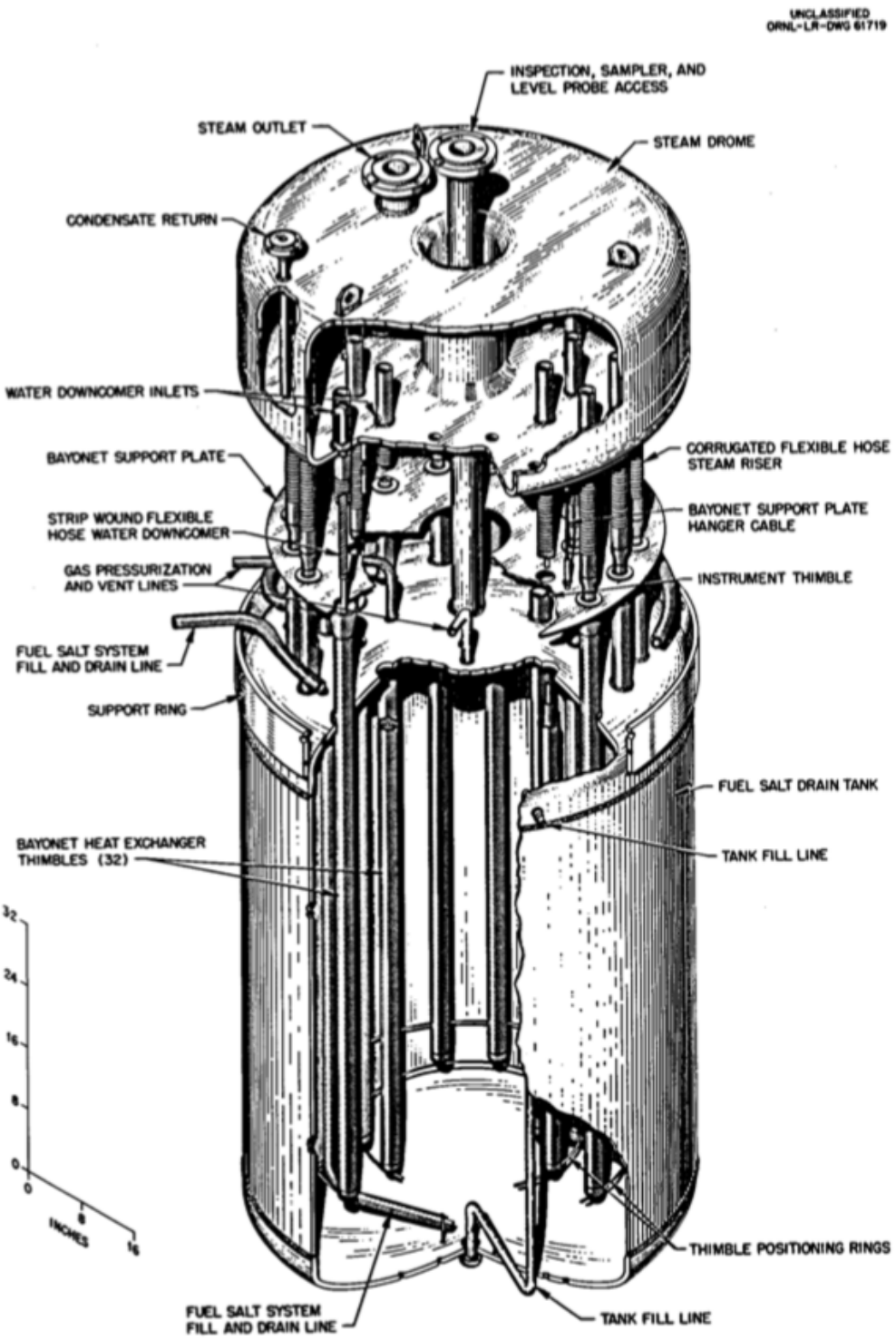

Figure 1.8: MSRE drain tank [30].

The reactor vessel is a 5-ft diameter by 8-ft height (152.4 cm x 243.84 cm) tank that contains a 55-in. diameter by 64-in. height (139.7 cm x 162.56 cm) graphite core structure. The cutaway drawing and the cross sectional view of the vessel are shown in Figures 1.9 and 1.10, respectively. The dimensions and design data of the reactor vessel and the core are summarized in Table 1.1.

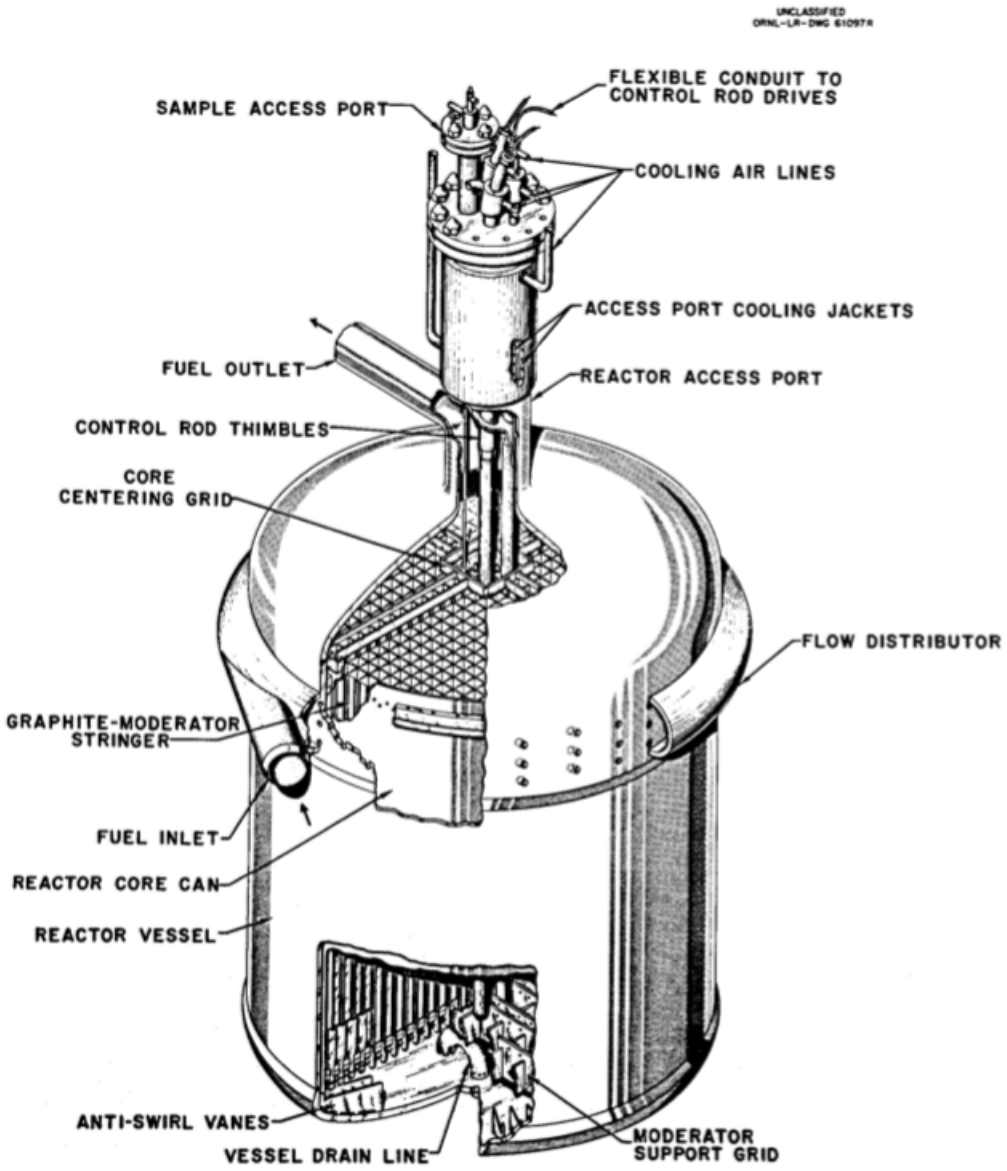

Figure 1.9: Cutaway drawing of MSRE reactor vessel [30].

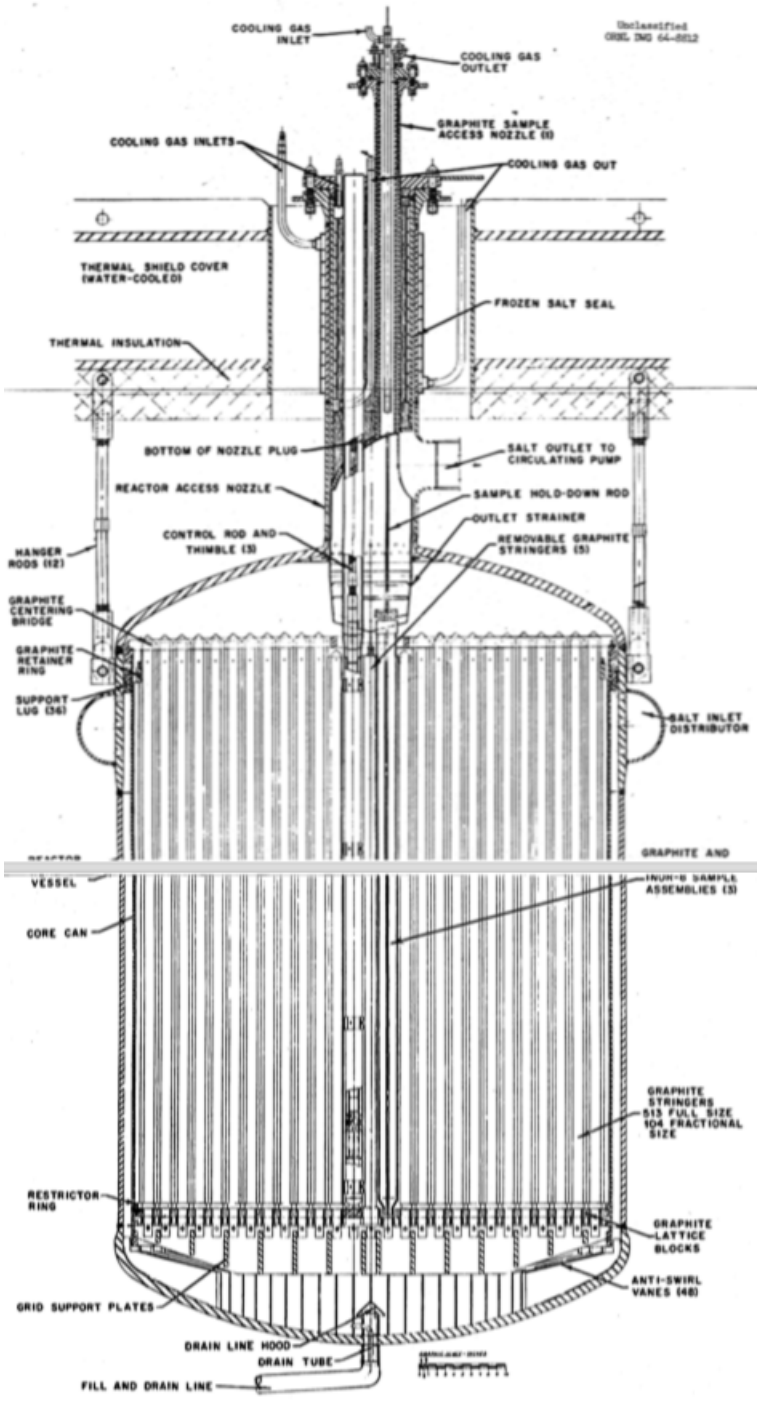

Figure 1.10: Cross sectional view of MSRE reactor vessel [30].

Table 1.1: MSRE reactor vessel and core design data and dimensions [30].

Construction Material	INOR-8
Inlet Nozzle, sched-40, in., Iron Pipe Size (IPS)	5
Outlet Nozzle, sched-40, in., IPS	5
Core Vessel	
Outside Diameter (OD), in.	59.125 (60 in. max)
Inside Diameter (ID), in.	58
Wall Thickness, in.	0.5625
Overall Height (to the centerline of fuel outlet nozzle), in.	100.75
Head Thickness, in.	1
Design Pressure, psi	50
Design Temperature, °F	1300
Fuel Inlet Temperature, °F	1175
Fuel Outlet Temperature, °F	1225
Inlet	Constant Area Distributor
Cooling Annulus ID, in.	56
Cooling Annulus OD, in.	58
Graphite Core	
Diameter, in.	55.25
Number of Fuel Channels (equivalent)	1140
Fuel Channel Size, in.	1.2 x 0.4 (rounded corners)
Core Container	
ID, in.	55.5
OD, in.	56
Wall Thickness, in.	0.25
Height, in.	68

At the design power of 10 MWth, the fuel salt first enters the flow distributor at the top of the vessel, and then it is distributed evenly around the circumference of the vessel and flows downward, in a spiral path through a 1-in. (2.54 cm) annulus between the vessel wall and the core can, to the lower plenum. Due to the swirl-straightening vanes installed in the lower plenum, the salt loses its rotational motion, turns and flows upward through the core. The core is formed of graphite stringers, which are shown in Figures 1.11 and 1.12. The salt leaves the reactor core and flows through the upper head to the 10-in. (25.4 cm) nozzle opening. It is diverted through a 5-in. (12.7 cm) opening in the side of the nozzle to flow to the fuel circulating pump, which operates at a speed of 1160 rpm (revolutions per minute) to deliver a volumetric flow rate of 1200 gpm (1200 gallons per minute = 0.0757 m^3/s). The salt discharged by the fuel pump flows through the shell side of the shell-and-tube heat exchanger, where it is cooled from 1225 °F (935.93 K) to 1175 °F (908.15 K). Finally, the

fuel salt from the heat exchanger is returned to the reactor vessel.

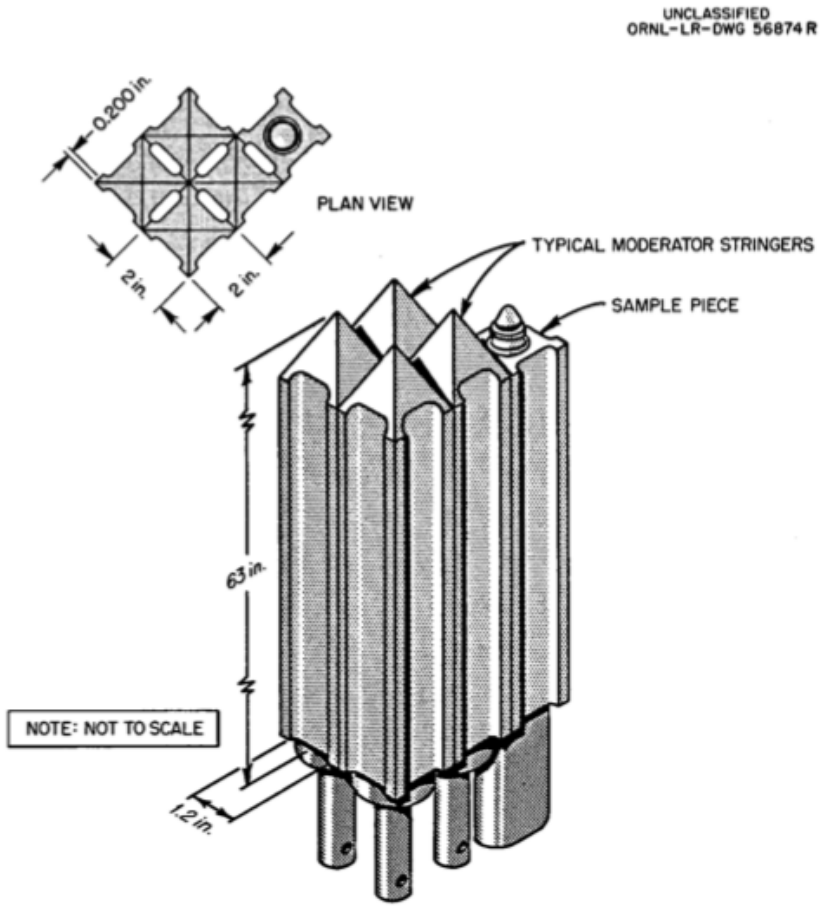

Figure 1.11: Graphite stringers in MSRE [30].

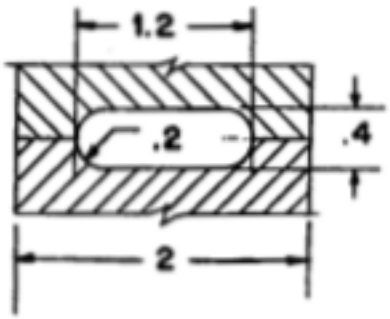

Figure 1.12: A Fuel channel in MSRE core [30].

Zero-power physics experiments on the MSRE

A program of zero-power nuclear experiments on the MSRE was conducted by ORNL to establish the basic nuclear characteristics of the reactor system and provide a baseline for the evaluation of system performance in the nuclear operation, as well as to evaluate the calculation techniques and models used in predicting properties of the MSRE.

The program began with an initial critical experiment, which found the minimum critical concentration of ^{235}U in the fuel under the simplest possible conditions (i.e., core isothermal, fuel salt stationary and control rods withdrawn to their upper limits). The salt was prepared in three lots: the carrier salt ($65LiF - 30BeF_2 - 5ZrF_4$ expressed as molar percentages), the eutectic ($73LiF - 27UF_4$) containing depleted uranium and the eutecic ($73LiF - 27UF_4$) containing highly enriched ^{235}U. The carrier salt and the eutectic having depleted uranium were mixed and circulated for ten days at 1200 °F (922.04 K) to establish the initial composition. Then the eutectic having enriched uranium was added in increments to make the reactor critical. At approximately 6:00 p.m., June 1, 1965, the reactor, containing 69.6 kg ^{235}U (1.408 ± 0.007 wt.%) in the fuel salt ($65LiF - 29.2BeF_2 - 5ZrF_4 - 0.8UF_4$ and density of 2.3275 ± 0.0160 g/cm^3 at 911 K), finally reached the critical point when the circulation was stopped and the rods were withdrawn.

Following the initial critical experiment, the fuel pump started to run, and additional ^{235}U was added into the fuel salt to keep the reactor at critical. The effect of each capsule addition was measured and analyzed in Figure 1.13. The vertical distance between two curves is 212 ± 4 pcm, which was due to the delayed neutron precursor decay in the part of the circulating system external to the core and the effective loss of delayed neutrons.

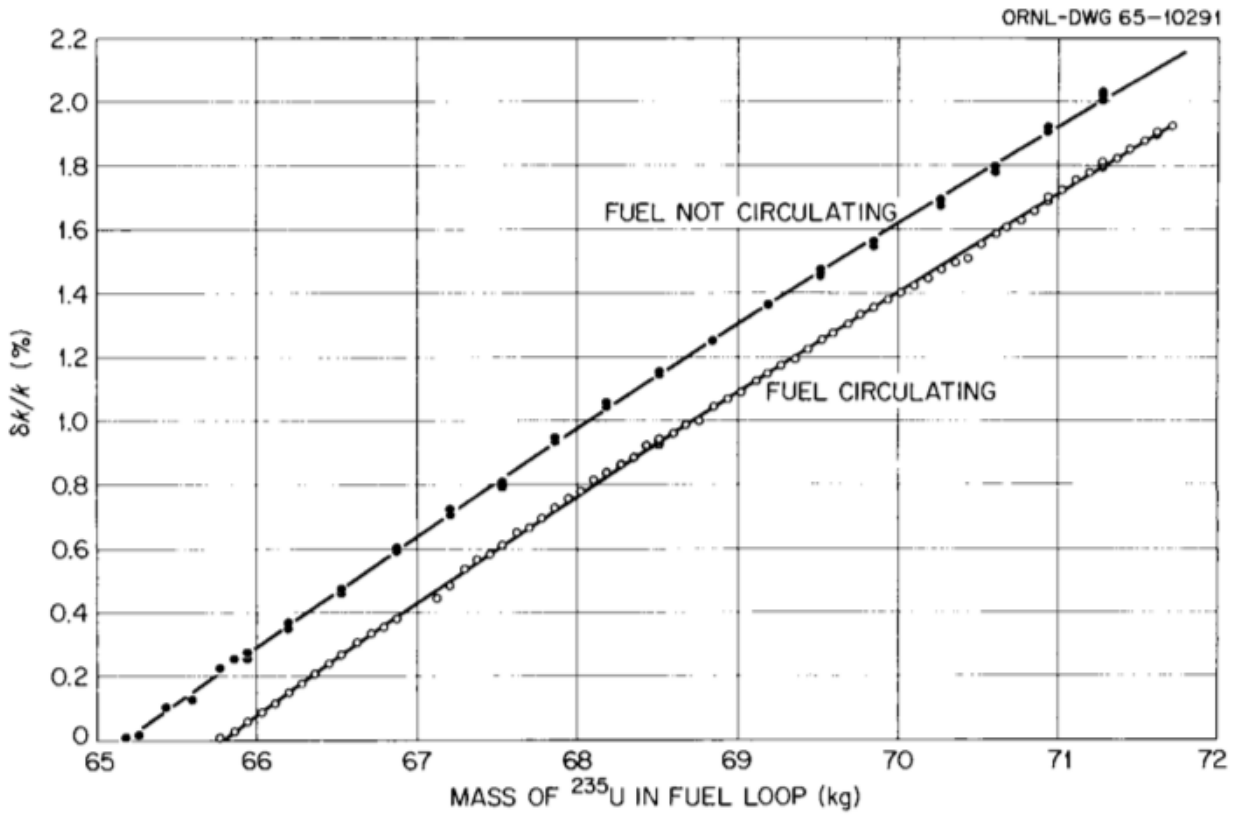

Figure 1.13: Effect of ^{235}U mass on reactivity [29].

1.5 Molten Salt Fast Reactor

Since 2005, the research focus on molten salt reactors has been directed towards a fast-spectrum MSR, e.g., the Molten Salt Fast Reactor proposed in the Euratom's EVOL (Evaluation and Viability of Liquid Fuel Fast Reactor System) project [10] and its continuing SAMOFAR project [31]. This innovative concept derives from ORNL's MSRE and MSBR (Molten Salt Breeder Reactor) along with extensive parametric studies, including various core arrangements, reprocessing performances, investigation of different salt compositions, etc. Compared to the old MSRs developed at ORNL, the MSFR removes the graphite moderator from the core and operates in a thorium fuel cycle, resulting in a breeder reactor with a fast neutron spectrum.

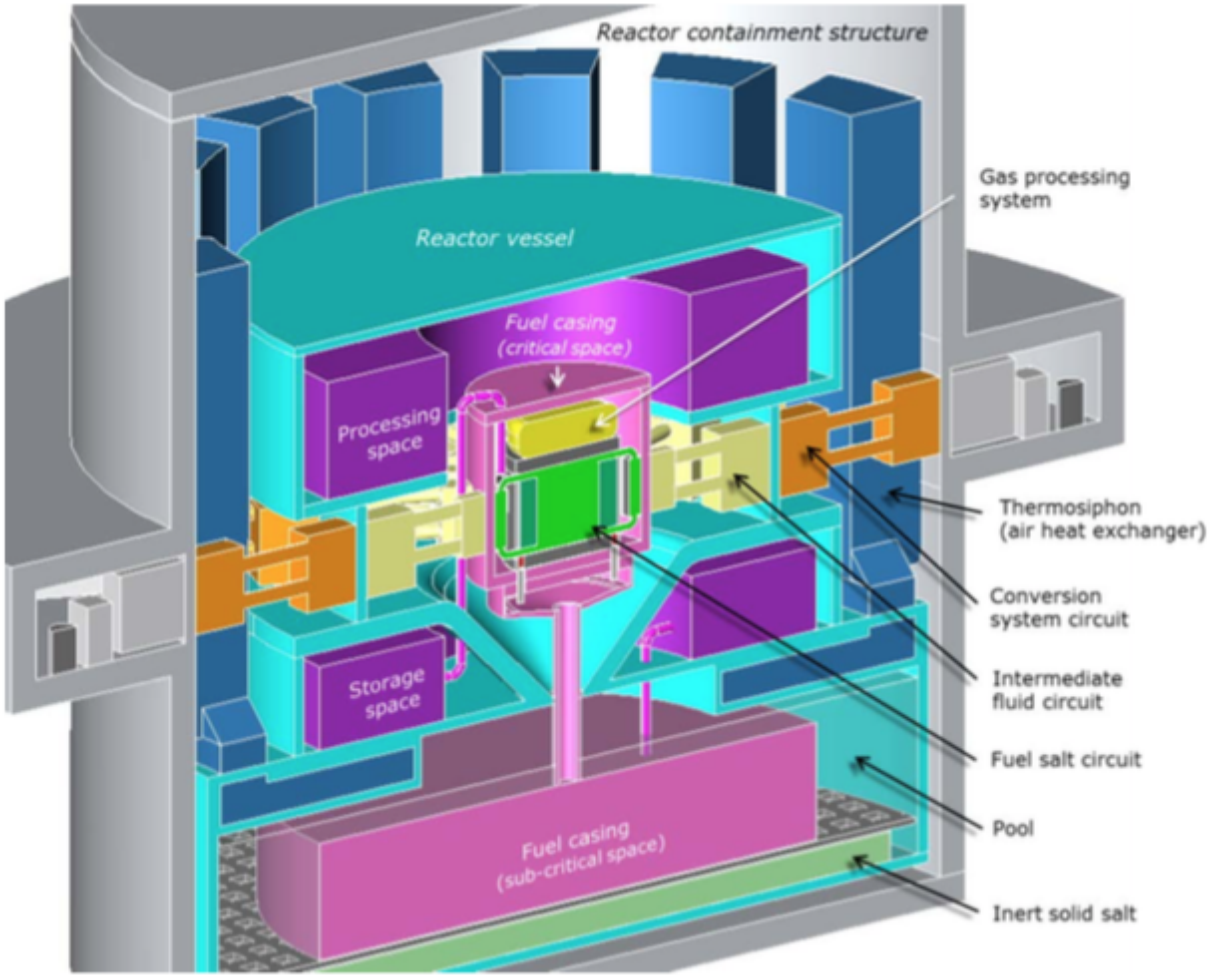

Figure 1.14: Layout of MSFR system [23].

The conceptual design of the MSFR system is illustrated in Figure 1.14. There are three different circuits in the MSFR: the fuel salt circuit (primary circuit), the intermediate fluid circuit and the conversion system circuit. They are confined by three physical barriers:

- Fuel casing (pink): the wall between fuel salt and intermediate salt.
- Reactor vessel (light blue): the wall between intermediate salt and conversion fluid.
- Reactor containment structure (grey): the wall insulating conversion fluid from atmosphere in a closed conversion loop.

The fuel salt composition is a molten binary fluoride salt, which is composed of 77.5 mol% lithium fluoride (^7Li enriched to 99.995 mol%) and 22.5 mol% heavy nuclei (HN) fluoride.

This salt composition leads to a fast neutron spectrum in the core. The total volume of fuel salt in the primary circuit is 18 m^3 (half in the core and half out of the core), and the total circulating time is about 4 s at a volumetric flow rate of 4.5 m^3/s.

As illustrated in Figure 1.15, the fission reactions take place within the fuel salt circuit, which includes the core cavity, the inlet and outlet pipes, the liquid-gas separation and sampling systems, the pumps, the fuel heat exchangers and the bubble injection systems. At the design power of 3 GWth the fuel salt enters the core cavity from the bottom at 923 K, flows upward through the active core, and leaves the core cavity from the top at 1023 K. Afterwards, it is fed into 16 external modules (each one contains a fuel pump, a fuel heat exchanger and a bubbling system) located around the core. Finally the fuel salt is returned to the core.

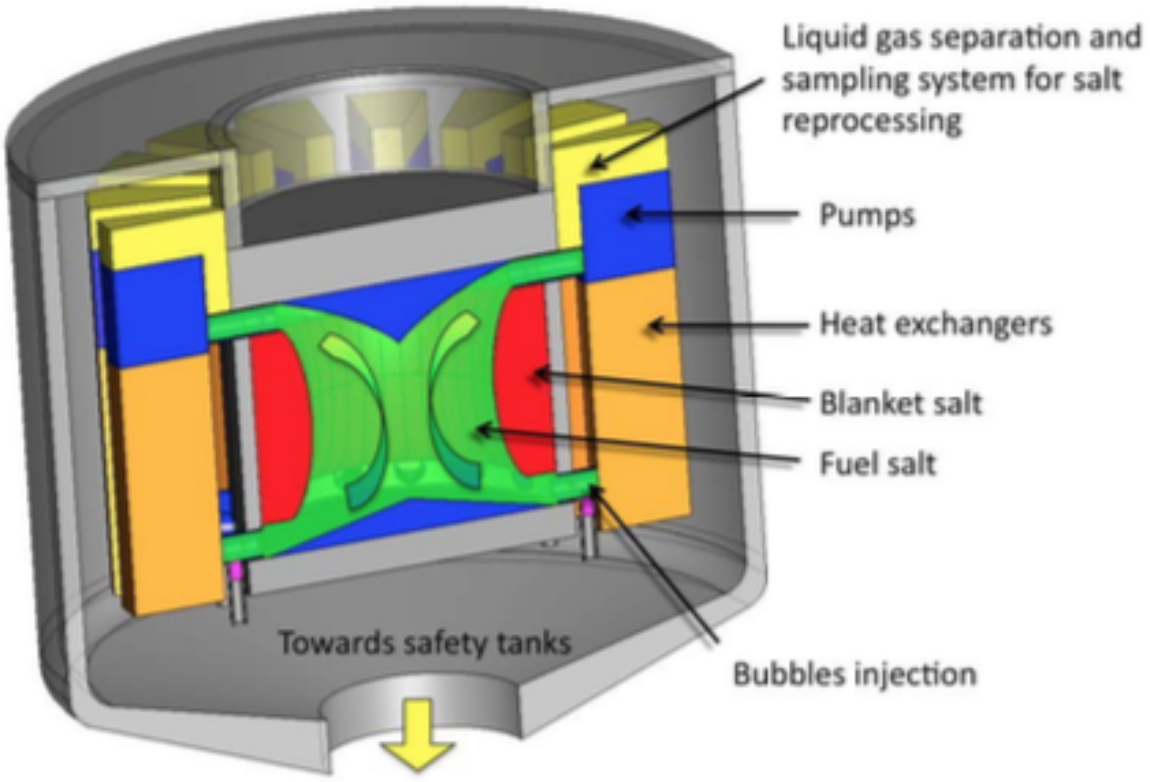

Figure 1.15: MSFR fuel circuit [23].

The shape of the MSFR core is a cylinder with a radius of 112.75 cm and a height of 225.5 cm. The external core structures and the fuel heat exchangers are protected by thick reflectors, which are made of nickel-based alloys. They are designed to stop more than 99% of the escaping neutrons. The radial reflector includes a 50 cm thick fertile blanket ($77.5LiF - 22.5ThF_4$) to increase the breeding ratio. This blanket is surrounded by a 20

cm thick layer of boron carbide (B_4C), which provides an additional protection from the remaining neutrons.

1.6 Thesis Scope and Outline

The main objective of my Ph.D. work is to continue the development of the multi-physics tool GeN-Foam, as well as to build high-fidelity MSR models which are able to analyze phenomena peculiar to liquid-fueled MSRs. Since commercialized MSR has not been built yet, GeN-Foam will allow us to study and better understand the significance and impact of these phenomena on the performance and safety of MSRs. Also, a higher fidelity tool can provide benchmark data for a lower fidelity tool. For example, in this project, our research partner Texas A&M University is doing the code development of reduced-order modeling for MSRs, which is a lower fidelity tool with a less computational demanding. We can provide our MSR models and simulation results for their code verification and validation. Therefore, it is necessary and very beneficial to develop such a high-fidelity tool for MSRs.

Chapter 2 provides an overview of the multi-physics code GeN-Foam and its calculation methodologies. New functionalities of solving adjoint multi-group diffusion eigenvalue problems and calculating effective delayed neutron fractions have been implemented in GeN-Foam and will be discussed. Additionally, the methods of evaluating the impacts of fuel salt compressibility and radiative heat transfer in MSRs will be presented.

Chapter 3 describes the simulation models for two different types of MSRs, i.e., the Molten Salt Reactor Experiment and the Molten Salt Fast Reactor. The MSRE model is mainly used for studying the delayed neutron precursor drift in MSRs, and the MSFR model is used for studying the effects of fuel salt compressibility and radiative heat transfer in MSRs.

The calculation results are summarized in Chapters 4, 5 and 6. Chapter 4 includes the results of multiplication factor and effective delayed neutron fraction under the static and flow circulating conditions in the MSRE, compared them with ORNL's reports. Also, three simple transient analyses have been performed to demonstrate the transient modeling capability of GeN-Foam. Chapter 5 evaluates the fuel salt compressibility effect in the MSFR using two different salts, molten fluoride salt and molten chloride salt. Chapter 6 describes the impact of radiation on the heat transfer mechanism in the MSFR.

Finally, Chapter 7 draws a conclusion and lists future work and possible improvements on the MSR study.

Chapter 2

Methodologies

2.1 GeN-Foam Code Review

GeN-Foam (Generalized Nuclear Foam) is a multi-physics solver for nuclear reactor analysis based on an open-source C++ toolbox OpenFOAM [35], and it was originally developed at the Paul Scherrer Institut (PSI) and École Polytechnique Fédérale de Lausanne (EPFL) in Switzerland. Today GeN-Foam is still under an active development with contributions from universities or institutes worldwide, including UC-Berkeley. In essence, this code system is an unusually complex OpenFOAM solver for advanced users who have a good knowledge of C++ programming language [34] and OpenFOAM and a solid background in multi-physics nuclear applications, with particular regard to computational fluid dynamics (CFD). GeN-Foam consists of 4 sub-solvers: a neutronics sub-solver, a thermal-hydraulics sub-solver, a thermal-mechanics sub-solver, and a sub-scale fuel sub-solver. The methodologies applied in each sub-solver, as well as their coupling strategy, will be explained in the following subsections. A more detailed description of GeN-Foam code can be found in Fiorina's paper [11] and [12].

Neutronics sub-solver

The neutronics sub-solver solves multi-group diffusion Equation (2.1) and delayed neutron precursor (DNP) concentration Equation (2.2), including a precursor transport term based on the velocity field $\boldsymbol{u}$ for the analysis of DNP drift in a liquid-fueled reactor (e.g., molten salt reactors):

$$\frac{1}{v_i}\frac{\partial \phi_i}{\partial t} = \nabla \cdot D_i \nabla \phi_i + \frac{(1-\beta)\chi_{p,i}}{k_{eff}} \sum_{i'=1}^{I} \nu_{i'} \Sigma_{f,i'} \phi_{i'} - \Sigma_{r,i}\phi_i + \chi_{d,i} \sum_{k=1}^{K} \lambda_k C_k + \sum_{i' \neq i} \Sigma_{s,i' \rightarrow i} \phi_{i'} \quad (2.1)$$

$$\frac{\partial C_k}{\partial t} + \nabla \cdot (\boldsymbol{u_D} C_k) = \frac{\beta_k \sum_{i=1}^{I} \nu_i \Sigma_{f,i} \phi_i}{k_{eff}} - \lambda_k C_k \quad (2.2)$$

where

$$v_i = \text{average neutron velocity for the } i^{th} \text{ energy group},$$

$$\phi_i = \text{neutron flux for the } i^{th} \text{ energy group},$$

$$\phi_{i'} = \text{neutron flux for the } i'^{th} \text{ energy group},$$

$$t = \text{time},$$

$$D_i = \text{neutron diffusion coefficient for the } i^{th} \text{ energy group},$$

$$\beta = \text{total delayed neutron fraction},$$

$$\beta_k = \text{delayed neutron fraction for the } k^{th} \text{ DNP group},$$

$$\chi_{p,i} = \text{prompt neutron yield for the } i^{th} \text{ energy group},$$

$$k_{eff} = \text{effective multiplication factor},$$

$$\nu_i = \text{number of neutrons produced per fission for the } i^{th} \text{ energy group},$$

$$\nu_{i'} = \text{number of neutrons produced per fission for the } i'^{th} \text{ energy group},$$

$$\Sigma_{f,i} = \text{macroscopic fission cross section for the } i^{th} \text{ energy group},$$

$$\Sigma_{f,i'} = \text{macroscopic fission cross section for the } i'^{th} \text{ energy group},$$

$$\Sigma_{r,i} = \text{macroscopic removal cross section for the } i^{th} \text{ energy group},$$

$$\chi_{d,i} = \text{delayed neutron yield for the } i^{th} \text{ energy group},$$

$$\lambda_k = \text{decay constant for the } k^{th} \text{ DNP group},$$

$$C_k = \text{concentration of the } k^{th} \text{ DNP group},$$

$$\Sigma_{s,i'\rightarrow i} = \text{macroscopic group-transfer cross section from the } i'^{th} \text{ to the } i^{th} \text{ energy group},$$

$$\text{and } \boldsymbol{u_D} = \text{Darcy fluid velocity}.$$

The number and structure of both neutron energy and DNP group are based on user's selection. The group constants (e.g., reaction cross section, neutron velocity, diffusion coefficient, average number of neutrons produced per fission, total delayed neutron fraction, prompt/delayed neutron yield, and DNP's decay constant) are generated by the Monte Carlo code Serpent 2 [21], and an Octave [9] script has been written to convert them to GeN-Foam readable inputs. For the cross section parametrization in GeN-Foam, eight different perturbed states can be fed to the solver: (1) nominal condition; (2) increased/decreased fuel temperature; (3) increased/decreased coolant density; (4) increased/decreased coolant temperature; (5) axially expanded fuel; (6) radially expanded core; (7) expanded cladding; and (8) increased/decreased boron concentration. Linear interpolation between the nominal state and perturbed states is applied except the fuel temperature, for which the process can be based either on the logarithm or the square root of temperature, depending on fast or thermal neutron spectrum, respectively.

In addition to the standard built-in boundary conditions in OpenFoam, a new boundary condition, which is used to simulate albedo boundary conditions, has been implemented in the GeN-Foam neutronics sub-solver as:

$$\frac{D_i}{\phi_i}\nabla\phi_i = -\frac{1}{2}(\frac{1-\alpha_a}{1+\alpha_a}) \tag{2.3}$$

where the albedo coefficient, α_a, depends on the properties of the medium external to the boundary, and it can be estimated by Equation (2.4):

$$\alpha_a = -\frac{1-2D_i/L_i}{1+2D_i/L_i} \tag{2.4}$$

where L_i is the diffusion length for the i^{th} energy group. If the outside of boundaries is vacuum without any incoming current, the albedo coefficient is just 0.

Thermal-hydraulics sub-solver

The thermal-hydraulics sub-solver has been developed based on the standard $k-\varepsilon$ turbulent model for compressible or incompressible flows but extended to coarse-mesh applications through the use of a porous medium approach for user-selected cell zones inside the mesh. In other words, fine meshes can be applied for simple structures (e.g., plenum region), and coarse meshes can be applied for complex structures (e.g., core region and heat exchanger) by treating them as porous media. The equations for the turbulent single-phase flow of a fluid in a porous medium can be derived from the standard Navier-Stokes (NS) equations, which govern the motion of fluids and can be seen as Newton's second law of motion for fluids, via time and volume averages. Equations (2.5), (2.6) and (2.7), representing mass, momentum and energy conservation, respectively, have been implemented in GeN-Foam:

$$\frac{\partial\gamma\rho}{\partial t} + \nabla\cdot(\rho\boldsymbol{u_D}) = 0 \tag{2.5}$$

$$\frac{\partial\rho\boldsymbol{u_D}}{\partial t} + \frac{1}{\gamma}\nabla\cdot(\rho\boldsymbol{u_D}\otimes\boldsymbol{u_D}) = \nabla\cdot(\mu_T\nabla\boldsymbol{u_D}) - \gamma\nabla p + \gamma\boldsymbol{F_g} + \gamma\boldsymbol{F_{ss}} - (\rho\boldsymbol{u_D}\otimes\boldsymbol{u_D})\nabla\frac{1}{\gamma} \tag{2.6}$$

$$\frac{\partial\gamma\rho e}{\partial t} + \nabla\cdot(\boldsymbol{u_D}(\rho e+p)) = \gamma\nabla\cdot(k_T\nabla T) + \boldsymbol{F_{ss}}\cdot\boldsymbol{u_D} + \gamma\dot{Q}_{ss} + (k_T\nabla T)\cdot\nabla\gamma \tag{2.7}$$

where

γ = porosity or void fraction,

ρ = density,

t = time,

$\boldsymbol{u_D}$ = Darcy fluid velocity,

μ_T = turbulent dynamic viscosity,

p = pressure,

$\boldsymbol{F_g}$ = volumetric force due to gravity,

$\boldsymbol{F_{ss}}$ = volumetric force due to the interaction with the sub-scale structure,

e = fluid total energy,

k_T = turbulent conductivity,

T = temperature,

and $\dot{Q}_{ss}$ = heat transferred from the sub-scale structure to the fluid.

The drag force, $\boldsymbol{F_{ss}}$, is proportional to the fluid's velocity and can be obtained as follows:

$$\boldsymbol{F_{ss}} = \boldsymbol{\kappa}(\boldsymbol{u_D}) \cdot \boldsymbol{u_D} \tag{2.8}$$

where the tensor, $\boldsymbol{\kappa(u_D)}$, can be obtained from experiments or by Equation (2.9):

$$\kappa(u_D)_{ii} = \frac{f_{D,i}\rho u_{D,i}}{2D_h\gamma^2} \tag{2.9}$$

where

$\kappa(u_D)_{ii}$ = component of $\boldsymbol{\kappa(u_D)}$ in the i^{th} principal direction of the sub-scale structure,

$f_{D,i}$ = Darcy friction factor in the i^{th} principal direction of the sub-scale structure,

ρ = density,

$u_{D,i}$ = Darcy fluid velocity in the i^{th} principal direction of the sub-scale structure,

D_h = hydraulic diameter of the sub-scale structure,

and γ = porosity or void fraction.

The Darcy friction factor, f_D, is assumed to have the correlation of the form:

$$f_{D,i} = A_{f_{D,i}} Re^{B_{f_{D,i}}} \tag{2.10}$$

where the Reynolds number, Re, is calculated using the velocity and hydraulic diameter, and the constants, $A_{f_{D,i}}$ and $B_{f_{D,i}}$, are user selected.

The heat source, $\dot{Q}_{ss}$, can be calculated as follows:

$$\dot{Q}_{ss} = A_V h(T_{ss} - T) \tag{2.11}$$

where

A_V = volumetric area between the fluid and the sub-scale structure,

h = heat transfer coefficient between the fluid and the sub-scale structure,

T = temperature of the fluid,

and T_{ss} = temperature of the sub-scale structure.

The temperature of the sub-scale structure, T_{ss}, is calculated by Equation (2.12):

$$\rho_{ss} c_{p,ss} \frac{\partial T_{ss}}{\partial t} = \nabla \cdot (\gamma k_{ss} \nabla T) + A_V h (T - T_{ss}) \tag{2.12}$$

where

ρ_{ss} = density of the sub-scale structure,

$c_{p,ss}$ = specific heat capacity of the sub-scale structure,

T = temperature of the fluid,

T_{ss} = temperature of the sub-scale structure,

t = time,

γ = porosity or void fraction,

k_{ss} = conductivity of the sub-scale structure,

A_V = volumetric area between the fluid and the sub-scale structure,

and h = heat transfer coefficient between the fluid and the sub-scale structure.

The heat transfer coefficient between the fluid and the sub-scale structure, h, and the Nusselt number in the i^{th} principal direction of the sub-scale structure, Nu_i, are calculated by Equations (2.13) and (2.14), respectively:

$$h = \sum_i \frac{h_i u_{D,i}}{|\boldsymbol{u_D}|} \tag{2.13}$$

$$Nu_i = A_{Nu,i} Re^{B_{Nu,i}} Pr^{C_{Nu,i}} + D_{Nu,i} \tag{2.14}$$

where

h_i = heat transfer coefficient in the i^{th} principal direction of the sub-scale structure,

$u_{D,i}$ = Darcy fluid velocity in the i^{th} principal direction of the sub-scale structure,

$\boldsymbol{u_D}$ = Darcy fluid velocity,

Re = Reynolds number,

Pr = Prandtl number,

$A_{Nu,i}, B_{Nu,i}, C_{Nu,i}$ and $D_{Nu,i}$ = user-selected constants.

In addition, it is possible to simplify the modeling of a heat exchanger by providing a user-selected external heat transfer coefficient, h_{ext}, and a fixed external fluid temperature, T_{ext}:

$$\dot{Q}_{ss} = h_{eff} A_V (T_{ext} - T) = \frac{1}{1/h + 1/h_{ext}} A_V (T_{ext} - T) \tag{2.15}$$

Besides, in case of a clear fluid, by setting the porosity to 1 and the sub-scale structure's effect to 0, the equations employed in the thermal-hydraulics sub-solver are converted back to the traditional Reynolds-averaged Navier-Stokes (RANS) equations. Therefore, the same set of equations can be discretized and solved on the same mesh while treating different zones of geometry with two different approaches (detailed RANS for a clear fluid zone or a coarse mesh porous medium for a complex structure zone).

Thermal-mechanics sub-solver

The thermal-mechanics sub-solver is constructed based on the already available solver "solidDisplacementFoam" in OpenFOAM. It is used to evaluate the temperature-induced deformation of the main structures, e.g., reactor vessel, strongback, diagrid, etc. In the active core region, the axial deformation of the neutronics mesh is calculated independently, based on the fuel (in case of open gap) or cladding (in case of closed gap) expansion coefficients and temperatures, as shown in Equation (2.16):

$$\boldsymbol{v_f} \cdot \nabla D_f = \alpha_{f/c} (T_{f/c} - T_{f/c,ref}) \tag{2.16}$$

where

$\boldsymbol{v_f}$ = user-selected axial orientation of fuel,

D_f = fuel displacement field,

$\alpha_{f/c}$ = linear expansion coefficient of fuel or cladding,

$T_{f/c}$ = temperature in fuel or cladding,

and $T_{f/c,ref}$ = reference temperature in fuel or cladding.

Sub-scale fuel sub-solver

The sub-scale fuel sub-solver is used to accurately calculate the temperature distribution in the solid fuel and the cladding. It is assumed that the geometry of the fuel is axial-symmetric and the axial heat conduction is neglected. Instead of solving Equation (2.12), the 1-D heat conduction Equations (2.17) and (2.18) are solved for the fuel pellet and cladding, respectively.

$$\rho_f c_{p,f} \frac{\partial T_f}{\partial t} = k_f \frac{\partial^2 T_f}{\partial r^2} + k_f \frac{1}{r} \frac{\partial T_f}{\partial r} + \dot{Q}_f \tag{2.17}$$

$$\rho_c c_{p,c} \frac{\partial T_c}{\partial t} = k_c \frac{\partial^2 T_c}{\partial r^2} + k_c \frac{1}{r} \frac{\partial T_c}{\partial r} \tag{2.18}$$

where

$$\rho_f = \text{density of fuel},$$

$$\rho_c = \text{density of cladding},$$

$$c_{p,f} = \text{specific heat capacity of fuel},$$

$$c_{p,c} = \text{specific heat capacity of cladding},$$

$$T_f = \text{temperature of fuel},$$

$$T_c = \text{temperature of cladding},$$

$$t = \text{time},$$

$$k_f = \text{conductivity of fuel},$$

$$k_c = \text{conductivity of cladding},$$

$$r = \text{radial distance},$$

$$\text{and } \dot{Q}_f = \text{heat source in fuel}.$$

Coupling strategy

The multi-physics solver GeN-Foam uses three different meshes, corresponding to thermal-hydraulics, thermal-mechanics and neutron diffusion. The additional sub-scale fuel model is solved in each mesh cell within the fuel zone of the thermal-hydraulics mesh. It is possible to have different refinements on different meshes, and consistent mapping between three meshes is performed at each time step using a standard OpenFOAM cell-volume-weighted algorithm. The coupling strategy between four sub-solvers in GeN-Foam is depicted in Figure 2.1.

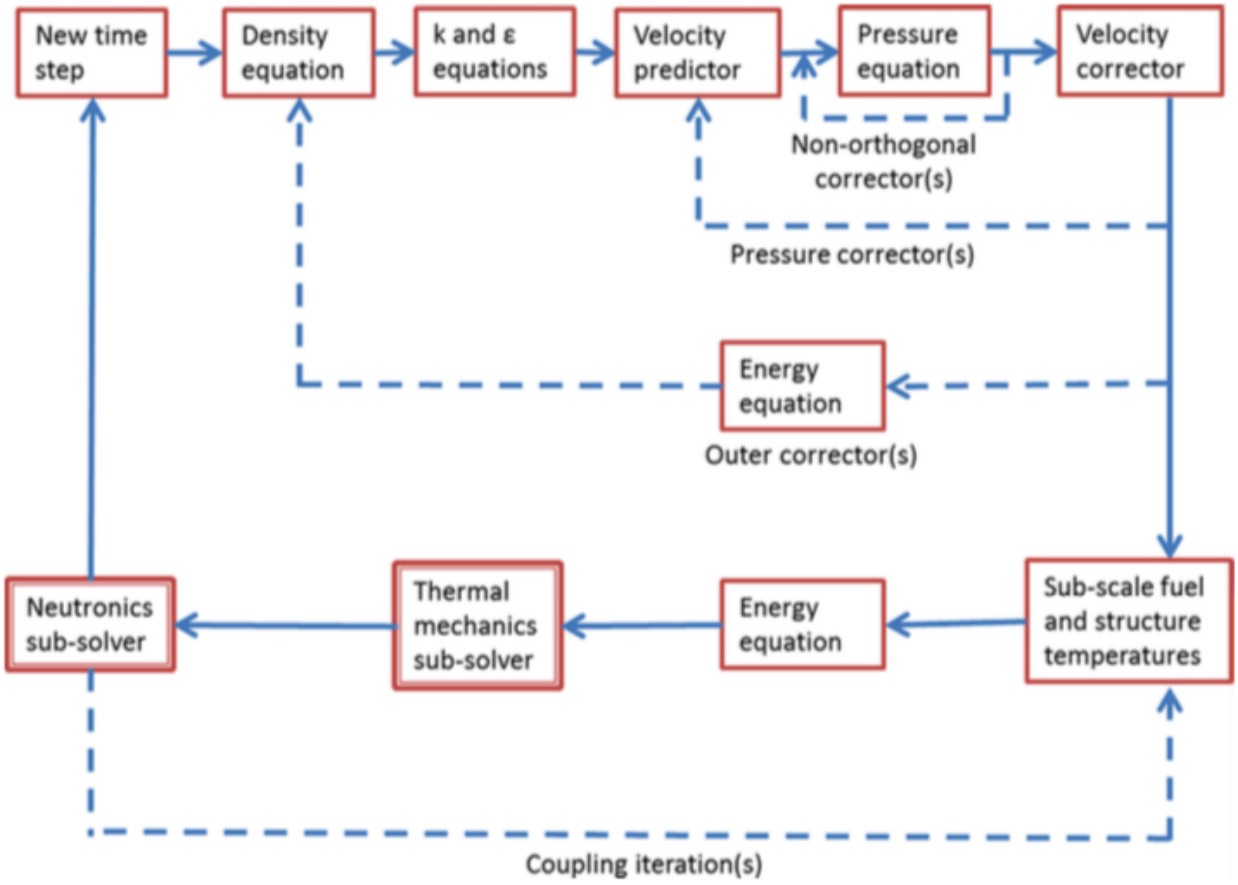

Figure 2.1: Coupling strategy in GeN-Foam [12].

An initial time step is first selected by the user, and then GeN-Foam follows the structure of the PIMPLE algorithm [17], which is a combination of PISO (Pressure Implicit with Splitting of Operator) and SIMPLE (Semi-Implicit Method for Pressure-Linked Equations), for solving velocity, pressure and energy. After obtaining the coolant flow and temperature fields, GeN-Foam solves the temperature in the sub-scale structures, fuel and cladding (Equations (2.12), (2.17) and (2.18)), and again for the energy Equation (2.7). The thermal-mechanics and neutronics sub-solvers are used subsequently. Initial residuals are evaluated before solving each equation, and the iteration continues until all residuals are lower than the desired tolerance. Afterwards, GeN-Foam will move to the next time step. Note that it is possible to solve the selected equations of interest and leave others untouched. In this Ph.D. project for the liquid-fueled MSR study, the thermal-mechanics sub-solver and the sub-scale fuel sub-solver have never been used.

2.2 Effective Delayed Neutron Fraction Calculation

Although the fraction of delayed neutrons in a fission reaction is very small, delayed neutrons are significantly important for the safe control of any nuclear reactors. In liquid-fueled MSRs, the effective delayed neutron fraction differs from the delayed neutron fraction. In order to calculate the effective delayed neutron fraction, the solutions of both forward and adjoint multi-group diffusion eigenvalue problems are needed. Since the old version of GeN-Foam only solved the forward neutron flux, a function of computing the adjoint neutron flux, according to Aufiero's paper [1], has been implemented. Equations (2.19) and (2.20) used to calculate the adjoint eigenvalue functions are given:

$$\nabla \cdot D_i \nabla \phi_i^* - \Sigma_{r,i}\phi_i^* + \sum_{i' \neq i} \Sigma_{s,i\to i'}\phi_{i'}^* + \frac{1-\beta}{k_{eff}}\nu_i\Sigma_{f,i}\sum_{i'=1}^{I}\chi_{p,i'}\phi_{i'}^* + \frac{1}{k_{eff}}\nu_i\Sigma_{f,i}\sum_{k=1}^{K}\beta_k C_k^* = 0 \quad (2.19)$$

$$-\nabla \cdot (-\boldsymbol{u_D} C_k^*) - \lambda_k C_k^* + \lambda_k \sum_{i=1}^{I}\chi_{d,i}\phi_i^* = 0 \quad (2.20)$$

where

D_i = neutron diffusion coefficient for the i^{th} energy group,

ϕ_i^* = Adjoint neutron flux for the i^{th} energy group,

$\phi_{i'}^*$ = Adjoint neutron flux for the i'^{th} energy group,

$\Sigma_{r,i}$ = macroscopic removal cross section for the i^{th} energy group,

$\Sigma_{s,i\to i'}$ = macroscopic group-transfer cross section from the i^{th} to the i'^{th} energy group,

β = total delayed neutron fraction,

k_{eff} = effective multiplication factor,

ν_i = number of neutrons produced per fission for the i^{th} energy group,

$\Sigma_{f,i}$ = macroscopic fission cross section for the i^{th} energy group,

$\chi_{p,i'}$ = prompt neutron yield for the i'^{th} energy group,

β_k = delayed neutron fraction for the k^{th} DNP group,

C_k^* = importance of the k^{th} DNP group,

$\boldsymbol{u_D}$ = Darcy fluid velocity,

λ_k = decay constant for the k^{th} DNP group,

and $\chi_{d,i}$ = delayed neutron yield for the i^{th} energy group.

Discretization of the equations is performed according to a finite-volume approach provided by OpenFOAM, which operates on unstructured meshes and optionally includes correctors for non-orthogonal meshes. In case of forward multi-group diffusion eigenvalue calculations, a traditional power iteration algorithm [33] is used to calculate the forward neutron flux. In case of adjoint multi-group diffusion eigenvalue calculations, exactly same algorithm is applied here to calculate the adjoint neutron flux. After obtaining the forward and adjoint neutron flux distribution, the effective delayed neutron fraction for the k^{th} DNP group, $\beta_{eff,k}$, and the total effective delayed neutron fraction, β_{eff}, can be calculated as follows in Equations (2.21) and (2.22), respectively:

$$\beta_{eff,k} = \frac{\int_{allspace} \lambda_k C_k \sum_{i=1}^{I} \chi_{d,i} \phi_i^*}{\int_{allspace} \sum_{i=1}^{I} \chi_{d,i} \phi_i^* \sum_{k'=1}^{K} \lambda_{k'} C_{k'} + \int_{allspace} \sum_{i=1}^{I} \chi_{p,i} \phi_i^* \sum_{i'=1}^{I} \nu_{i'} \Sigma_{f,i'} \phi_{i'}} \tag{2.21}$$

$$\beta_{eff} = \sum_{k=1}^{K} \beta_{eff,k} \tag{2.22}$$

2.3 Fuel Salt Compressibility Calculation

Even though all real fluids are compressible, liquid flows are almost always treated as incompressible due to their small compressibilities or insignificant change in density as pressure changes. In non-moderated, fast-spectrum MSRs the effect of thermal expansion of liquid fuel out of the core is critical, and an incompressible-fluid model leads to an overestimation of negative feedback under certain circumstances.

For example, during a power excursion in the MSFR, the increase of reactor power leads to a rapid rise in the in-core fuel salt temperature, which affects the neutron balance in two different ways. The Doppler effect increases the neutron absorption term, and the thermal expansion of the fuel salt out of the core increases the neutron leakage. Both phenomena reduce the system reactivity, but unlike the Doppler effect that happens immediately, the salt expansion is a delayed response after the energy deposition in fuel, as the density perturbation and the pressure waves take a finite time to propagate through the reactor core. However, an incompressible approximation implies that the salt density is instantaneously related to the fluid temperature, as if the speed of sound in the fluid is infinite. Therefore, an incompressible-fluid model is not suitable to accurately study MSRs transients, and it is necessary to develop a compressible-fluid model for high-fidelity simulations. The velocity of pressure wave propagation is related to the speed of sound, c, which can be estimated by Equation (2.23) if the bulk modulus, K, or the isentropic compressibility, β_S, is known [27]:

$$c = \sqrt{\frac{K}{\rho}} = \frac{1}{\sqrt{\beta_S \rho}} \tag{2.23}$$

where the density, ρ, is related to both temperature and pressure, and it is assumed to be linearized around a reference condition as shown in Equation (2.24):

$$\rho = \rho_0 - \rho_0 \alpha (T - T_0) + \rho_0 \beta_T (p - p_0) \tag{2.24}$$

where

$$\rho_0 = \text{reference density},$$

$$\alpha = \text{thermal expansion coefficient},$$

$$T = \text{temperature},$$

$$T_0 = \text{reference temperature},$$

$$\beta_T = \text{isothermal compressibility},$$

$$p = \text{pressure},$$

$$\text{and } p_0 = \text{reference pressure}.$$

This equation of state has been implemented in the OpenFOAM library and can be used by the GeN-Foam thermal-hydraulics sub-solver to take into account the salt compressibility effect. The isothermal compressibility, β_T, can be evaluated by Equation (2.25):

$$\beta_T = \beta_S + \frac{\alpha^2 T}{\rho_0 c_p} = \frac{1}{K} + \frac{\alpha^2 T}{\rho_0 c_p} \tag{2.25}$$

When there are gas bubbles present in the salt, the effective compressibility of the mixture increases and the speed of sound in that medium decreases. Then the speed of sound in the mixture, c_{mix}, can be approximated by Wood's Equation (2.26)[36]:

$$c_{mix} = \sqrt{\frac{K_{salt} \cdot K_{gas}}{(K_{salt} \cdot \gamma + K_{gas}(1-\gamma)) \cdot (\rho_{salt}(1-\gamma) + \rho_{gas} \cdot \gamma)}} \tag{2.26}$$

where

$$K_{salt} = \text{bulk modulus of salt},$$

$$K_{gas} = \text{bulk modulus of the gas bubble},$$

$$\gamma = \text{void or gas volume fraction in the mixture},$$

$$\rho_{salt} = \text{density of salt},$$

$$\text{and } \rho_0 = \text{density of the gas bubble}.$$

2.4 Radiative Heat Transfer Calculation

Radiative heat transfer is not usually considered in the design of nuclear reactors, partly due to the lack of data and partly due to lower operation temperatures. However, MSRs have much higher operation temperatures (above 900 K) because of the characteristics of molten salts. At high temperatures, RHT begins to play a more important role as it enhances the heat transfer rate. Therefore, it is necessary to investigate RHT effects in MSRs.

In OpenFOAM applications, some RHT solvers have been developed and available for public use. They can be easily implemented in GeN-Foam to calculate the radiation transport. First, the header file, "radiationModel.H", is included in GeN-Foam for code compilation. Then the thermal-hydraulics sub-solver is modified by adding a radiation source term, $rad.Sh(thermo, he)$, to the energy Equation (2.7). This source term consists of two member functions, $Ru()$ and $Rp()$, which represent a constant source term component and a source term component for the power of T^4, respectively:

$$Sh() = Ru() - Rp() \cdot T^4 \tag{2.27}$$

These two source term components are defined differently in different radiation models, e.g., no radiation model (noRadiation), P1 model (P1), finite volume discrete ordinates model (fvDOM), view factor model (viewFactor), etc. In this project, the "noRadiation" model and the "P1" model are used and explained in the following paragraphs.

The "noRadiation" model disables the RHT calculation by setting the member functions $Ru()$ and $Rp()$ to 0, so $Sh()$ becomes 0 and the original energy equation is not affected by radiation.

The "P1" model is the simplest case of the more general "P-N" model based on the first order spherical harmonic expansion of radiation intensity. This method is very popular because it reduces the equation of radiative transfer from a very complicated integral equation to a relatively simple partial differential equation. A detailed mathematical derivation of the P1-approximation for RHT can be found in Modest's book [24]. The "P1" model is powerful and capable of modeling anisotropic scattering in absorbing, emitting and scattering media. It provides advantages of simplicity, high computational efficiency and relatively good accuracy, if the optical thickness is not too small. In "P1" model, member function $Ru()$ and $Rp()$ are calculated as:

$$Ru() = aG - E \tag{2.28}$$

$$Rp() = 4e\sigma_{SB} \tag{2.29}$$

where

$$a = \text{absorption coefficient},$$

$$G = \text{incident radiation},$$

$$E = \text{emission contribution},$$

$$e = \text{emission coefficient},$$

$$\text{and } \sigma_{SB} = \text{Stefan-Boltzmann Constant} = 5.67\text{E-}8 \text{ W m}^{-2} \text{K}^{-4}.$$

The incident radiation, G, is obtained by solving the transport Equation (2.30)

$$\nabla \cdot (D_{P1} \nabla G) - aG = -4e\sigma_{SB}T^4 - E \tag{2.30}$$

where the diffusion coefficient in the "P1" model, D_{P1}, is defined as:

$$D_{P1} = \frac{1}{3a + \sigma_{eff}} = \frac{1}{3a + \sigma(3 - C_{P1})} \tag{2.31}$$

where

$$a = \text{absorption coefficient},$$

$$\sigma_{eff} = \text{effective scattering coefficient},$$

$$\sigma = \text{scattering coefficient},$$

$$\text{and } C_{P1} = \text{linear-anisotropic phase function coefficient.}$$

The linear-anisotropic phase function coefficient, C_{P1}, has a value between -1 and 1. A negative value represents the backward scattering, a positive value represents the forward scattering, and 0 represents the isotropic scattering. By setting the scattering coefficient, σ, to 0, the scattering is neglected. Finally, in the "P1" model the radiation source term, $Sh()$, is calculated as:

$$Sh() = Ru() - Rp() \cdot T^4 = aG - E - 4e\sigma_{SB}T^4 \tag{2.32}$$

Besides, to allow for a simplified treatment of RHT in heat exchangers, a possibility is included in GeN-Foam to model the net radiation rate, $\dot{Q}_{rad}$, between the fluid in the primary loop and the external fluid at a fixed temperature by:

$$\dot{Q}_{rad} = \epsilon\sigma_{SB}(T_{ext}^4 - T^4)A_V \tag{2.33}$$

where

$$\epsilon = \text{emissivity coefficient},$$

$$\sigma_{SB} = \text{Stefan-Boltzmann Constant} = 5.67\text{E-}8\ \mathrm{W\,m^{-2}\,K^{-4}},$$

$$T = \text{temperature of the fluid in the primary loop},$$

$$T_{ext} = \text{fixed external fluid temperature},$$

$$\text{and } A_V = \text{volumetric area of the surface.}$$

Chapter 3

Molten Salt Reactor Models

3.1 Molten Salt Reactor Experiment Model

The Molten Salt Reactor Experiment, constructed and operated at ORNL, is a liquid-fueled, graphite-moderated MSR with a thermal neutron spectrum. It was selected and used as a reference model to evaluate the effect of delayed neutron precursor drift in MSRs. The MSRE Serpent model, developed in Serpent 2, was used to generate neutron group constants. The MSRE GeN-Foam model, developed in GeN-Foam, was used to perform multi-physics calculations.

MSRE Serpent model

According to the zero-power physics experiments on the MSRE [29] and Shen's PhD thesis [32], a neutronics model was built in Serpent 2 to generate group constants at a reference state of 911 K, an increased temperature of 1200 K, and a reduced salt density of -10%, adopting ENDF/B-VII.1 nuclear data library with Serpent default two neutron energy groups (Table 3.1) and six DNP groups (Table 3.2). The XZ-plane of MSRE Serpent model is given in Figure 3.1, and materials used are listed in Table 3.3.

Table 3.1: Neutron energy group's boundaries in MSRE model.

Neutron Energy Group	1	2
Upper Boundary, MeV	0.625E-6	Infinite

Table 3.2: DNP group decay constants at the reference state in MSRE model.

DNP Group	1	2	3	4	5	6
Decay Constant, s^{-1}	1.334E-2	3.274E-2	1.208E-1	3.028E-1	8.497E-1	2.854

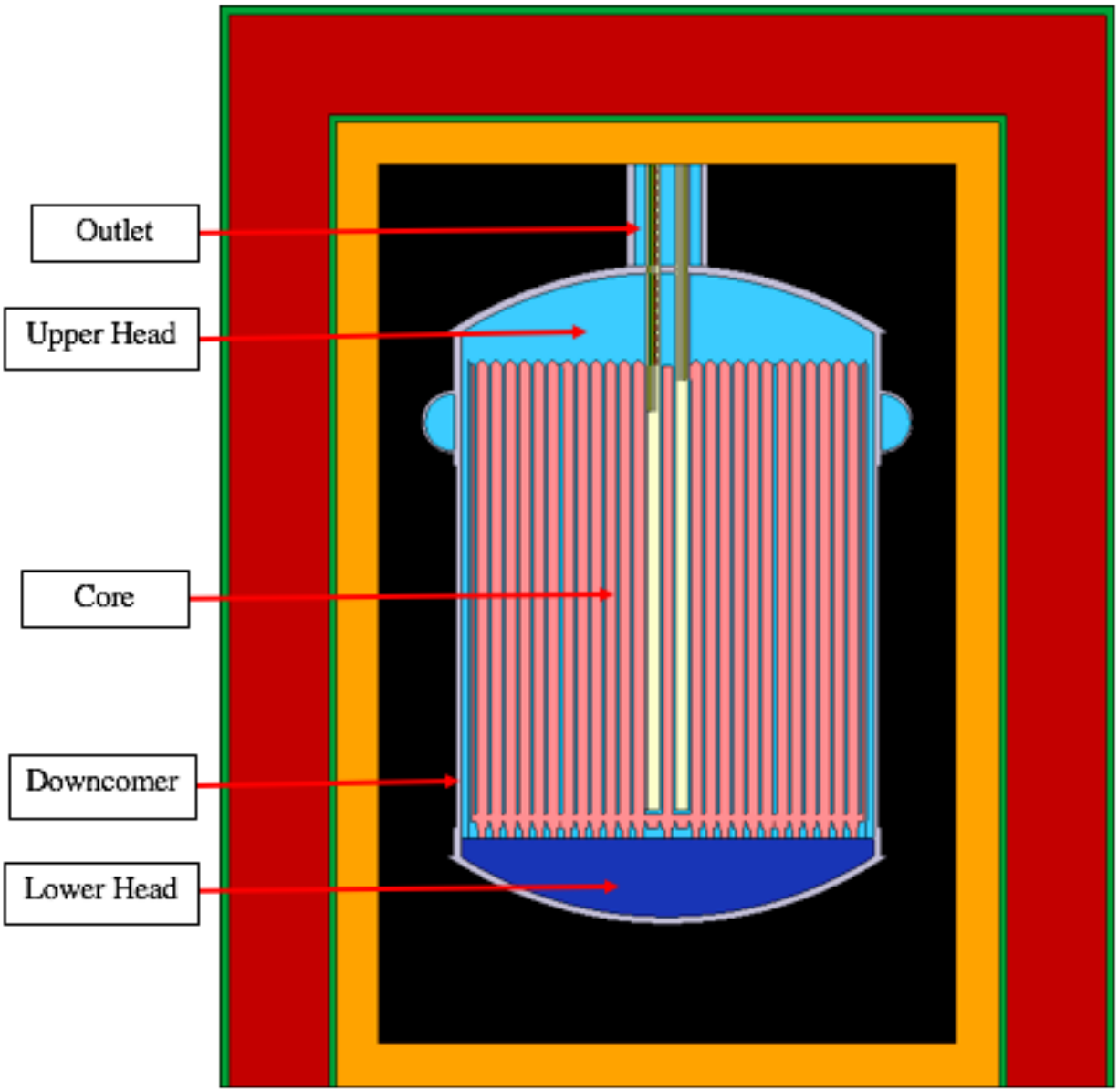

Figure 3.1: XZ-plane of MSRE Serpent model.

Table 3.3: Material information at 911 K in MSRE Serpent model.

Material	Composition	Density, $\mathrm{kg\,m^{-3}}$
Fuel Salt	$LiF - BeF_2 - ZrF_4 - UF_4$ (65-29.2-5-0.8 mol%)	2327.5
Coolant Salt	$LiF - BeF_2 - ZrF_4$ (65-30-5 mol%)	2327.5
Moderator	Graphite	1868.5
Salt Container	INOR-8	8774.7
Cover Gas	Helium	0.1786

The group constants generated by Serpent 2 were then imported into GeN-Foam by an Octave script. Their corresponding zones in the GeN-Foam model are summarized in Table 3.4.

Table 3.4: Group constant regions in MSRE Serpent and GeN-Foam models.

Regions in Serpent Model	Corresponding Regions in GeN-Foam Model
Lower Head	Lower Plenum
Core	Core
Upper Head	Upper Plenum
Outlet	Outlet, Pipe1, Fuel Pump, Pipe2, Heat Exchanger, Pipe3
Downcomer	Downcomer, Inlet

MSRE GeN-Foam model

A two-dimensional MSRE model was built in GeN-Foam, and its meshes, as shown in Figure 3.2, were generated by Gmsh tool [14]. This model is divided into 11 regions, and the geometrical size of the lower plenum, the core, the upper plenum and the downcomer are consistent with the MSRE design. However, it is difficult to model the external loop components (e.g., fuel pump, heat exchanger, etc.) in a 2D-RZ coordinate. Hence, the external loop's geometry is artificial and determined based on the the fuel salt volume from the ORNL-TM-728 report [30].

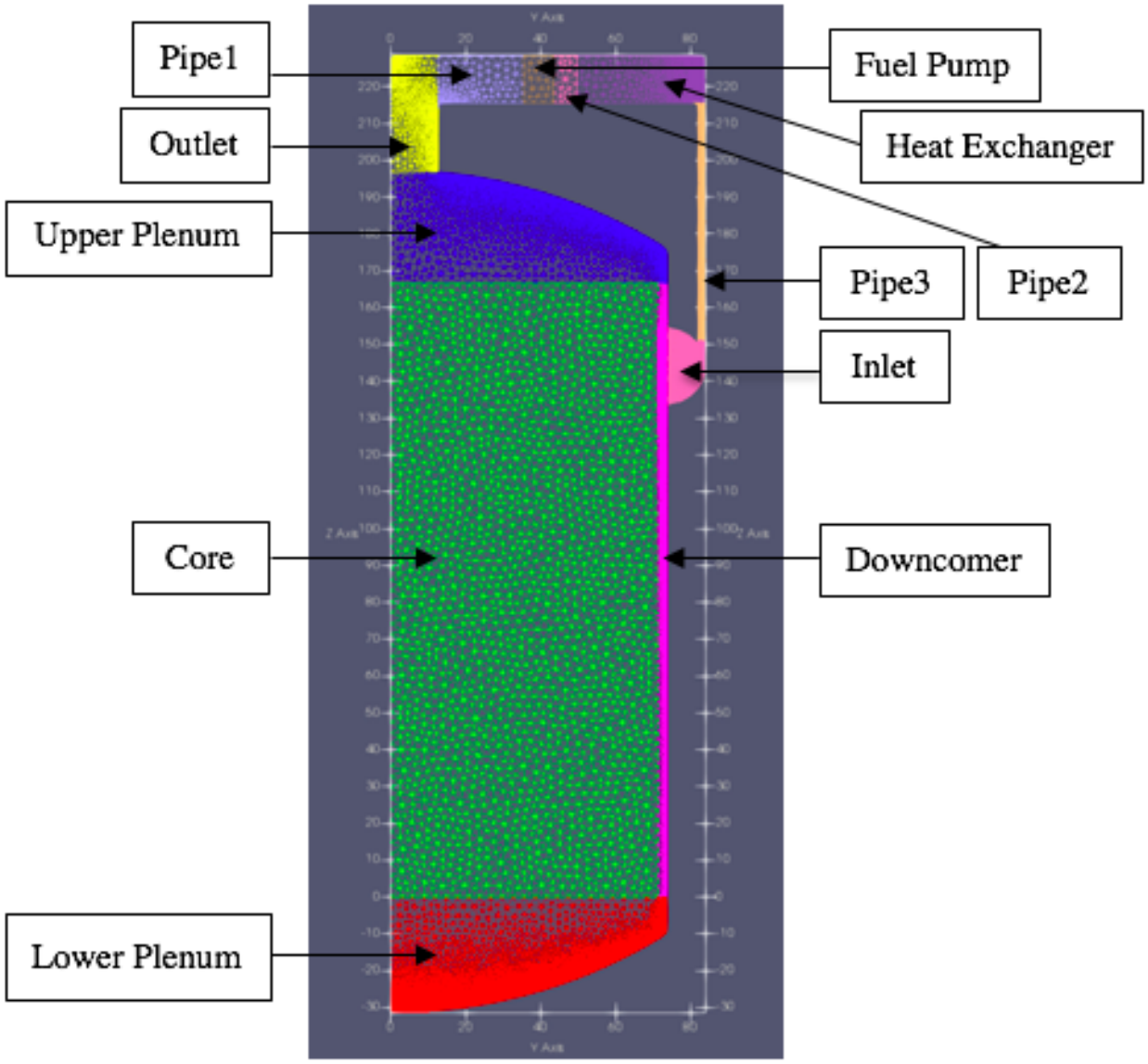

Figure 3.2: MSRE mesh in GeN-Foam.

In order to match the fuel salt volume in GeN-Foam model with the MSRE design, the void (salt) fraction was adjusted. By conserving the fuel salt volume, the residence time can also be matched with the MSRE design as long as the volumetric flow rate is same. The total fuel salt volume in the main stream is 67.3 ft^3 (1.905 m^3), and the volume in each region is listed in Table 3.5.

Table 3.5: Fuel salt volume in MSRE.

Region	GeN-Foam Model		MSRE Report [30]
	Void Fraction (γ)	Fuel Salt Volume, m^3	Fuel Salt Volume, m^3
Lower Plenum	79.08%	$0.358 \cdot 0.7908 = 0.283$	0.283
Core	26.77%	$2.645 \cdot 0.2677 = 0.708$	0.708
Upper Plenum	85%	$0.350 \cdot 0.85 = 0.297$	0.297
Outlet	100%	0.016	0.059
Pipe1	100%	0.043	
Fuel Pump	100%	0.025	0.025
Pipe2	100%	0.023	0.023
Heat Exchanger	94.77%	$0.182 \cdot 0.9477 = 0.173$	0.173
Pipe3	100%	0.062	0.062
Inlet	100%	0.082	0.275
Downcomer	100%	0.192	
Total	-	1.904	1.905

The MSRE core region, consisting of 1150 fuel channels and 618 graphite matrixes, was treated as a porous medium. A standard model was applied for coefficients of $k - \varepsilon$ correlation, and Blasius correlation was used for Darcy friction coefficients [3]. The fuel pump was simulated by a momentum force in the direction of flow and was able to establish a constant volumetric flow rate of 1200 gallons/min (0.07571 m^3/s), which equals to the operation flow rate in the MSRE design. In the heat exchanger zone, Darcy friction factors were adjusted to cause a pressure drop of $\sim$140 kPa at the nominal condition. The fuel salt was assumed to be incompressible, and its thermal-physical properties at 922 K are given in Table 3.6.

Table 3.6: Thermal-physical properties of molten salt used in MSRE GeN-Foam model [19].

Parameter	Value
Density (ρ), $\mathrm{kg\,m^{-3}}$	2258.6
Thermal Expansion Coefficient (α), $\mathrm{K^{-1}}$	$2.1 \cdot 10^{-4}$
Specific Heat (c_p), $\mathrm{J\,kg^{-1}\,K^{-1}}$	1967.796
Dynamic Viscosity (μ), $\mathrm{Pa\,s}$	0.00785
Prandtl Number	10.7

The boundary conditions applied in GeN-Foam model are summarized in Table 3.7. Note that the boundary condition of velocity on walls was set to "slip" rather than "noSlip" because the meshes near walls have not been refined yet. With large cells near walls, the "slip" boundary condition neglected the viscous effect, so Darcy friction coefficients in Equation (2.10) were provided to calculate the pressure drop.

Table 3.7: Boundary conditions applied in MSRE GeN-Foam model.

Parameter	Front / Back	Walls
Static Pressure (p)	wedge	calculated
Pseudo Hydrostatic Pressure ($p - \rho g H$)	wedge	fixedFluxPressure
Velocity ($\boldsymbol{u}$)	wedge	slip
Temperature (T)	wedge	zeroGradient
Turbulent Thermal Diffusivity (α_T)	wedge	zeroGradient
Turbulent Kinetic Energy (k)	wedge	zeroGradient
Dissipation Rate of Turbulent Kinetic Energy (ε)	wedge	zeroGradient
Turbulent Kinematic Viscosity (ν_T)	wedge	zeroGradient
Neutron Flux (ϕ)	wedge	fixedValue: 0
Adjoint Neutron Flux (ϕ^*)	wedge	fixedValue: 0
Concentration of DNPs (C)	wedge	zeroGradient
Importance of DNPs (C^*)	wedge	zeroGradient

Some simplifications applied to the MSRE GeN-Foam model are listed as follows:

- No control rods modeling;
- No heat transfer between the core and the downcomer;
- No bypass flow from the downcomer to the upper plenum.

Besides, during the simulations, a few vortexes were observed when flow entered the core from the lower plenum. In order to eliminate them, a large flow resistance in the XY-plane

at the bottom of the core was applied. This should not affect our steady-state results as long as the flow rate keeps at 0.07571 m^3/s. In reality, these vortexes are avoided by the existing of anti-swirl vanes in the lower plenum.

3.2 Molten Salt Fast Reactor Model

The Molten Salt Fast Reactor, currently supported by Euratom, is a liquid-fueled, fast-spectrum MSR without employing any solid moderator. It was selected and used as a reference model to study the effects of fuel salt compressibility and radiative heat transfer in MSRs. The MSFR Serpent model, developed in Serpent 2, was used to generate neutron group constants. The MSFR GeN-Foam model, developed in GeN-Foam, was used to perform multi-physics calculations.

MSFR Serpent model

A neutronics model was built in Serpent-2 to generate group constants at a reference state of 900 K, an increased temperature of 1200 K, and a reduced salt density of -10%, adopting ENDF/B-VII.1 nuclear data library with six neutron energy groups (Table 3.8).

Table 3.8: Neutron energy group's boundaries in MSFR model [28].

Neutron Energy Group	1	2	3	4	5	6
Upper Boundary, MeV	7.485E-4	5.531E-3	2.479E-2	4.979E-1	2.231	12

The core of the MSFR is a cylinder whose diameter and height are both equal to 225.5 cm. The core is radially surrounded by a 50 cm thick fertile blanket, and the fertile blanket is surrounded by a 20 cm thick boron carbide layer to absorb the remaining neutrons and protect the heat exchangers. In addition, there are 100 cm thick nickel-based alloy reflectors covering the top and the bottom of the core. The XZ- and XY-plane of the MSFR Serpent model are given in Figures 3.3 and 3.4, respectively.

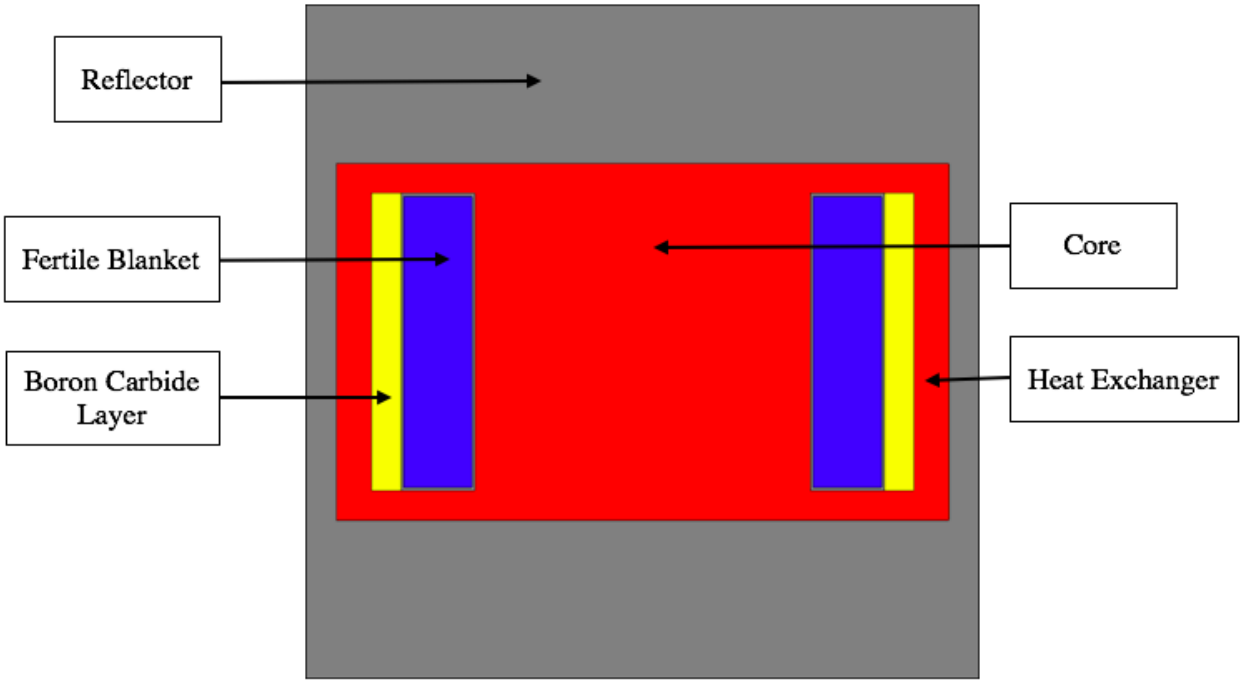

Figure 3.3: XZ-plane of MSFR Serpent model.

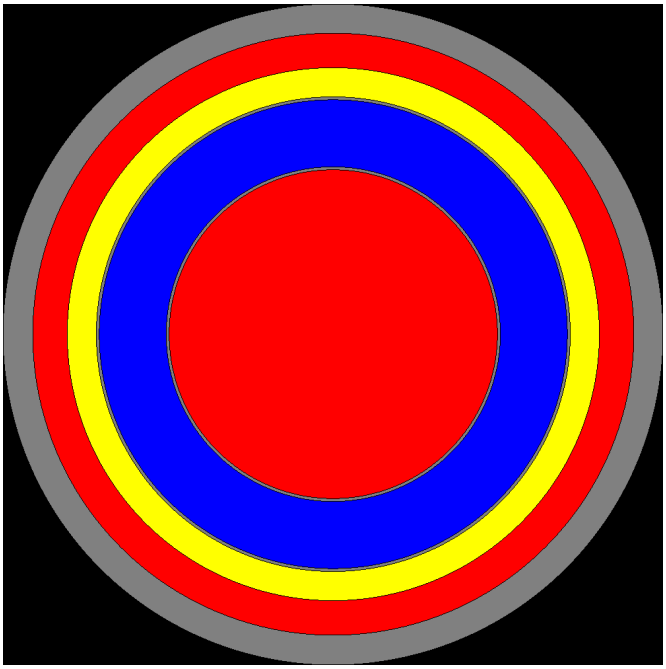

Figure 3.4: XY-plane of MSFR Serpent model.

Two different fuel salts, fluoride salt with thorium fuel and chloride salt with uranium fuel, were considered and used in the study. Composition and density of materials at 900 K in each region are summarized in Table 3.9, as well as the decay constants of six DNP groups are summarized in Table 3.10.

Table 3.9: Material information at 900 K in MSFR Serpent model.

Component	MSFR with Fluoride Salt	MSFR with Chloride Salt
Core and Heat Exchanger	$LiF - ^{232}ThF_4 - ^{233}UF_4$ (77.5-20-2.5 with 99.995 mol% ^{7}Li) Density of 4189 kg m^{-3}	$Na^{37}Cl - ^{238}U^{37}Cl_3 - ^{239}Pu^{37}Cl_3$ (60-35-5 mol%) Density of 3358 kg m^{-3}
Fertile Blanket	$LiF - ^{232}ThF_4$ (77.5-22.5 mol%) Density of 4189 kg m^{-3}	$Na^{37}Cl - ^{238}U^{37}Cl_3$ (60-40 mol%) Density of 3358 kg m^{-3}
Boron Carbide Layer	B_4C (natural boron with 19.9 mol% ^{10}B and 80.1 mol% ^{11}B) Density of 2520 kg m^{-3}	
Reflector	$Ni - W - Cr - Mo - Fe - Ti - C - Mn - Si - Al - B - P - S$ (79.432-9.976-8.014-0.736-0.632-0.295-0.294-0.257-0.252-0.052-0.033-0.023-0.004 mol%) Density of 10000 kg m^{-3}	

Table 3.10: DNP group decay constants at the reference state in MSFR model.

DNP Group	1	2	3	4	5	6
Fluoride System Decay Constant, s^{-1}	1.288E-2	3.465E-2	1.195E-1	2.910E-1	8.552E-1	2.615
Chloride System Decay Constant, s^{-1}	1.338E-2	3.118E-2	1.184E-1	3.107E-1	8.874E-1	2.955

The group constants generated by Serpent 2 were then imported into GeN-Foam by an Octave script. Their corresponding zones in the GeN-Foam model are summarized in Table 3.11.

Table 3.11: Group constant regions in MSFR Serpent and GeN-Foam models.

Regions in Serpent Model	Corresponding Regions in GeN-Foam Model
Core	Core
Heat Exchanger	Pump, Intermediate, Heat Exchanger

MSFR GeN-Foam model

By courtesy of Texas A&M University [13], a two-dimensional MSFR model was built in GeN-Foam, and its meshes are shown in Figure 3.5. This model is divided into four regions: the core, the pump, the intermediate, and the heat exchanger. All zones, except the heat exchanger, were modeled as clear fluid flows (100% fuel salt). The heat exchanger was modeled as a porous medium with a void fraction of 40%, and the Nusselt number was calculated by Dittus-Boelter equation [18].

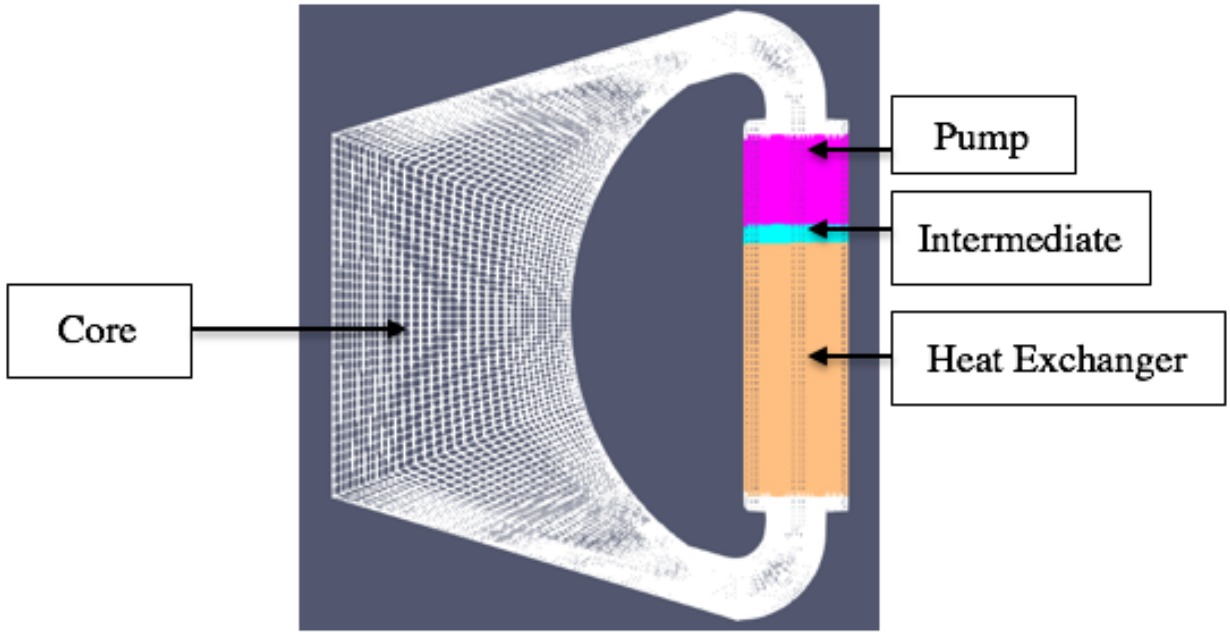

Figure 3.5: MSFR mesh in GeN-Foam.

The total volume of fuel salt is 18 m^3 (9 m^3 in the core and 9 m^3 out of the core), and a momentum force was provided in the pump region to establish a nominal flow rate of 4.5 m^3/s. The thermal-physical properties of fluoride and chloride salts are listed in Table 3.12.

Table 3.12: Thermal-physical properties of molten salts used in MSFR GeN-Foam model.

Parameter	Fluoride Salt [4] & [10]	Chloride Salt [6] & [7]
Density (ρ), $\mathrm{kg\,m^{-3}}$	$\rho_0 - \rho_0 \cdot \alpha \cdot (T - T_0)$ $+\rho_0 \cdot \beta_T \cdot (p - p_0)$	$\rho_0 - \rho_0 \cdot \alpha \cdot (T - T_0)$ $+\rho_0 \cdot \beta_T \cdot (p - p_0)$
Reference Density (ρ_0), $\mathrm{kg\,m^{-3}}$	4125	3337
Reference Temperature (T_0), K	973	923
Reference Pressure (p_0), Pa	2E5	1E5
Thermal Expansion (α), $\mathrm{K^{-1}}$	2.1E-4	2.7E-4
Compressibility (β_T), $\mathrm{m\,s^2\,kg^{-1}}$	0 or 1.6E-10 (incomp. vs. comp.)	0 or 1.9E-10 (incomp. vs. comp.)
Specific Heat Capacity (c_p), $\mathrm{J\,kg^{-1}\,K^{-1}}$	1455	536.6
Dynamic Viscosity (μ), $\mathrm{Pa\,s}$	0.01	0.0038
Thermal Conductivity (λ), $\mathrm{W\,m^{-1}\,K^{-1}}$	1.0	0.5

For the study of fuel salt compressibility effects in the MSFR, it is necessary to create an open boundary somewhere on the wall (e.g., a small inlet on top of the pump) to adjust the pressure and avoid a solver failure during transient calculations. The boundary conditions at inlet were set to "totalPressure" for pressure and "pressureInletOutletVelocity" for velocity. With a closed boundary, the total mass or the average density in the system is always conserved. Since liquid has a very small compressibility, as temperature increases the pressure has to explode dramatically to satisfy Equation (2.24). In reality, it is not physical to design a reactor without an expansion vessel. Other boundary conditions applied in the MSFR GeN-Foam model are summarized in Table 3.13.

Table 3.13: Boundary conditions applied in MSFR GeN-Foam model.

Parameter	Front / Back	Walls
Static Pressure (p)	wedge	calculated
Pseudo Hydrostatic Pressure ($p - \rho g H$)	wedge	fixedFluxPressure
Velocity ($\boldsymbol{u}$)	wedge	noSlip
Temperature (T)	wedge	zeroGradient
Turbulent Thermal Diffusivity (α_T)	wedge	zeroGradient
Turbulent Kinetic Energy (k)	wedge	kqRWallFunction
Dissipation Rate of Turbulent Kinetic Energy (ε)	wedge	epsilonWallFunction
Turbulent Kinematic Viscosity (ν_T)	wedge	nutkWallFunction
Neutron Flux (ϕ)	wedge	albedo
Concentration of DNPs (C)	wedge	zeroGradient

Note that the albedo boundary condition was applied for the neutron flux on the wall

because the fuel salt circuit is surrounded by the reflectors and the fertile blanket, which are not included in the MSFR GeN-Foam model. The albedo coefficients on different parts of the wall were predicted by the MSFR Serpent model.

For the study of RHT effects in the fluoride MSFR, the "P1" radiation model was used, and the "MarshakRadiation" boundary condition [22] was applied to the incident radiation, G, on the wall. The radiation properties used in the "P1" model are listed in Table 3.14.

Table 3.14: Radiation properties of molten fluoride salt.

Parameter	Value
Absorption Coefficient (a), m^{-1}	85
Emission Coefficient (e), m^{-1}	85
Scattering Coefficient (σ), m^{-1}	0
Emission Contribution (E), $\mathrm{W\,m}^{-3}$	0

It was assumed that absorption and emission coefficients are constant, and there is no scattering in the fluoride salt. It is clear that such assumptions would introduce some errors because those coefficients are actually non-constant and wavelength-dependent. However, fully resolving the shapes of coefficients would be very computationally expensive. One possible solution is to use the spectral banding method, which divides the real coefficient curves into discrete, constant bands over defined wavelength ranges [5]. Due to the time limit, in preliminary calculations only one value was assigned to each parameter over the entire wavelength.

Chapter 4

Steady-State and Transient Analyses for the MSRE

4.1 Steady-State Analysis

At designed power of 10 MWth, the steady-state calculation was performed to validate the MSRE model developed in GeN-Foam. By adjusting the pump momentum source in the pump region, the flow rate was fixed to the operational value of 1200 gallons/min (0.07571 m^3/s). The fuel salt residence time in each component of the MSRE GeN-Foam model has been matched with the MSRE designed values, as demonstrated in Table 4.1, and the calculated velocity distribution is shown in Figure 4.1.

Table 4.1: Fuel salt residence time in MSRE.

Region	Fuel Salt Residence Time, s	
	Fuel Salt Volume/Volumetric Flow Rate	MSRE Report [30]
Lower Plenum	0.283/0.07571 = 3.8	3.8
Core	0.708/0.07571 = 9.4	9.4
Upper Plenum	0.297/0.07571 = 3.9	3.9
Outlet	0.016/0.07571 = 0.2	0.8
Pipe1	0.043/0.07571 = 0.6	
Fuel Pump	0.025/0.07571 = 0.3	0.3
Pipe2	0.023/0.07571 = 0.3	0.3
Heat Exchanger	0.173/0.07571 = 2.3	2.3
Pipe3	0.062/0.07571 = 0.8	0.8
Inlet	0.082/0.07571 = 1.1	3.6
Downcomer	0.192/0.07571 = 2.5	
Total	25.2	25.2

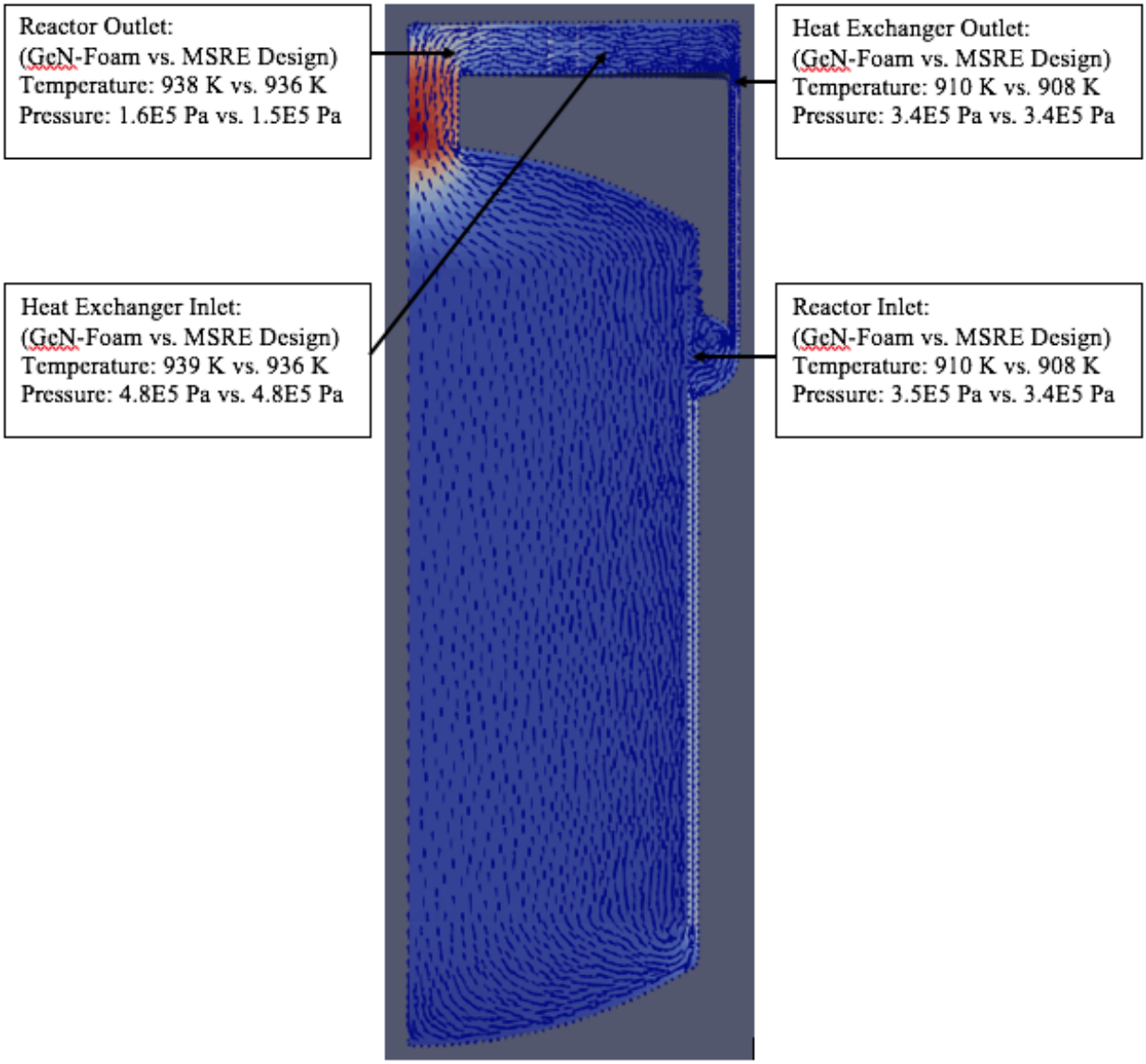

Figure 4.1: Velocity distribution in MSRE GeN-Foam model.

In addition, the values of temperature and pressure at different locations (reactor inlet, reactor outlet, heat exchanger inlet and heat exchanger outlet) were measured and indicated on the above plot. They have a good agreement with the MSRE design.

Effect of delayed neutron precursor drift

To benchmark the delayed neutron precursor drift against available experimental data from the MSRE, two steady-state conditions were simulated at zero power: stationary salt and flowing salt at 1200 gallons/min (0.07571 m^3/s). The change of reactivity and the change of total effective delayed neutron fraction, due to the fuel movement, were calculated by GeN-Foam and are summarized in Table 4.2.

Table 4.2: Reactivity change and total effective delayed neutron fraction change.

Parameter	GeN-Foam	MSRE Reports
Reactivity Change ($\Delta\rho$)	-224 pcm	-212 pcm [29]
Total Effective Delayed Neutron Fraction Change ($\Delta\beta_{eff}$)	-220 pcm	-304 pcm [16]

As molten salt circulates in the reactor, the calculated reactivity change of -224 pcm agrees with the zero-power physics experiment data of -212 pcm. The calculated β_{eff} drop of 220 pcm is smaller than ORNL's prediction of 304 pcm. The discrepancy is due to the simplification in the ORNL's MSRE model, where the fission of delayed neutrons was only considered in the graphite-moderated core region and the contribution of delayed neutrons emitted in the upper and lower plenum was not included. This led to an underestimation of β_{eff} when the salt was flowing, and thus the change of β_{eff} was overestimated. The total neutron flux distribution under two different conditions, (a) salt stationary vs. (b) salt circulation, in the MSRE GeN-Foam model is plotted and compared in Figure 4.2.

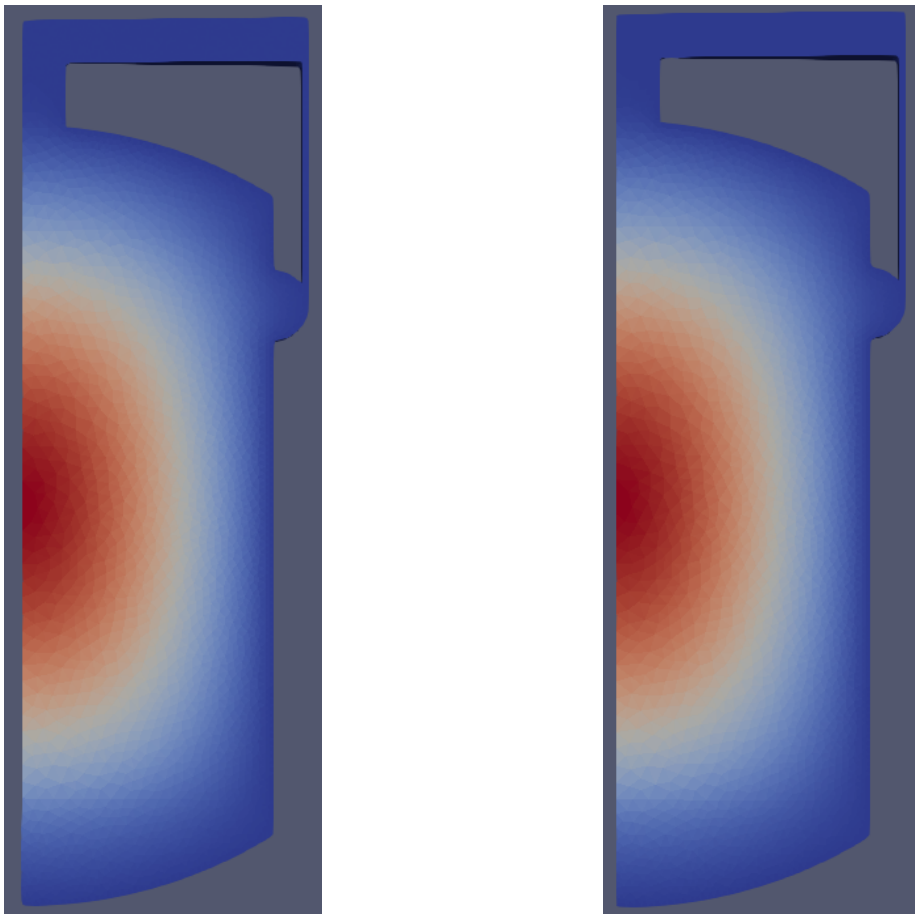

(a) Salt stationary. (b) Salt circulation.

Figure 4.2: Total neutron flux distribution in MSRE.

It shows that most neutrons are concentrated in the center of the core because more fission reactions are happening there. No significant difference can be found between two plots because the delayed neutrons only take account of less than 1% of total number of neutrons. However, different phenomena are captured for the delayed neutron precursor concentration, as illustrated in Figures 4.3 to 4.8.

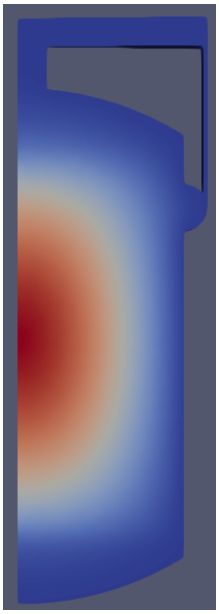

(a) Salt stationary.

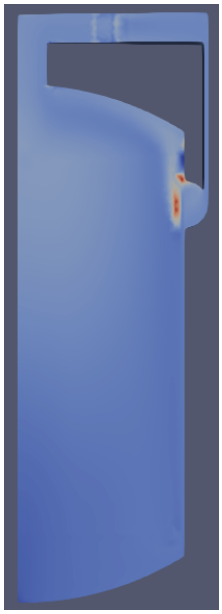

(b) Salt circulation.

Figure 4.3: DNP_1 concentration in MSRE.

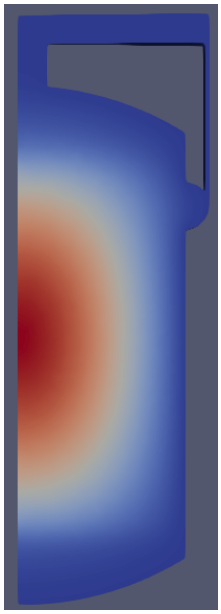

(a) Salt stationary.

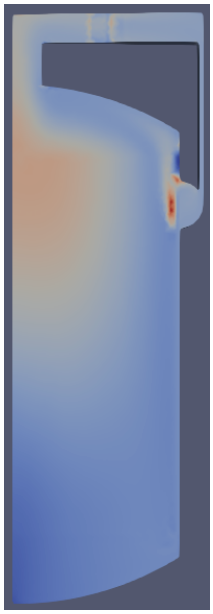

(b) Salt circulation.

Figure 4.4: DNP_2 concentration in MSRE.

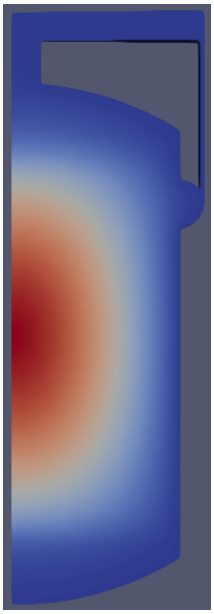

(a) Salt stationary.

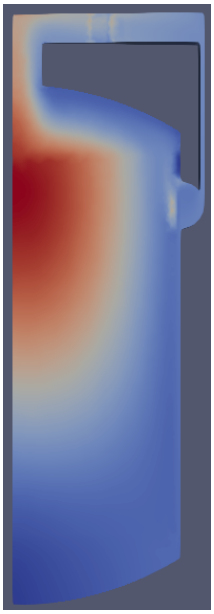

(b) Salt circulation.

Figure 4.5: DNP_3 concentration in MSRE.

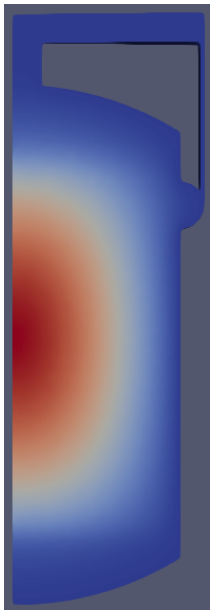

(a) Salt stationary.

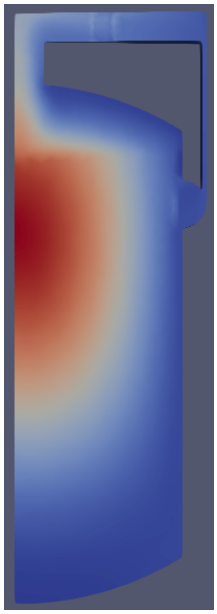

(b) Salt circulation.

Figure 4.6: DNP_4 concentration in MSRE.

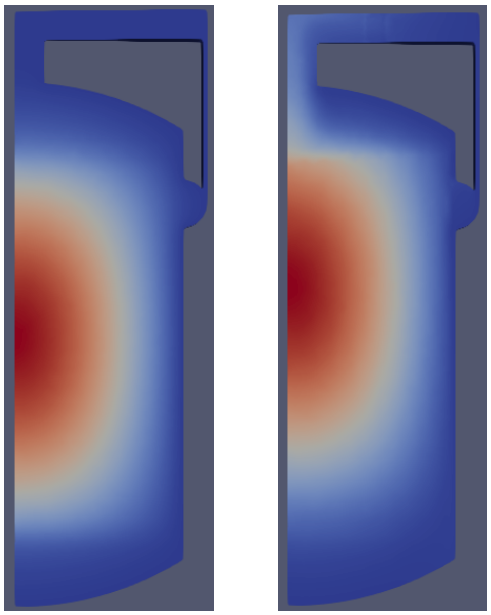

(a) Salt stationary. (b) Salt circulation.

Figure 4.7: DNP_5 concentration in MSRE.

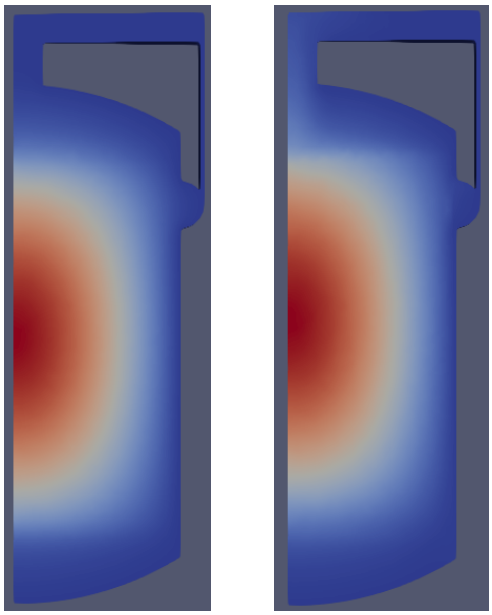

(a) Salt stationary. (b) Salt circulation.

Figure 4.8: DNP_6 concentration in MSRE.

In the static fuel salt, the DNP concentration has a similar shape as the total neutron flux since DNPs are not moving, and their concentration is proportional to the neutron flux. When the fuel salt starts to move, significant changes are observed on the concentration plots of DNP_1 and DNP_2. This is because precursors drift as fuel salt circulates in the reactor, and DNP_1 and DNP_2 have the smallest decay constant and longest half-life (greater than 30 s), so they have sufficient time to distribute all over the MSRE core and the external loop before decaying. As the decay constant increases and the half-life decreases, DNP_3 and DNP_4 have higher concentration at the top of the core and the upper plenum region. Finally, for DNP_5 and DNP_6 with the largest decay constant and shortest half-life (less than 2 s), they decay very quickly before moving out of the core, resulting in a minor change on the concentration plots.

4.2 Transient Scenario Analysis

In most reactors, there are three main transient initiators, i.e., reactivity insertion, heat exchanger failure and fuel pump coast-down. The following subsections discuss the three possible MSRE responses to the corresponding transient initiators. The transient calculations were conducted following the steady-state calculation at 10 MWth with a flow rate of 1200 gallons/min (0.07571 m^3/s). Even though the steady-state results agree with the MSRE design, the aforementioned assumptions in Section 3.1 and the 2D-RZ geometry applied in

the modeling might affect the thermal-hydraulics calculations under various transient conditions. Thus, further investigations in this area are important and necessary. Note that the main purpose of these analyses is to demonstrate the transient modeling capability of GeN-Foam because a few bugs have been identified and fixed during the study.

Unprotected transient over power (UTOP)

An UTOP may occur following a reactivity insertion, which is particularly demanding from a numerical point of view, thus it represents a good test for the MSRE GeN-Foam model. It also gives rise to the maximum power excursion for a given reactivity insertion. For simplicity, three step-wise reactivity insertions have been investigated: 100 pcm (prompt subcritical), 440 pcm (prompt critical) and 500 pcm (prompt supercritical) reactivity insertions. In GeN-Foam, such reactivity insertions were introduced by directly changing the k_{eff} value or the number of neutrons produced per fission at the beginning of the transients. The resulting relative power and average fuel salt temperature profiles are given in Figures 4.9 and 4.10, respectively.

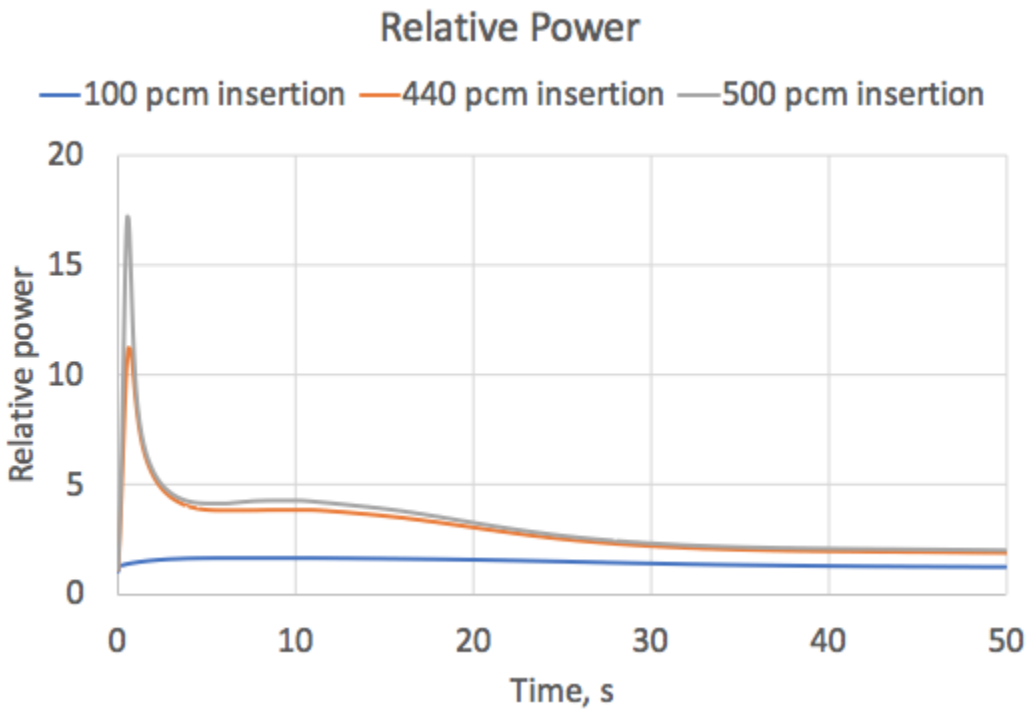

Figure 4.9: Relative power in MSRE during an UTOP.

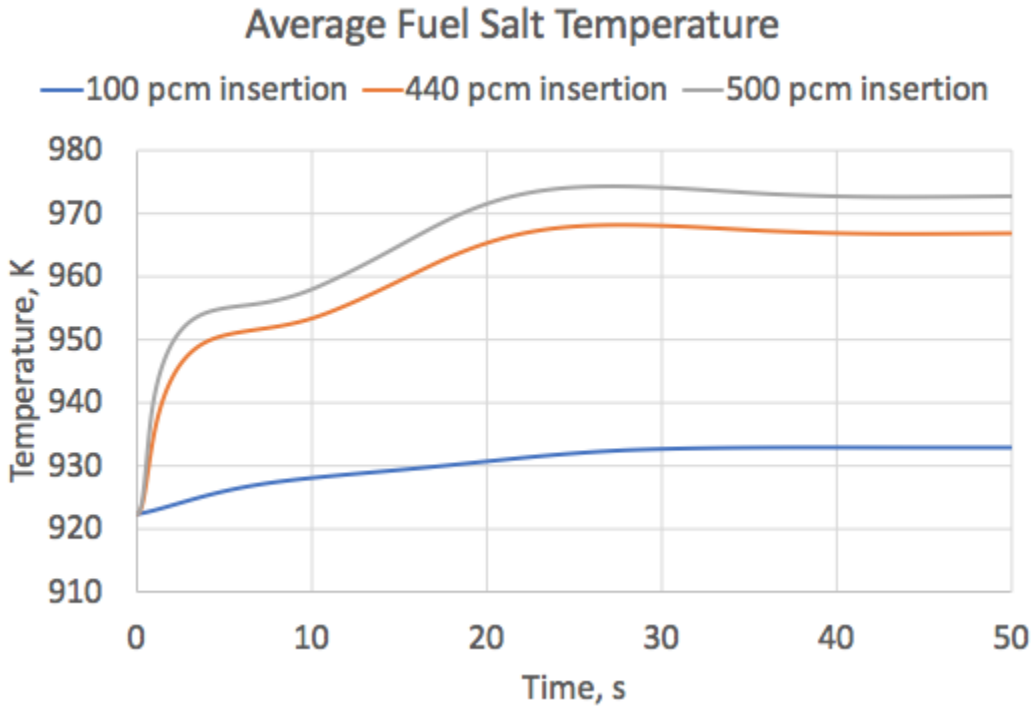

Figure 4.10: Average fuel salt temperature in MSRE during an UTOP.

It can be observed that by inserting a larger reactivity, a larger power peak occurs at an earlier time. The prompt power increase is triggered by a step-wise reactivity insertion and leads to a rapid temperature rise. Even the reactor is at prompt critical ($\rho = \beta_{eff} = 0.44\%$) and prompt supercritical ($\rho = 0.5\% > \beta_{eff} = 0.44\%$) states, the consequent negative reactivity insertion due to the Doppler effect is able to quickly reduce the power, and the final temperature increase is determined by the amount of initial reactivity inserted.

Unprotected loss of heat sink (ULOHS)

An ULOHS may occur following a loss of coolant salt in the reactor secondary loop. For simplicity, the loss of cooling capability in the heat exchanger was simulated by removing all related heat transfer coefficients in the heat exchanger zone. The resulting responses are shown in Figures 4.11 and 4.12, respectively.

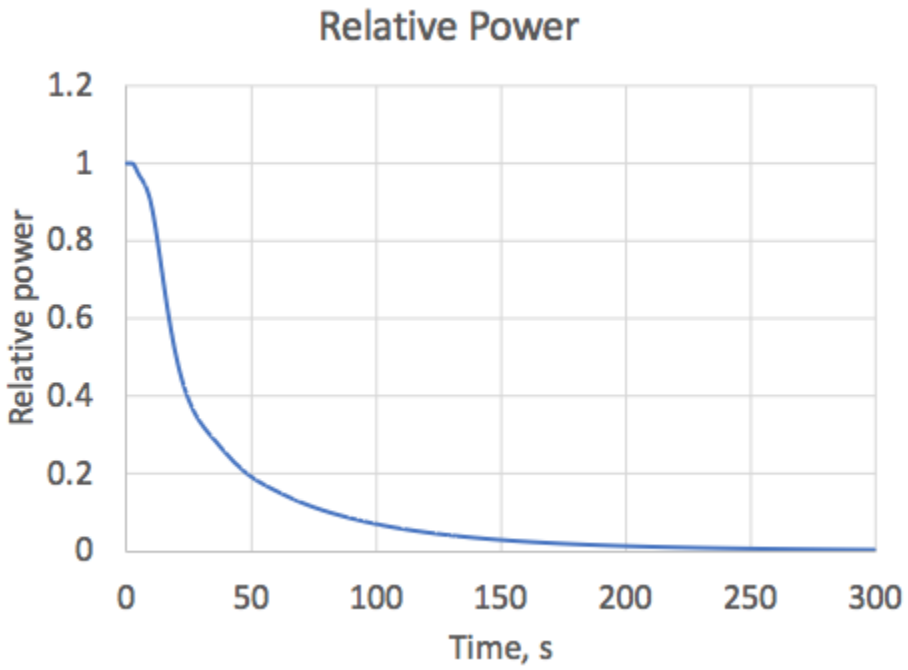

Figure 4.11: Relative power in MSRE during an ULOHS.

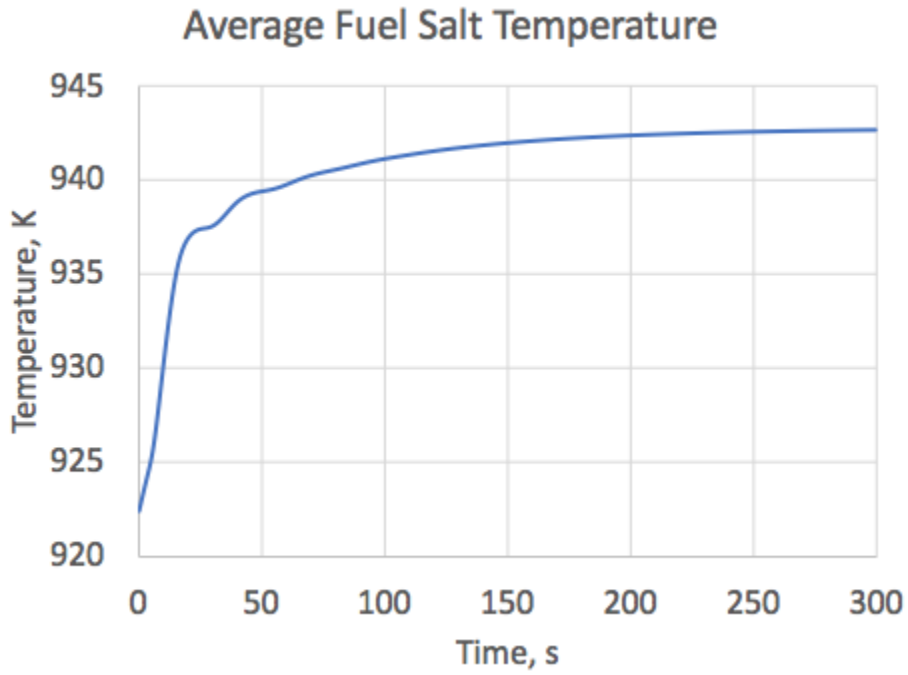

Figure 4.12: Average fuel salt temperature in MSRE during an ULOHS.

As soon as the cooling capability is lost, the fuel salt temperature increases, and thus the temperature feedback quickly reduces the power and shuts down the reactor. The temperature in the primary loop is gradually homogenized because the heat sink is completely removed. In fact, a more realistic scenario should include the effect of decay heat, which would further increase the fuel salt temperature and lead to a faster and larger power drop.

Unprotected loss of flow (ULOF)

An ULOF with a fuel pump coast-down may occur in the reactor following an electricity shortage. In this simulation, the pump force in the primary circuit was assumed to drop exponentially, starting from 1 second with a time constant of ∼8 seconds. After ∼27 seconds, the flow rate dropped to 1/10 of the nominal operating flow rate, as shown in Figure 4.13. The resulting power and average fuel salt temperature are plotted in Figures 4.14 and 4.15, respectively.

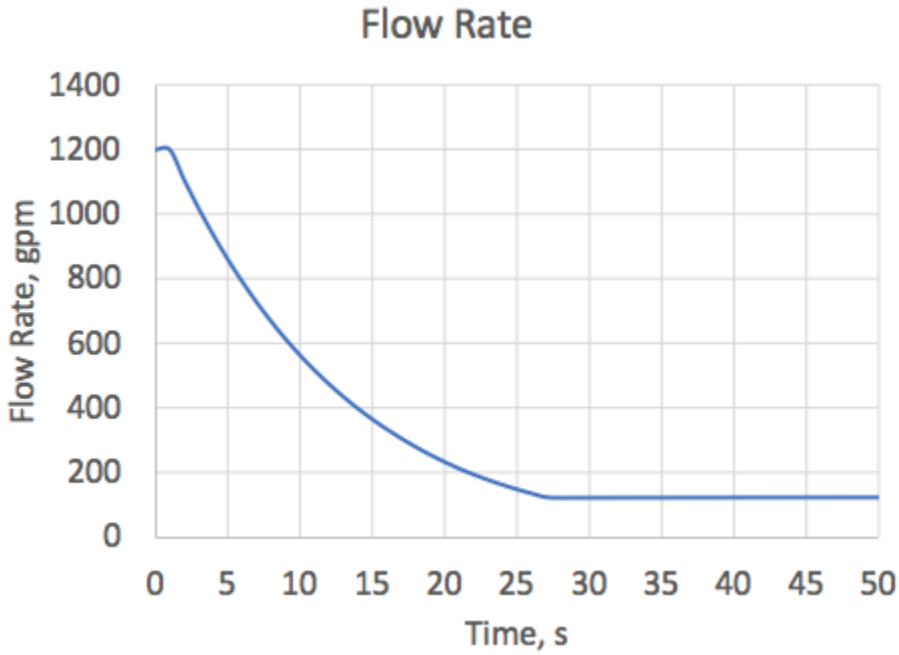

Figure 4.13: Flow rate in MSRE during an ULOF.

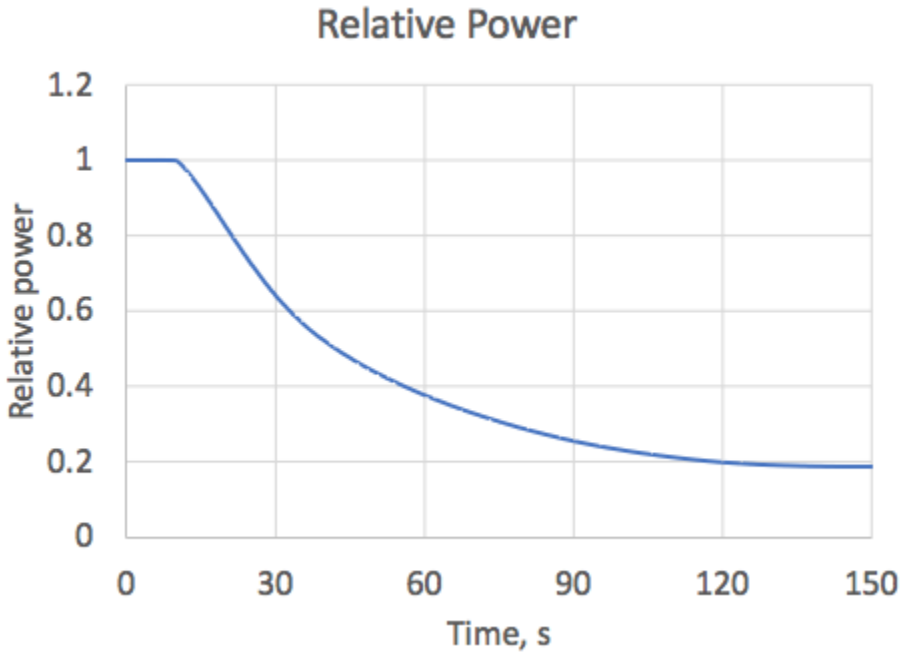

Figure 4.14: Relative power in MSRE during an ULOF.

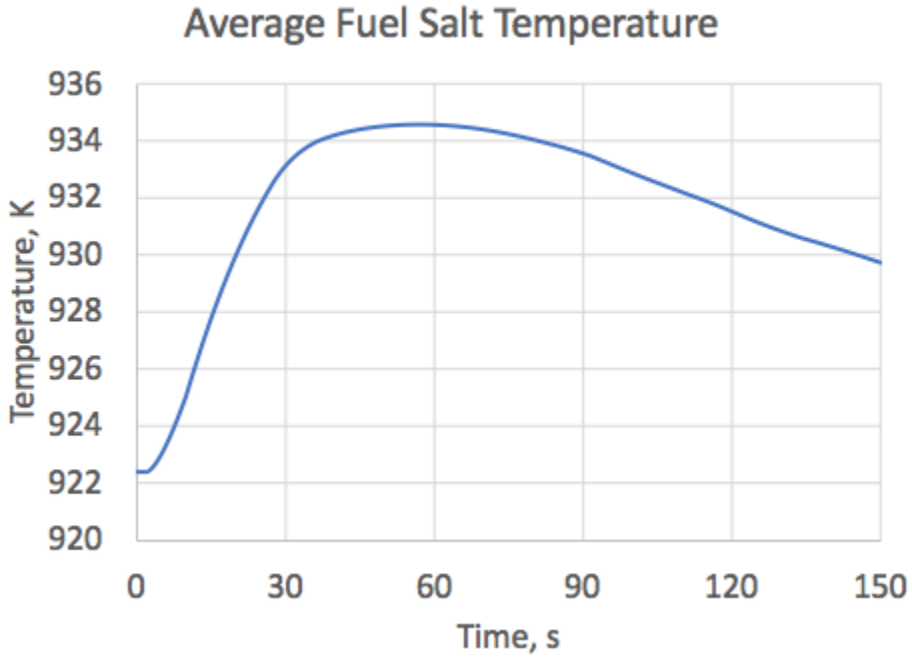

Figure 4.15: Average fuel salt temperature in MSRE during an ULOF.

As the flow rate decreases, the heat removing capability is receded, and the average fuel salt temperature initially increases. This temperature increase introduces a negative reactivity due to the Doppler effect and thus reduces the power. However, at the very beginning of the transient (1 second to ∼10 seconds), the power does not drop immediately because the speed of DNPs flowing out of the core becomes slower, resulting in a positive reactivity insertion and offsetting the negative temperature feedback. Finally, the salt temperature starts to decrease after reaching its peak point where the heat generating rate is equal to the heat removing rate.

Chapter 5

Fuel Salt Compressibility Effects in the MSFR

Two cases, incompressible flow and compressible flow, are analyzed and compared for the Molten Salt Fast Reactor. For the incompressible simulations, the isothermal compressibility coefficient, β_T, was set to 0 $\mathrm{m\,s^2\,kg^{-1}}$. On the contrary, a non-zero value was assigned to β_T in GeN-Foam for compressible simulations. The initial steady-state calculations were performed at the design thermal power of 3 GW. At the beginning of the reactivity insertion accident (RIA), a 500 pcm reactivity was added by modifying the value of k_{eff} or increasing the number of neutrons produced per fission.

5.1 Compressibility Effect in Molten Fluoride Salt

In the MSFR design, the molten fluoride salt was selected as the fuel carrier, as well as coolant. The obtained relative power and core outlet temperature change during a 500 pcm RIA are shown in Figures 5.1 and 5.2, respectively.

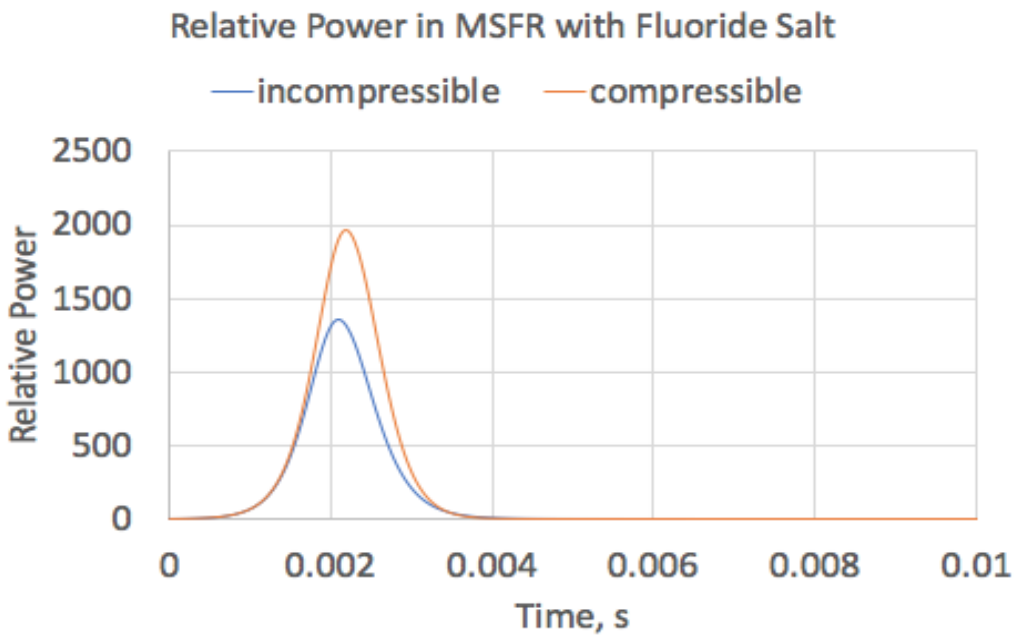

Figure 5.1: Relative power during the RIA in MSFR fluoride system.

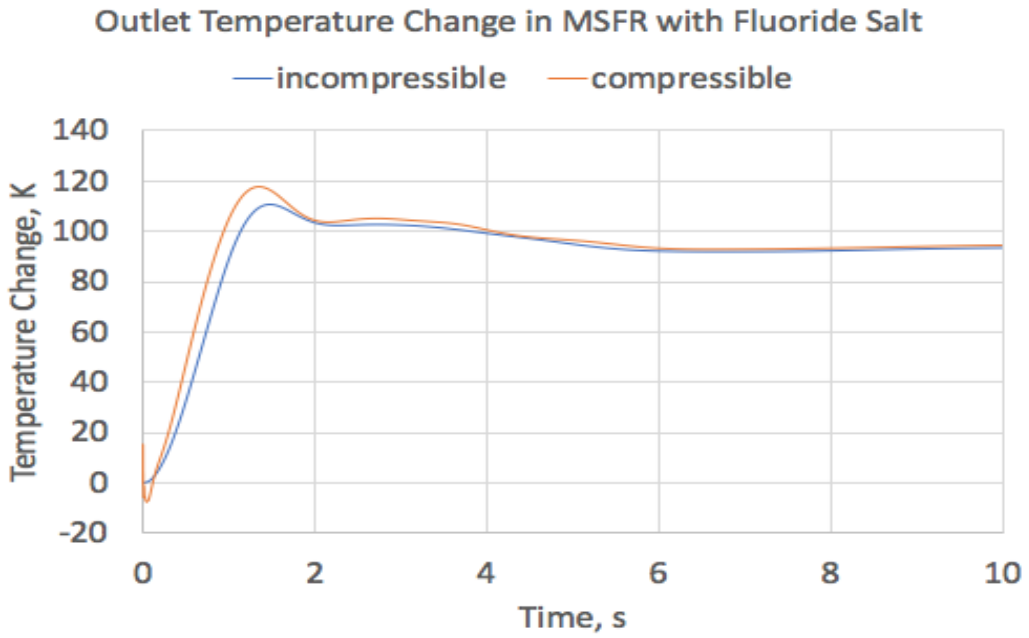

Figure 5.2: Core outlet temperature change during the RIA in MSFR fluoride system.

The plots show that the incompressible calculation underestimates the increase of power and core outlet temperature during the RIA. The incompressible assumption implies that the salt density is instantaneously related to the fluid temperature, as if the speed of sound were infinite. In fact, the propagation of pressure waves and the fuel salt expansion out of the core usually take several milliseconds or more. Therefore, the incompressible assumption leads to an overestimation of negative feedback, a lower power and a lower core outlet temperature. Moreover, in the compressible simulation the core outlet temperature oscillates at the very beginning of the transient (less than 0.1 s). This is because the pressure change related to pressure wave propagation leads to the core outlet flow rate oscillation (Figure 5.3), resulting in the temperature oscillation. However, this temperature oscillation is not captured in the incompressible case.

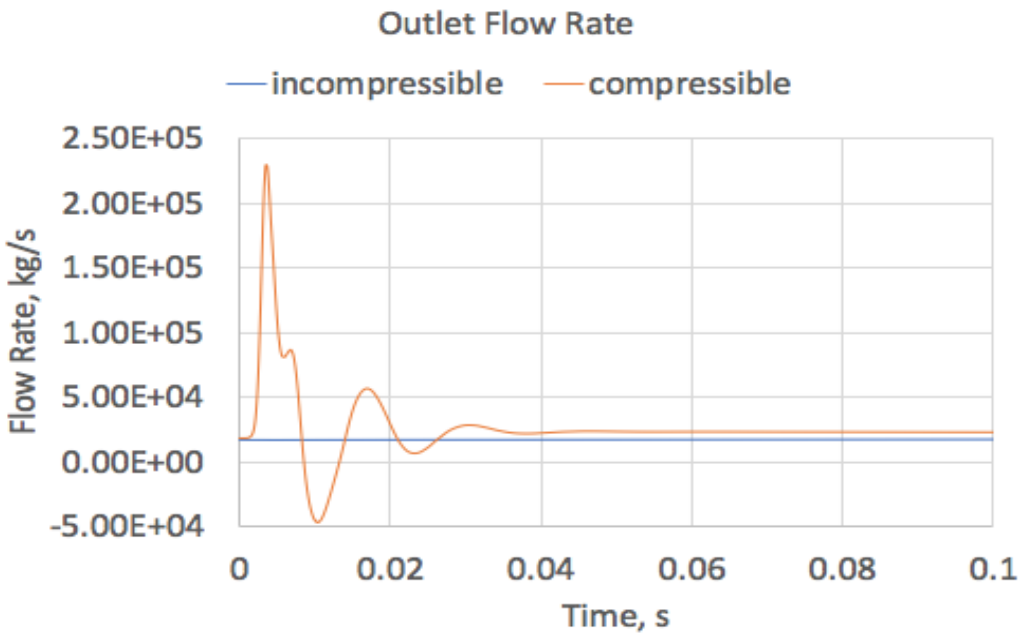

Figure 5.3: Core outlet flow rate during the RIA in MSFR fluoride system.

With an incompressible fluid assumption, the compressibility coefficient is zero, so there is no change in pressure field during the transient, and the pressure wave propagation cannot be observed. The pressure profiles in the compressible fluoride salt at various time steps are shown in Figure 5.4.

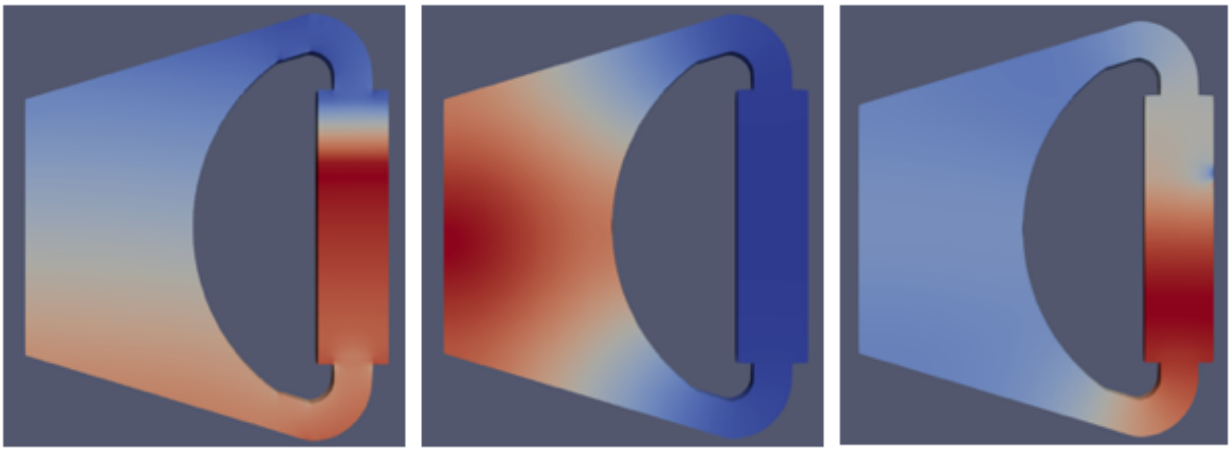

Figure 5.4: Pressure distribution at t = 0, 2E-3, and 4E-3 s (compressible fluoride salt).

It is obvious that the pressure waves take a finite time to move from the core center to the external circuit, resulting in a delay of fuel salt expansion or slowing down the negative reactivity insertion. Besides, even with the installation of gas removal equipment in liquid-fueled MSRs, it is expected that a small number of bubbles exist in salt during the reactor's operation. Since the presence of voids decreases the speed of sound in liquid, the effective compressibility of the mixture becomes larger. According to Aufiero's paper [2], when the MSFR design contains about 0.01% helium bubbles, the sound speed decreases approximately by a factor of 2 and the effective compressibility of fluoride salt increases approximately by a factor of 4. The new power and temperature profiles with a 500 pcm reactivity insertion, compared with preceding no-bubble compressible salt results, are plotted in Figures 5.5 and 5.6, respectively.

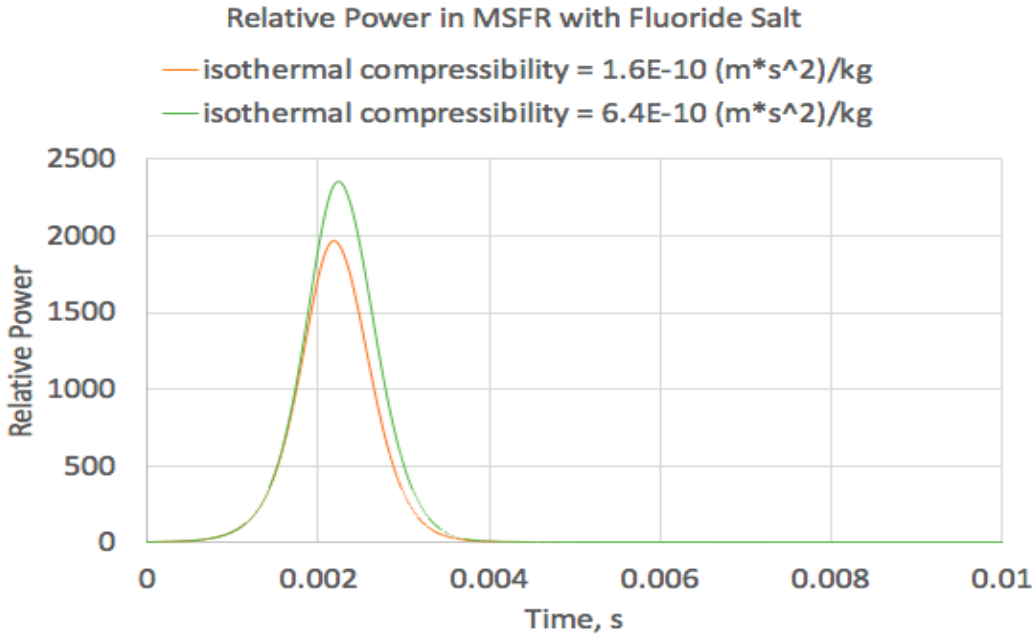

Figure 5.5: Relative power comparison in MSFR fluoride system.

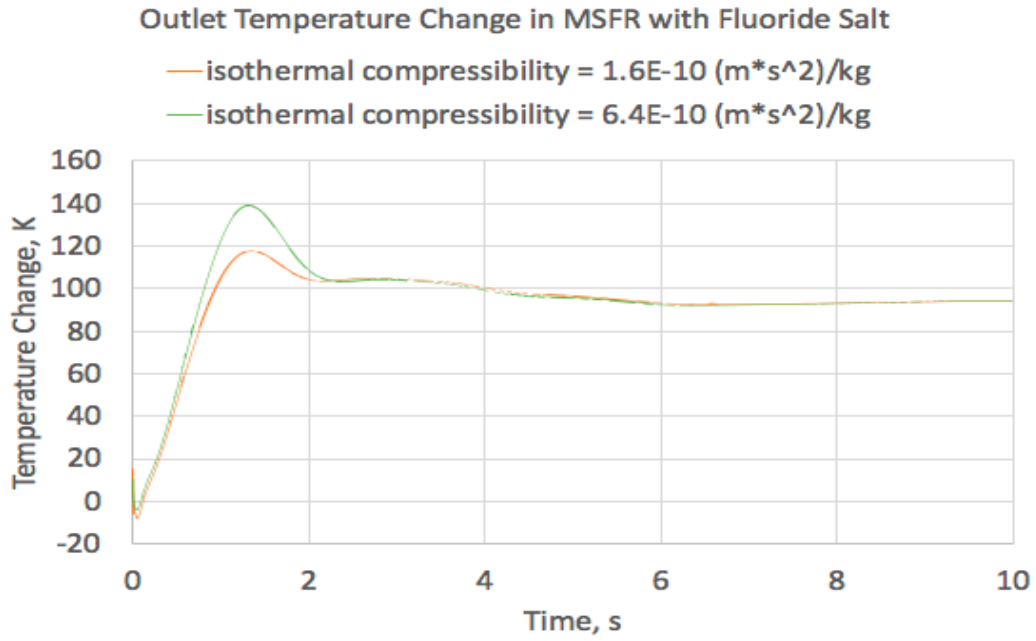

Figure 5.6: Core outlet temperature change comparison in MSFR fluoride system.

By increasing the compressibility coefficient, the speed of sound in salt decreases, and thus the negative expansion feedback further delays. As a result, the peak power increases by ∼20% and the maximum core outlet temperature increases by ∼20 K. In fact, a more accurate calculation should model the gas phase and bubbles' spatial distribution, rather than a simple adjustment or estimation of the salt compressibility.

5.2 Compressibility Effect in Molten Chloride Salt

The molten chloride salt was another possible candidate and used in GeN-Foam calculations. The obtained relative power and core outlet temperature change during a 500 pcm RIA are shown in Figures 5.7 and 5.8, respectively. The pressure wave propagation is given in Figure 5.9.

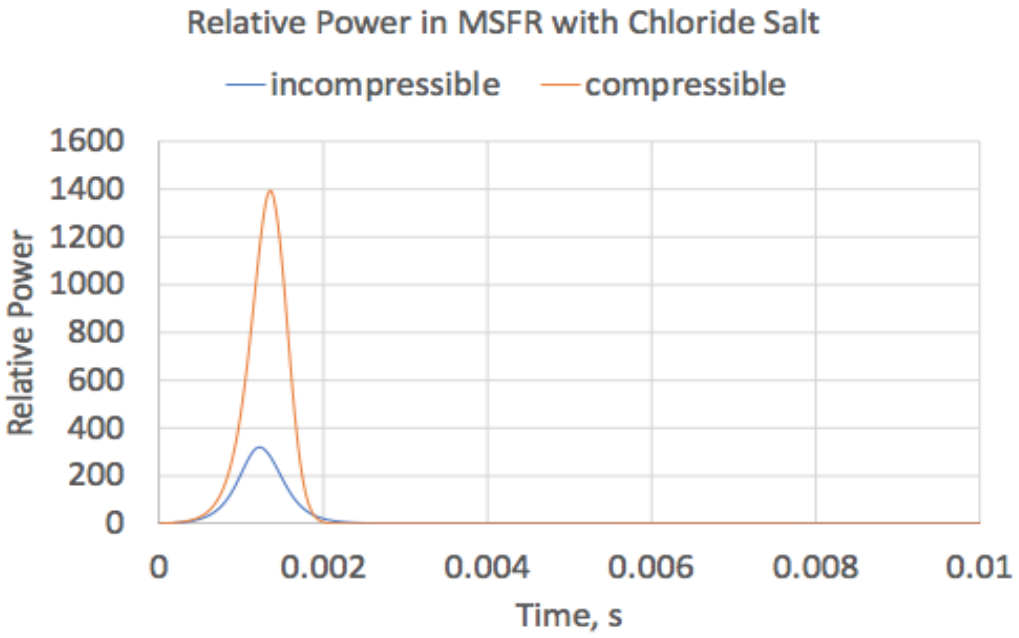

Figure 5.7: Relative power during the RIA in MSFR chloride system.

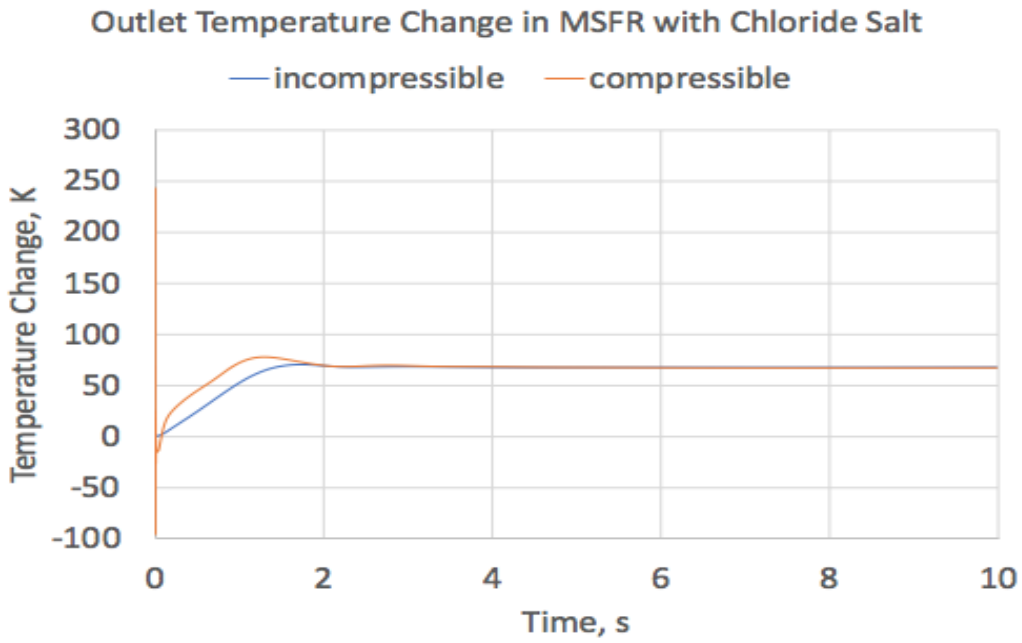

Figure 5.8: Core outlet temperature change during the RIA in MSFR chloride system.

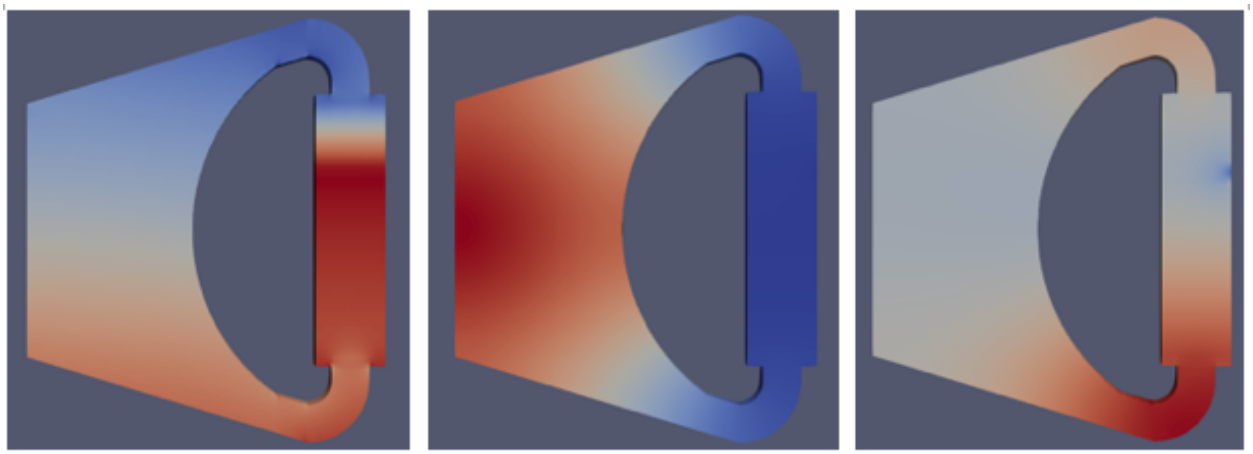

Figure 5.9: Pressure distribution at t = 0, 1E-3, and 2E-3 s (compressible chloride salt).

Similar to the MSFR fluoride system, a larger power excursion and a faster core outlet temperature rise are also observed in the compressible-fluid model of the chloride system. At the very beginning of the RIA compressible calculation, the core outlet temperature oscillates because of the flow rate variation. However, the compressibility effect is more exaggerated in the chloride system due to its harder neutron spectrum and shorter neutron prompt lifetime.

Chapter 6

Impacts of Radiative Heat Transfer in the MSFR

At the MSFR full power of 3 GWth, two initial steady-state calculations, without radiative heat transfer and with "P1" radiation model, were performed, respectively. Then a loss of flow scenario was simulated by exponentially reducing flow rate from 4.5 m^3/s to 0.5 m^3/s in 20 seconds (Figure 6.1). The obtained changes of average fuel salt temperature, core inlet temperature and core outlet temperature, with and without RHT, are shown in Figures 6.2 to 6.4, respectively.

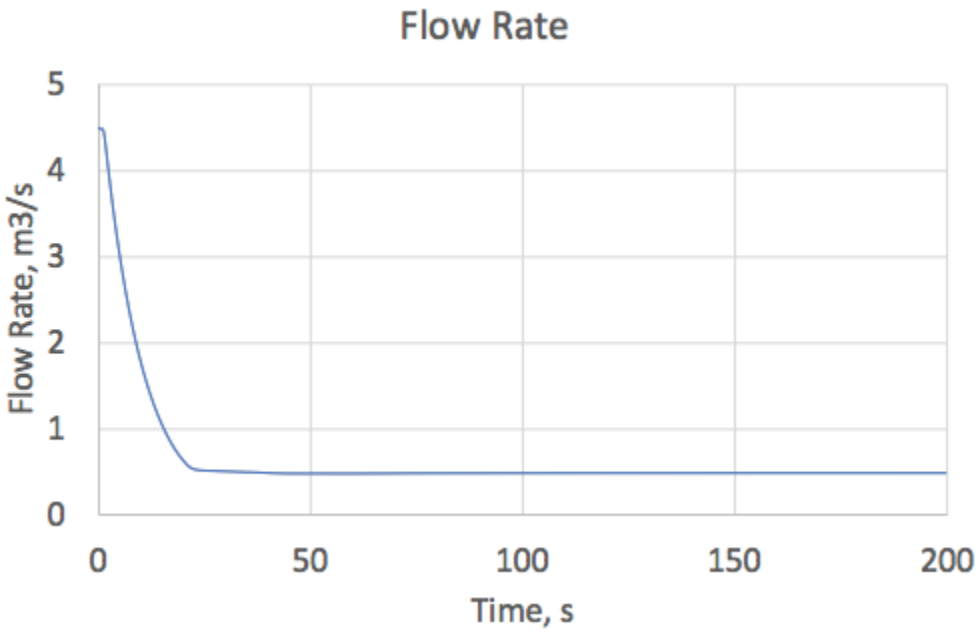

Figure 6.1: Flow rate in MSFR during an ULOF.

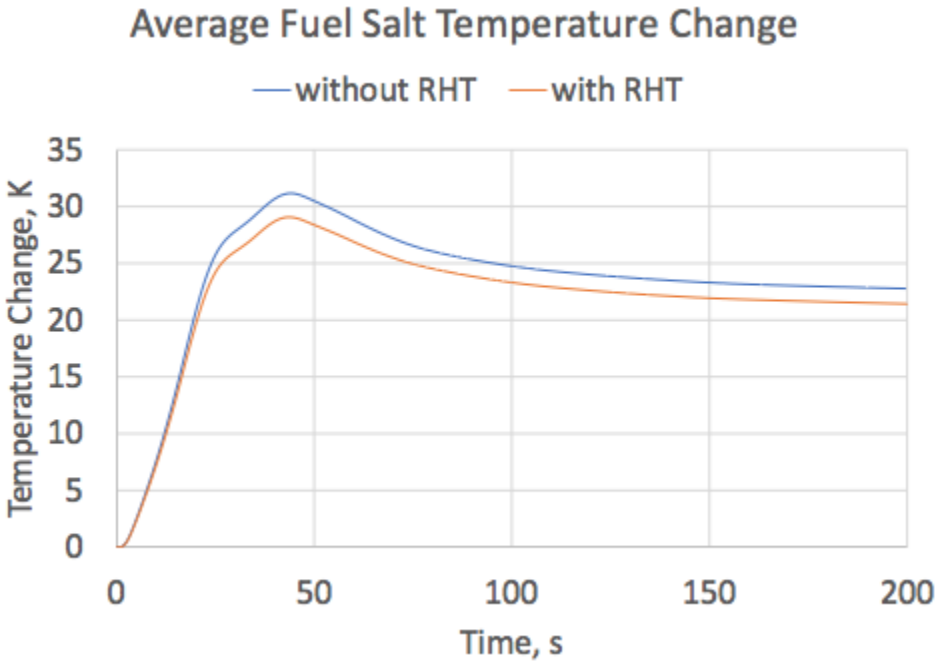

Figure 6.2: Change of average fuel salt temperature in MSFR during an ULOF.

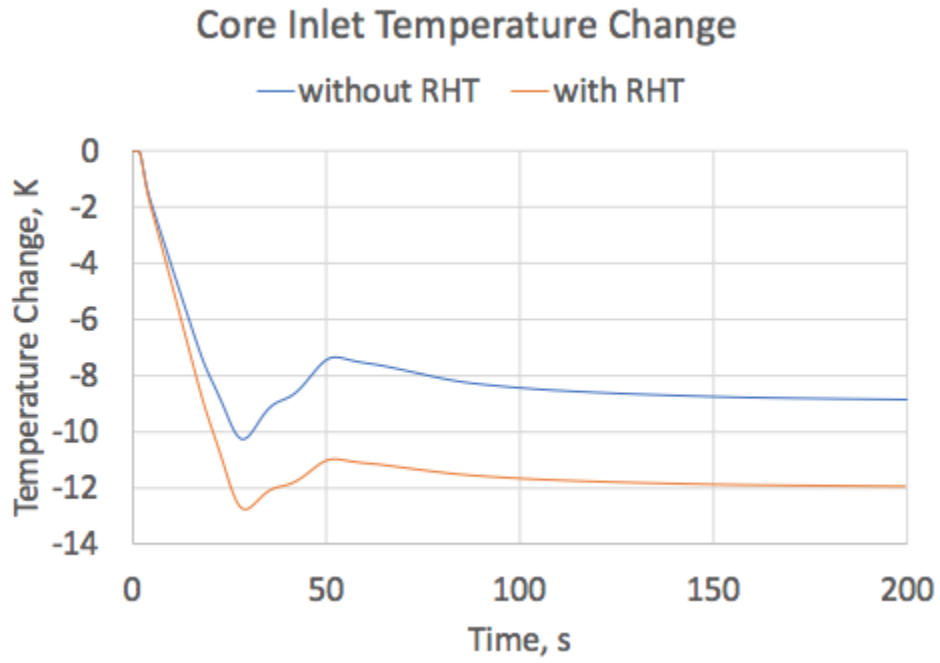

Figure 6.3: Change of core inlet temperature in MSFR during an ULOF.

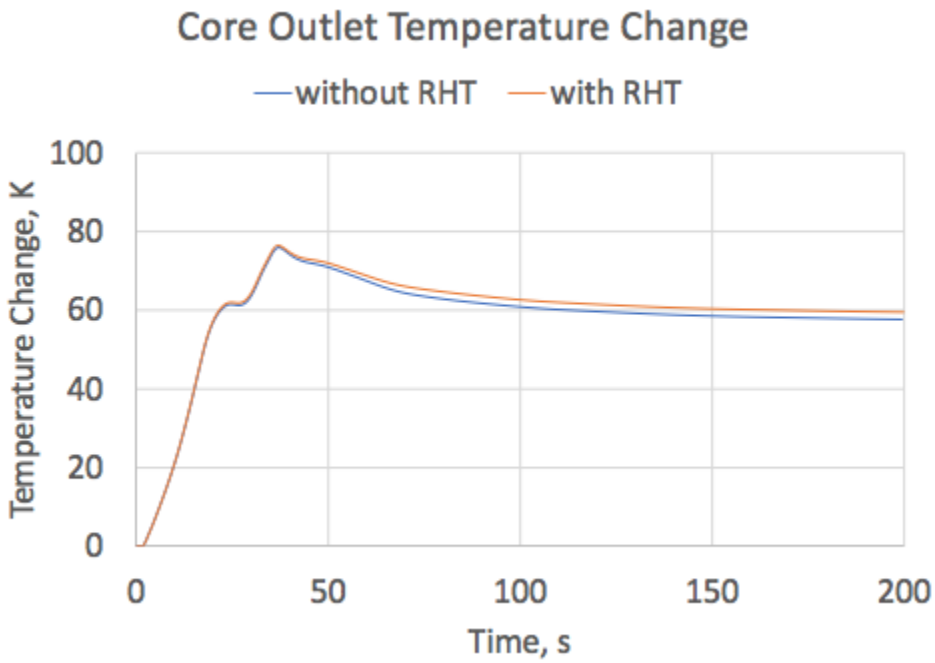

Figure 6.4: Change of core outlet temperature in MSFR during an ULOF.

During the unprotected loss of flow accident in the MSFR, the effective thermal conductivity of salt in the heat exchanger is enhanced due to the addition of radiative heat transfer, resulting in a larger temperature drop at the core inlet (or heat exchanger outlet), a larger temperature rise at core outlet, and a smaller average temperature rise in the reactor system, which are demonstrated in the above figures. However, these differences are all less than 5 K, not very significant in the fluoride MSFR. It would be interesting to see this RHT impact on other molten salt reactors with different radiation properties or using more accurate radiation models.

Chapter 7

Conclusions and Future Work

In 2002, the molten salt reactor concept was selected by the GIF as one of six most promising Generation IV nuclear energy systems. Modeling of liquid-fueled MSRs involves the simulation of peculiar phenomena whose treatment is not available in common reactor physcis tools. In particular, effects related to the delayed neutron precursor drift, fuel salt compressibility and radiative heat transfer within liquid salt need specific modeling and simulation capabilities. Thus, this dissertation described the development of the multi-physics code GeN-Foam and the high-fidelity MSR models.

For the GeN-Foam code development, an adjoint neutron flux solver has been developed and implemented in the neutronics sub-solver in order to calculate the effective delayed neutron fraction. A new linear equation of state, correlating the density of a fluid to its temperature and pressure, has been implemented in the OpenFOAM library and can be used by GeN-Foam to perform the compressible calculation. A radiation source term has been added into the thermal-hydraulics sub-solver to enable the radiation transport calculation.

The short-lived but enduring legacy, the Molten Salt Reactor Experiment, successfully operated from 1965 to 1969 at Oak Ridge National Laboratory, and it was selected as a reference model to study the effect of delayed neutron precursor circulation in liquid-fueled MSRs. The MSRE Serpent model, adopting ENDF/B-VII.1 nuclear data library with two neutron energy groups and six DNP groups, was built in Serpent 2 to generate neutron group constants for the MSRE GeN-Foam model, which was developed in GeN-Foam and used for multi-physics calculations. For zero-power steady-state simulations (salt at static vs. flowing at 1200 gallons/min), the calculated $\Delta\rho$ of -224 pcm is in good agreement with the experimental data of -212 pcm. However, a discrepancy on the value of $\Delta\beta_{eff}$ (-220 pcm vs. -304 pcm) was identified due to the inaccurate model developed by ORNL, which neglected the contribution to fission of delayed neutrons emitted in the upper and lower plenum. Also, velocity, temperature, pressure and delayed neutron precursor concentration have been calculated at 10 MWth and compared with the MSRE reports, showing close agreement. Moreover, three possible accidental transients (UTOP, ULOHS and ULOF) have been simulated and analyzed.

The Molten Salt Fast Reactor, developed in the Euratom's EVOL and SAMOFAR

projects, was another selected reference design to study effects of fuel salt compressibility and radiative heat transfer in MSRs. The MSFR Serpent model, adopting ENDF/B-VII.1 nuclear data library with six neutron energy groups and six DNP groups, was built in Serpent 2 to generate neutron group constants for the MSFR GeN-Foam model, which was developed in GeN-Foam and used for multi-physics calculations. The salt comressibility effect during a large reactivity-initiated accident was observed in both fluoride salt and chloride salt, and a consistent conclusion was made that incompressible-fluid simulations underestimate the power increase and the core outlet temperature. However, this phenomenon is more exaggerated and important in the chloride system because of its harder neutron spectrum and shorter neutron prompt lifetime. Besides, the effect of radiative heat transfer was evaluated in the fluoride MSFR, and preliminary results show that the impact on heat transfer during a loss of flow accident is limited. Nonetheless, some simple assumptions, such as the P1-approximation with a constant absorption coefficient and no scattering in salt, were applied and might affect the accuracy of results.

In the future, there are still a lot of work can be done to help researchers better understand and design MSRs. Enhanced results may be obtained by extending geometries of the MSRE and the MSFR from 2-D to 3-D, refining meshes near walls, modeling the gas phase or bubbles in salt, analyzing MSFR's safety under various accidental scenarios, applying more complex radiation models, and investigating different carrier salts with different radiation properties.

Bibliography

[1] Manuele Aufiero et al. "Calculating the effective delayed neutron fraction in the Molten Salt Fast Reactor: Analytical, deterministic and Monte Carlo approaches". In: *Annals of Nuclear Energy* 65 (2014), pp. 78–90.

[2] Manuele Aufiero, Pablo Rubiolo, and Massimiliano Fratoni. "Monte Carlo/CFD coupling for accurate modeling of the delayed neutron precursors and compressibility effects in molten salt reactors". In: *Transactions of the American Nuclear Society* 116.1 (2017), pp. 1183–1186.

[3] Jiadong Bao. "Development of the model for the multi-physics analysis of Molten Salt Reactor Experiment using GeN-Foam code". MA thesis. Paul Scherre Institut, 2016.

[4] Eric Cervi et al. "Development of a multiphysics model for the study of fuel compressibility effects in the Molten Salt Fast Reactor". In: *Chemical Engineering Science* 193 (2019), pp. 379–393.

[5] Carolyn Coyle, Emilio Baglietto, and Charles Forsberg. "Advancing radiative heat transfer modeling in high-temperature liquid salts". In: *Nuclear Science and Engineering* 194 (2020), pp. 782–792.

[6] V. N. Desyatnik et al. "Density, surface tension, and viscosity of uranium trichloride-sodium chloride melts". In: *Atomnaya Énergiya* 39.1 (1975), pp. 70–72.

[7] Thomas J. Dolan. *Molten salt reactors and thorium energy*. United Kingdom: Woodhead Publishing, 2017.

[8] James J. Duderstadt and Louis J. Hamilton. *Nuclear Reactor Analysis*. New York: John Wiley & Sons, Inc., 1976.

[9] John W. Eaton et al. *GNU Octave version 6.3.0 manual: A high-level interactive language for numerical computations*. 2021.

[10] *EVOL (project number 249696) final report*. CNRS, JRC-ITU, TUD, HZDR, KIT, POLITO, AD, EVM, BME, UOXF-DJ, INOPRO, PSUD, POLIMI, PSI, ROSATOM, 2015.

[11] Carlo Fiorina et al. "Development and verification of the neutron diffusion solver for the GeN-Foam multi-physics platform". In: *Annals of Nuclear Energy* 96 (2016), pp. 212–222.

[12] Carlo Fiorina et al. "GeN-Foam: A novel OpenFOAM based multi-physics solver for 2D/3D transient analysis of nuclear reactors". In: *Nuclear Engineering and Design* 294 (2015), pp. 24–37.

[13] Peter German, Jean C. Ragusa, and Carlo Fiorina. "Application of multiphysics model order reduction to Doppler/neutronic feedback". In: *EPJ Nuclear Sciences & Technologies* 5.17 (2019).

[14] Christophe Geuzaine and Jean-François Remacle. "Gmsh: A three-dimensional finite element mesh generator with built-in pre- and post-processing facilities". In: *International Journal for Numerical Methods in Engineering* 79.11 (2009), pp. 1309–1331.

[15] *GIF 2020 annual report*. Generation IV International Forum, 2020.

[16] P. N. Haubenreich. *Prediction of effectivce yields of delayed neutrons in MSRE*. Oak Ridge National Laboratory, 1962.

[17] Tobias Holzmann. *Mathematics, numerics, derivations and OpenFOAM®*. Leoben, Austria: Holzmann CFD, 2017.

[18] Frank P. Incropera et al. *Fundamentals of heat and mass transfer*. United States of America: John Wiley & Sons, 2007.

[19] R. J. Kedl. *Fluid dynamic studies of the Molten-Salt Reactor Experiment (MSRE) core*. Oak Ridge National Laboratory, 1970.

[20] John R. Lamarsh and Anthony J. Baratta. *Introduction to Nuclear Engineering*. Upper Saddle River, New Jersey: Prentice Hall, 2001.

[21] Jaakko Leppänen et al. "The Serpent Monte Carlo code: Status, development and applications in 2013". In: *Annals of Nuclear Energy* 82 (2015), pp. 142–150.

[22] Fengshan Liu, Jim Swithenbank, and Eric S. Garbett. "The boundary condition of the P_N-approximation used to solve the radiative transfer equation". In: *International Journal of Heat and Mass Transfer* 35.8 (1992), pp. 2043–2052.

[23] Elsa Merle et al. "Preliminary design studies of the draining tanks for the Molten Salt Fast Reactor". In: *European Nuclear Conference*. 2014.

[24] Michael F. Modest. *Radiative heat transfer*. United States of America: Academic Press, 2003.

[25] *Molten salt reactors*. URL: `https://world-nuclear.org/information-library/current-and-future-generation/molten-salt-reactors.aspx` (visited on 08/08/2021).

[26] *Nuclear science, technology, and engineering for molten salt reactors*. URL: `https://nustem.engr.tamu.edu` (visited on 08/08/2021).

[27] Michael Pantano. "Investigation of performance of an ultrasonic flow meter for potential molten salt reactor applications". MA thesis. Massachusetts Institute of Technology, 2016.

[28] Sun Myung Park, Andrei Rykhlevskii, and Kathryn D. Huff. "Safety analysis of the Molten Salt Fast Reactor fuel composition using Moltres". In: *14th International Nuclear Fuel Cycle Conference, GLOBAL 2019 and Light Water Reactor Fuel Performance Conference, TOP FUEL 2019*. 2020, pp. 940–948.

[29] B. E. Prince et al. *Zero-power physics experiments on the Molten-Salt Reactor Experiment*. Oak Ridge National Laboratory, 1968.

[30] R. C. Robertson. *MSRE design and operations report part I: Description of reactor design*. Oak Ridge National Laboratory, 1965.

[31] *SAMOFAR*. URL: `http://samofar.eu` (visited on 08/10/2021).

[32] Dan Shen. "Validations of computational codes of molten salt reactors". PhD thesis. University of California, Berkeley, 2019.

[33] Weston M. Stacey. *Nuclear reactor physics*. Weinheim, Germany: Wiley-VCH Verlag GmbH & Co. KGaA, 2018.

[34] Bjarne Stroustrup. *The C++ programming language*. Addison-Wesley, 2013.

[35] H. G. Weller et al. "A tensorial approach to computational continuum mechanics using object-oriented techniques". In: *Computers in Physics* 12.6 (1998), pp. 620–631.

[36] A. B. Wood. *A textbook of sound*. New York: The Macmillan Company, 1941.